TECHNISCHE UNIVERSITÄT DRESDEN

**Faculty of Civil Engineering** Institute for Structural Analysis

Master Thesis

# NUMERICAL EVALUATION OF SUPPORTING STRUCTURES FOR TRAFFIC ROAD SIGNS UNDER CONSIDERATION OF PASSIVE SAFETY REQUIREMENTS ACCORDING TO EN 12767

Petromichelakis Ioannis

ISD

Master Thesis

# Numerical evaluation of supporting structures for traffic road signs under consideration of passive safety requirements according to EN 12767

Petromichelakis Ioannis

Supervised by:
Prof. Dr.-Ing. Wolfgang Graf

and:
Dipl.-Ing. Marco Götz

submitted on March 21, 2013

TECHNISCHE UNIVERSITÄT DRESDEN

**Faculty of Civil Engineering** Institute for Structural Analysis

## Conceptual Formulation of the master thesis

Nr. MT07/13

Name: Ioannis Petromichelakis
Field of Study: ACCESS Master Course

**Topic:** **Numerical evaluation of supporting structures for traffic road signs under consideration of passive safety requirements according to EN 12767**
(Bewertung von Tragstrukturen für Verkehrszeichen unter Beachtung der Anforderungen an die passive Sicherheit nach EN 12767)

**Objective:**

In Germany usually traffic road signs, beside the road, are supported by specific truss structures. These structures have to fulfil requirements due to the passive safety of car passengers. This means, in case of a collision a car should knock over the supporting structure with a small deceleration. The truss structures are made of steel tubes with standardised dimensions. For these structures the fulfilling of the passive safety requirements was proven by means of a few real crash-tests, resulting in the definition of a catalogue with permissible truss geometries. A consensus was established that these trusses fulfil the requirements of passive safety. With introduction of EN 12767 limit values for deceleration were introduced in terms of head and neck injury criterions. Public authorities and companies are confronted with the problem to prove, if the traditional used structures fulfil the requirements. This master thesis should offer a possibility for proofing the conformity of the traditional used structures with the requirements according to EN 12767 by means of numerical analysis.

Following tasks should be formulated:

- study literature, especially EN 12767, with respect to passive safety requirements
- modelling an exemplary truss structure and a traffic road sign for the Finite Element Analysis software *LS-DYNA*
- study different support models, with and without foundation, consider realistic soil-models and the interaction between truss and traffic road sign with the aid of equivalent loads
- multi-body dynamic analysis of the crash with car model considering the crash against one truss and two trusses
- assessment and interpretation of results with respect to the limit values given in EN 12767
- proposals for verification of numerical models by means of crash tests

Scientific Consultant: Dipl.-Ing. Marco Götz

Date of issue: 22.05.13
Date of release: 23.09.13

Prof. Dr.-Ing. Wolfgang Graf
Supervisor

Graf

Ioannis Petromichelakis

DRESDEN concept

# DECLARATION OF ORIGINALITY

I confirm that this assignment is my own work and that I have not sought or used inadmissible help of third parties to produce this work and that I have clearly referenced all sources used in the work. I have fully referenced and used inverted commas for all text directly or indirectly quoted from a source.

This work has not yet been submitted to another examination institution – neither in Germany nor outside Germany – neither in the same nor in a similar way and has not yet been published.

Dresden, October 10, 2012

.....
(signature)

# ABSTRACT

The present master thesis is devoted to the numerical evaluation of supporting structures for traffic road signs including passive safety considerations according to the norm EN 12767. For that purpose, a numerical car crash simulation is performed, using the commercial software LS-DYNA. For the required calculations, a non-linear Finite Element Analysis is employed, while the time integration of the equation of motion is performed using an explicit solution method. Explicit methods, in conjunction with single integration point elements, provide an efficient numerical framework suitable for solving the computationally demanding task of the impact simulation. Subsequently, an uncertainty analysis is being performed, that accounts for polymorphic uncertainty, in order to provide overall information for the studied problem including considerations of different crash scenarios. The results of this later analysis, proved that during an impact of a vehicle against a traffic road sign supporting structure, the risk for serious injury of the occupant is practically negligible.

# CONTENTS

# 1 INTRODUCTION

The present master thesis, is devoted to the numerical evaluation of supporting structures for traffic road signs including passive safety considerations according to the norm EN 12767. For that purpose, a numerical car crash simulation is performed, using the commercial software LS-DYNA. For the required calculations, a non-linear Finite Element Analysis is employed, while the time integration of the equation of motion is performed using an explicit solution method. Explicit methods, in conjunction with single integration point elements, provide an efficient numerical framework suitable for solving the computationally demanding task of the impact simulation. Subsequently, an uncertainty analysis is being performed, that accounts for polymorphic uncertainty, in order to provide overall information for the studied problem including considerations of different crash scenarios. The results of this later analysis, proved that during an impact of a vehicle against a traffic road sign supporting structure, the risk for serious injury of the occupant is practically negligible (see Chapter 5).

## 1.1 PASSIVE SAFETY

Accidents on roadways is a very often phenomenon with daily occurrence. According to statistics derived from [17], each year in Europe, over a million roadway accidents are being reported, causing tens of thousands deaths and hundreds of thousands serious injuries. A very common type of roadway accidents is the event of vehicle impact against roadway equipment, such as vertical columns for lighting, traffic lights and traffic signs.

In order to reduce the number of accidents as well as their consequences, the authorities have established several safety regulations. These regulations include rules concerning the driving conditions as well as both the vehicle and the roadway design. All the actions performed to provide safety in the roadways are classified in two major categories, the so called *active safety* and *passive safety* actions.

Active safety measures are being used to minimize the risk for an accident to occur. Such measures include the advanced, sophisticated design of the vehicles and provide maximum control by the driver e.g. with reliable braking systems, ABS systems, rare-vision mirrors, instrument panels, etc. Moreover, the driving conditions including certified driving skills as well as the prohibition of driving under the influence of certain substances like alcohol, are accounted for, as active safety. In addition to those, there are active safety regulations that refer to the roadway design such as the proper road alignment, sufficient lighting, effective signage etc.

On the other hand, passive safety measures have been established to reduce the consequences given that an accident occurs. Such measures include the use of passenger restraint systems like seatbelts and air-bags as well as vehicle restraint bars on the roadway sides. In addition, a very important aspect of passive safety is the ability of the car to absorb energy during an impact. For that reason, modern auto-mobiles are constructed using sophisticated composite materials and proper set-up of the structural parts possessing excellent energy absorption properties.

More recently, the importance of using passively safe roadway equipment has been recognized [34].

Figure 1.1: Consequences of a vehicle colliding into various types of columns. **Left**: rigid column. **Right**: deformable column.

The reason is indicatively illustrated in Fig. 1.1, where the result of a car crash at similar speeds into two different types of columns is shown [19]. In Fig. 1.1 left, a vehicle that has collided into a rigid ordinary column is shown, while Fig. 1.1 right, shows a car collided into a deformable column that is categorized as a passively safe structure.

During an impact between a vehicle and a vertical structure, a lot of energy is dissipated. When the structure is rigid, almost all of the dissipated energy is transferred to the vehicle and its occupants. As a result, the vehicle performs a sudden deceleration and the risk for serious injuries of the passengers is very high. On the other hand, if the structure is deformable, exhibiting energy absorption properties, a sufficient amount of energy is dispersed, and the energy transferred to the vehicle and its occupants is lower. In that case, the vehicle experiences a smoother deceleration and the occupant safety is sufficiently increased.

In order to reduce the unfavourable consequences of traffic accidents caused by collision of vehicles against roadway infrastructure, the European Commission proposed in 2000 the use of passively safe roadside equipment. For that purpose, the norm EN 12767 [2] was established, which focuses on vertical support structures possessing energy absorption characteristics. An overview of passive safety requirements, is provided in Chapter 2.

## 1.2 COMPUTER SIMULATION

Computer aided car crash simulations, are widely used in the vehicle design procedure in order to reduce the total development cost. After several years of advancement such simulations have reached a high degree of accuracy and numerical efficiency. In addition to that, numerical models of vehicles have become publicly available, making car crash simulations feasible for educational purposes. For the numerical evaluation of the traffic sign support structure, a car crash simulation with the non-linear dynamic Finite Element Analysis (FEA) software LS-DYNA has been used. The numerical model of the vehicle has been provided by National Crash Analysis Centre (NCAC), U.S.A. and it contains one Dummy provided by the DYNAmore GmbH, Germany (see Chapter 3).

Car crash simulations, are highly non-linear problems due to the extreme strains involved. As a result, advance non-lineal Finite Element codes like LS-DYNA should be employed, which require a sufficient amount of computational effort. In addition to this, the collision event is very fast and a small time step size is needed, which assigns extra computational effort in the process of time integration of the dynamical problem. As a result, an efficient explicit solution method (see Chapter 4), which uses small time steps anyway, is highly suitable.

For the solution of complex dynamical problems, the differential equation of motion, needs to be solved iteratively in time. In *explicit methods*, the state of the system in a later time, is calculated using information provided in the current time only [11]. As a result, the explicit solution methods, provide a set of recursive formulas that update the kinematic quantities (accelerations, velocities and displacements) of the problem without requiring the solution of systems of equations. These recursive formulas are based on approximations that can possibly result in unstable solution schemes. Explicit time integration methods, such as the *Central Difference Method*, are conditionally stable [46]. This means that they can be stable, given that the time step size is less or equal to a critical value.

The *critical time step size* of an explicit solution, equals the time that a sound wave needs to propagate through the smallest element and is referred to as the *Courant-Friedrichs-Lewy condition* [24]. Due to this condition, the calculated time step may become very small and overload the analysis in view of computational effort. As a result, the explicit solution methods are usually coupled with single integration point elements, which are very efficient and after the advances of [29] and [10] are sufficiently accurate. The use of single point integration elements, has the advantage of eliminating the *locking* effect and the disadvantage of the so-called *hourglass phenomenon*, both described in section 3.1.6.

In *implicit methods* on the other hand, the state of the system in a later time is determined by solving an equation involving both the current state of the system and the later one. As a result, implicit methods such as the *Newton method* and the *Newmark-β method*, provide an accurate, stable solution scheme. The disadvantage of the increased computational effort for each integration loop, is confronted by the use of large time steps. This requirement, makes the implicit solution methods inappropriate for the crash simulation problem, relatively to the explicit methods.

## 1.3 UNCERTAINTY

When assessing safety of a simulated system, some parameters of the physical or the computational model are not precisely known or exhibit some natural variation, they are thus uncertain parameters. As a result, in order to extract overall information, accounting for different event scenarios, an approach that involves the calculation of variants of the studied system, with non-precise input values, should be employed. Such an approach is usually referred to as *uncertainty analysis* (see Chapter 6). A very important aspect in uncertainty analysis, is to determine which variables of the problem are the most critical, as well as, their intervals of variation. This later procedure is usually referred to as *sensitivity analysis*.

In order to account for the special characteristics of an uncertain variable, the traditional approach of *random variables* (see section B.1.1), derived from *probability theory*, can be used. This approach however, is appropriate only for uncertain parameters that exhibit a natural, random variation, they are thus characterized by *variability*. This type of uncertainty is referred to as *aleatory uncertainty* [41]. Some parameters though, are uncertain because their values are based on incomplete and/or imprecise information. This type of uncertainty, that is associated with the uncertainty characteristics *incompleteness* and *impreciseness* is referred to as *epistemic uncertainty*.

According to [41] and [22], an appropriate approach to describe uncertain parameters of epistemic type is *fuzzy variables* [40] (see section B.1.2), derived from *fuzzy set theory*. The numerical treatment of fuzzy variables, is performed using a global optimization concept, as $\alpha$-level optimization, in conjunction with a modified evolution strategy [42]. In addition, it is possible to employ generalized models [43],[22], such as *fuzzy random variables*, that appropriately describe variables that possess more than one uncertainty characteristics simultaneously. For the uncertainty analysis, the

software 'Winfuz' is used, which is capable of performing Fuzzy Stochastic Analysis (FSA), which is a computational framework that involves fuzzy, random and fuzzy random variables simultaneously.

Uncertainty analysis of industry sized applications, such as the numerical simulation of the vehicle impact, requires a large number of evaluations of the deterministic fundamental solution, which in this case is the Finite Element model. This multiple evaluation, boosts the total numerical effort of the analysis which often becomes unfeasible. This problem is confronted by constructing a surface, in the n-dimensional input subspace $\mathbb{X} \subset \mathbb{R}^n$, that approximates the response value for each vectored point $\mathbf{x} \in \mathbb{X}$. This approach is referred to as the *metamodel* approach and provides a practical, very efficient alternative of the original computational model. The metamodel method is a generalization of the older *Response Surface* (approximation) *Method* (RSM) [14]. A more modern term for *metamodel* is *surrogate model*.

# 2 NORMATIVE REFERENCE

In the present chapter, an overview of the injury criteria, the impact severity indices and of the code EN 12767:2007 *'Passive safety of support structures for road equipment - Requirements, classification and test methods'*, is being presented.

## 2.1 INJURY CRITERIA

### 2.1.1 Head Injury Criterion (HIC)

The Head Injury Criterion (HIC) is a measure of the likelihood of head injury arising from an impact. The HIC can be used to assess safety related to vehicles. Normally the variable is derived from the acceleration time-history of an accelerometer mounted at the centre of gravity of a dummy's head (point H in Fig. 2.1), when the dummy is exposed to crash forces. It represents a relationship between the acceleration level and the impulse duration with respect to head injury [39].

According to [26] HIC is defined by Eq. (2.1),

$$\mathrm{HIC} = \max_{t_1,t_2} \left[ (t_2 - t_1) \left( \frac{1}{t_2 - t_1} \int_{t_1}^{t_2} \alpha(t) \mathrm{d}t \right)^{2.5} \right] \tag{2.1}$$

where $t_1$ and $t_2$ are the initial and final times (in seconds) of the interval during which HIC attains a maximum value and $\alpha$ is the acceleration measured in $\mathrm{g}$ (standard gravity acceleration, $1\ \mathrm{g} = 9.81\ \mathrm{m/s^2}$).

$$\alpha = \sqrt{{\alpha_x}^2 + {\alpha_y}^2 + {\alpha_z}^2} \tag{2.2}$$

It should be noted that the maximum time duration of HIC, $t_2 - t_1$, is limited to a specific value, usually $36\ \mathrm{ms}$ and $15\ \mathrm{ms}$. This means that the HIC includes the effects of head acceleration and the duration of the acceleration. Large accelerations may be tolerated for very short times. As a result, there are various alternative ways for the calculation of the HIC value. The most important are described in [1] and are:

| | | |
|---|---|---|
| HIC | for $t_2 - t_1$ | unlimited, |
| HIC36 | for $t_2 - t_1$ | $\leq 36\ \mathrm{ms}$, |
| HIC15 | for $t_2 - t_1$ | $\leq 15\ \mathrm{ms}$. |

A very common phenomenon in the measurement of accelerations during vehicle impacts, is the presence of noise in the results. More specifically, the accelerometer appears to measure an oscillation with amplitude much higher than the expected acceleration values. As a result, the original data is covered by this oscillation and it is impossible to extract any accurate results. This phenomenon

is observed in both, computer simulated impacts and real impact experiments. The solution to that problem is the use of low pass filters on the raw data, see Appendix B.2.1.

According to [1], the measured values of the head acceleration components $\alpha_x$, $\alpha_y$ and $\alpha_z$, should be filtered in accordance to CFC 1000 defined in [31], see Appendix B.2.1.

At a HIC value of 1000, one in six people will suffer a life-threatening injury to their brain. More accurately, an 18% probability of a severe head injury, a 55 % probability of a serious injury and a 90 % probability of a moderate head injury to the average adult [38]. A maximum HIC value of 1000 is also proposed by the European New Car Assessment Programme (Euro NCAP), associated with a 20 % risk of injury.

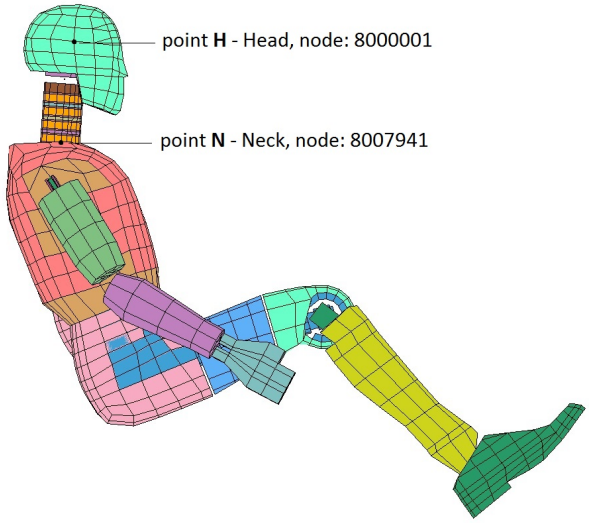


Figure 2.1: Points of acceleration measurement on the dummy.

### 2.1.2 Neck Injury Criterion (NIC)

The majority of neck injuries are caused by indirect loading produced by inertial loads being transferred from the torso to the head, following head impact or high acceleration. As the neck comprises of skeletal vertebrae joined by cartilage ligaments and muscles the range and type of motions produced are complicated, being combinations of translations and rotations in all three dimensions. The overall motion is also dependent on the direction of the resultant force and therefore impact location and direction on the head, or acceleration direction on the torso. The neck injury mechanism during a rear-end impact is shown in Fig. 2.2.

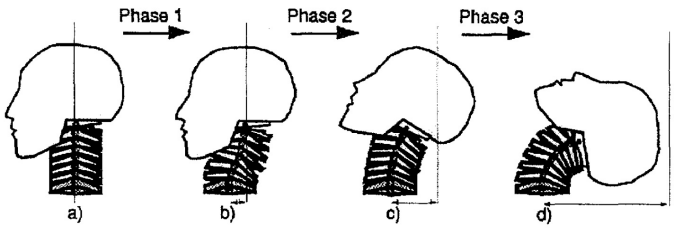


Figure 2.2: Schematic view of four parts of the head-neck motion during a rear-end collision: a) initial posture, b) maximum retraction, c) maximum rearward angular velocity of the head is reached, d) hyper extension. [13].

The NIC calculation procedure provided by [13] is shown in Eq. (2.3) - (2.5).

$$NIC = \alpha_{relative} \cdot 0.2 + v_{relative}{}^2 \tag{2.3}$$

$$\alpha_{relative} = \alpha_N - \alpha_H \tag{2.4}$$

$$v_{relative} = \int \alpha_{relative} dt \tag{2.5}$$

Where, $\alpha_N$ and $\alpha_H$ are the overall acceleration values at points N (neck) and H (head), shown in Fig. 2.1. The NIC value is the maximum value calculated during the crash and is measured in $\mathrm{m}^2/\mathrm{s}^2$. The maximum NIC value tolerable by the human body is $15\ \mathrm{m}^2/\mathrm{s}^2$ [13].

## 2.2 IMPACT SEVERITY INDICES

The European Commission adopts in [2] two indices to describe the severity of vehicle impact. The two indices are the Acceleration Severity Index (ASI) and the Theoretical Head Impact Velocity (THIV) and they are defined in [4]. In the present section, the calculation procedure for the two indices is quoted.

According to [4], measures of accelerations should taken for each one of the three Cartesian axes from a point close to vehicle's centre of gravity. The yaw rate[1] should be measured at the same point as well.

All the measurements should be processed according to the flow chart in Fig. 2.3, which is derived from [4], in order to be appropriately filtered with a suitable low-pass filters indicated by corresponding Channel Frequency Class (CFC) as defined in [4], [7] and [31].

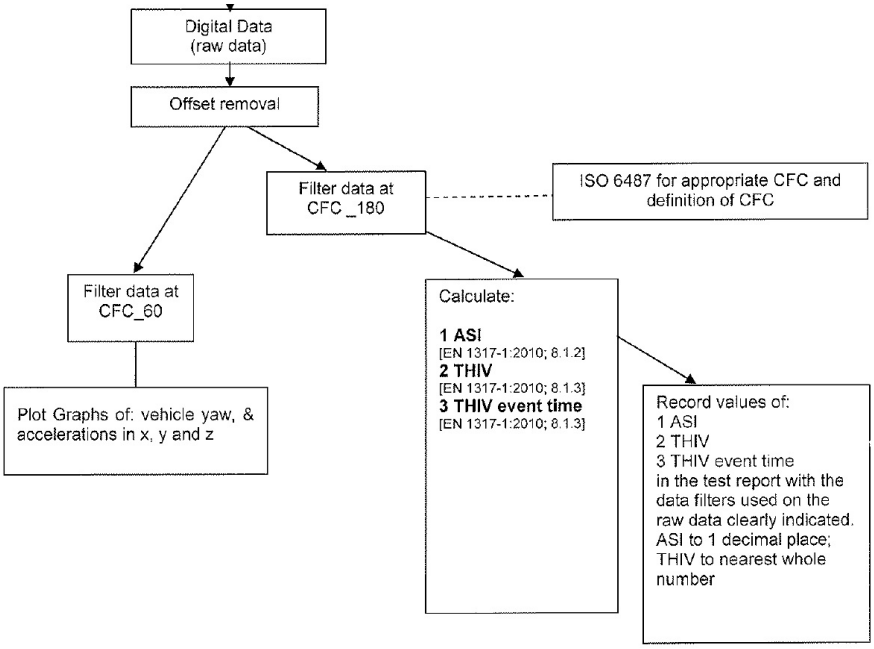


Figure 2.3: Data processing flow diagram for filtering the raw acceleration data recorded during impact tests. [4].

[1] Yaw rate is the rotational velocity with respect to the vertical (z) axis.

### 2.2.1 Acceleration Severity Index (ASI)

As indicated in Fig. 2.3, the acceleration measurements should be filtered with a CFC_180 filter before the calculation of the ASI which is shown in Eq. (2.6).

$$\mathrm{ASI}(t) = \left[ \left( \frac{\bar{A}_x(t)}{12} \right)^2 + \left( \frac{\bar{A}_y(t)}{9} \right)^2 + \left( \frac{\bar{A}_z(t)}{10} \right)^2 \right]^{0.5} \tag{2.6}$$

Where $\bar{A}_x$, $\bar{A}_y$, $\bar{A}_z$ are the filtered components of vehicle acceleration. The ASI value is the maximum among the ASI(t) values, it should be calculated with at least two decimal places and reported with one decimal place after mathematical rounding.

### 2.2.2 Theoretical Head Impact Velocity (THIV)

The theoretical head impact velocity (THIV) concept has been developed for assessing occupant impact severity for vehicles involved in collisions with roadway equipment. The occupant is considered to be a freely moving object (head) that, as the vehicle changes its speed during contact with the support structure, continues moving until it strikes a surface within the interior of the vehicle. The magnitude of the velocity of the theoretical head impact is considered to be a measure of the vehicle to support structure impact severity. In [4] the procedure to compute the THIV is described in detail and is quoted in the present subsection.

It can be assumed that at the beginning of the contact of the vehicle to the support structure, both the vehicle and the theoretical head have the same horizontal velocity $v_0$, vehicle motion being purely translational.

During the impact the vehicle is assumed to move only in a horizontal plane, because high levels of rotation along the longitudinal (x) axis, the so called roll and along the transverse (y) axis, the so called pitch as well as vertical motion are not of prime importance.

Two right handed reference frames shall be used.

a) A "vehicle" reference frame Cxy, x being longitudinal (positive forwards) and y transverse (positive to the right). This frame moves with the vehicle, so that the origin C is a fixed point within the vehicle close to the center of mass. This reference frame does not rotate around the x (roll) or y (pitch) axes, but is free to rotate around the z (yaw) axis as the vehicle rotates so that at time $t$ it makes an angle $\psi$ (positive clockwise viewed from above) with the initial direction at $t = 0$.

b) A "moving ground" reference frame CXY which is coincident with the "vehicle" axes at time $t = 0$, and initially moves with the same velocity as the vehicle. This axis is "inertial", i.e. it moves without acceleration at constant velocity, and does not rotate.

It should be noted that although both reference frames are initially moving with the vehicle initial velocity $v_0$, the analysis is concerned purely with velocity changes relative to this initial velocity.

Since the freely moving head does not accelerate before it strikes a surface within the vehicle, its coordinates in the ground reference frame shall remain constant during the free-flight phase of its motion.

For the THIV calculation, recordings of the velocity of the centre of mass of the car $v_c = (v_c^x, v_c^y)$ and rotational velocity (yaw rate) $\dot{\psi}$ are used. The initial velocity of the vehicle is denoted by $v_0 = (v_0^x, v_0^y)$. In the later, displacements in moving ground reference are denoted by capital $X$ and $Y$, while in vehicle reference by lower $x$ and $y$ and $\dot{X}$, $\dot{Y}$, $\dot{x}$ and $\dot{y}$ are the corresponding velocities. The subscript $C$ is used to denote the car centre of mass and $b$ the theoretical head. Moreover, the measurements are recorded in discrete time and the time-step is denoted by $dt$. It should be noted that the recorded $y$ component of the velocity, should be multiplied by $-1$ because the $y$ axis in the simulation has the opposite direction with the assumed $y$ axis in the THIV calculation.

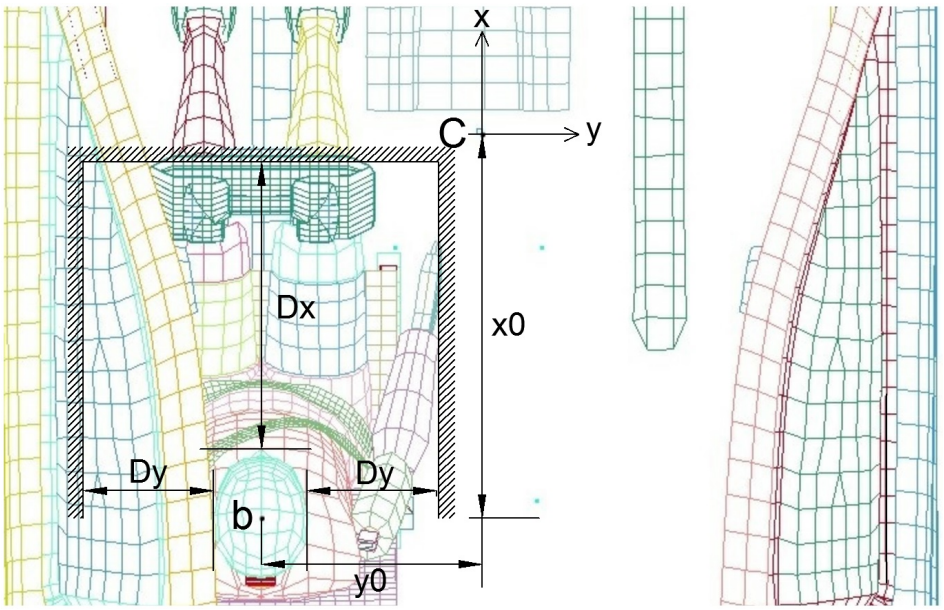


Figure 2.4: Vehicle interior ordinance for the case studied.

The vehicle motion in the moving (but non-rotating) ground coordinates is described by Eq. (2.7)-(2.9).

The yaw angle $\psi$ is calculated by integration of the yaw rate *psi* in Eq. (2.7).

$$\psi(t) = \dot{\psi}(t) \cdot dt \tag{2.7}$$

The vehicle velocity and displacement is calculated according to Eq. (2.8) and (2.9) respectively.

$$\begin{aligned} \dot{X}_C(t) &= v_c^x(t) - v_0^x \\ \dot{Y}_C(t) &= v_c^y(t) - v_0^y \end{aligned} \tag{2.8}$$

$$\begin{aligned} X_C(t) &= \dot{X}_C(t) \cdot dt \\ Y_C(t) &= \dot{Y}_C(t) \cdot dt \end{aligned} \tag{2.9}$$

The theoretical head does not move relatively to the moving ground, because during the impact, they both move along the $X$ axis with the initial velocity.

The motion of the theoretical head relative to the vehicle is then described by Eq. (2.10) and (2.11).

$$x_b(t) = (x_0 - X_C(t))\cos\psi(t) + (y_0 - Y_C(t))\sin\psi(t)$$
$$y_b(t) = -(x_0 - X_C(t))\sin\psi(t) + (y_0 - Y_C(t))\cos\psi(t) \tag{2.10}$$

Where $x_0$ and $y_0$ are the initial distances of the head from the car centre of mass $C$, see Fig. 2.4.

$$\dot{x}_b(t) = -\dot{X}_C(t)\cos\psi(t) - \dot{Y}_C(t)\sin\psi(t) + y_b(t)\dot{\psi}(t)$$
$$\dot{y}_b(t) = \dot{X}_C(t)\sin\psi(t) - \dot{Y}_C(t)\cos\psi(t) - x_b(t)\dot{\psi}(t) \tag{2.11}$$

The terms $x_b(t)\dot{\psi}(t)$ and $y_b(t)\dot{\psi}(t)$ arise from the velocity of a point in the rotating frame of reference at a point with coordinates $(x_b, y_b)$ in the frame. The angular rate term $\dot{\psi}$ shall be measured in radians per second $(\mathrm{rad/s})$.

The notional impact surfaces inside the vehicle are assumed to be flat and perpendicular to the vehicle $x$ and $y$ axes, see Fig. 2.5 and 2.4. The distances of those surfaces from the original head position (flail distances) shall be $D_x$ forward and $D_y$ laterally on both sides.

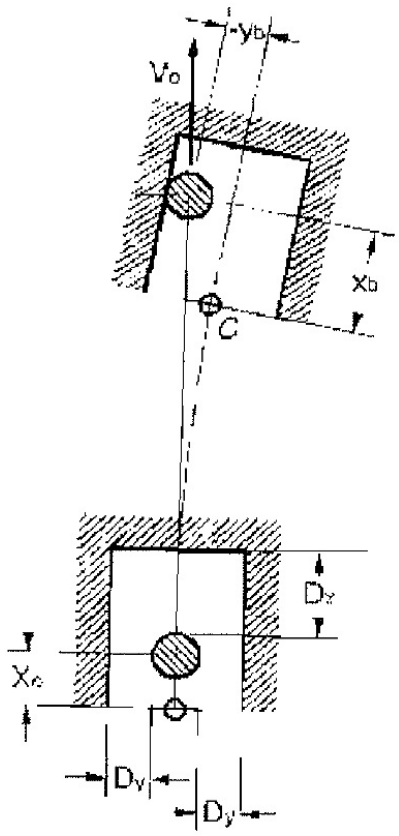


Figure 2.5: Impact of the theoretical head on the left side. [4].

For the calculation of the time of flight defined as the shortest time $t_s$ that the theoretical head strikes on one of the three vehicle interior surfaces shown in Fig. 2.5 and 2.4, one of the three relationships in Eq. (2.12) should be satisfied.

$$
\begin{aligned}
x_b(t_s) &= D_x + x_0 \\
y_b(t_s) &= D_y + y_0 \\
y_b(t_s) &= -D_y + y_0
\end{aligned}
\tag{2.12}
$$

The code [4] proposes standard values for the flail distances $D_x = 0.6\ \mathrm{m}$ and $D_y = 0.3\ \mathrm{m}$.

Finally the calculation of the THIV value is performed according to Eq. (2.13).

$$
THIV = \left[\dot{x}_b^2(t_s) + \dot{y}_b^2(t_s)\right]^{0.5} \tag{2.13}
$$

The THIV value should be calculated to at least one decimal place and be reported to zero decimal place by mathematical rounding.

## 2.3 EN 12767:2007

This European Standard, was released in 2000 (and revised in 2003 and 2007) in order to provide guidelines for the design of roadside support structures, the performance of which, affects the severity of collisions for vehicle occupants. These structures can be designed in such a way that they detach or yield when a vehicle impacts on them. The scope of [2] is quoted unedited in the following paragraph.

"This European Standard specifies performance requirements and defines levels in passive safety terms intended to reduce the severity of injury to the occupants of vehicles impacting with the permanent road equipment support structures. Consideration is also given to other traffic and pedestrians. Three energy absorption types are considered and test methods for determining the level of performance under various conditions of impact are given."

The test parameters, requirements and test methods proposed by [2] are described in the next subsections with special attention to sign support structures.

### 2.3.1 Speed Classes

The investigated support structure shall be tested for the speed classes selected by the manufacturer from Table 2.1. The test shall be carried out at each of the two impact speeds of the selected speed class. The test at $35\ \mathrm{km/h}$ is performed to ensure satisfactory functioning of the support structure at low speed, while the test at the class impact speed (50, 70 and $100\ \mathrm{km/h}$) represents the main testing case.

Table 2.1: Impact speeds

| Speed class<br>km/h | Impact speeds<br>km/h |
|---|---|
| 50 | 35 and 50 |
| 70 | 35 and 70 |
| 100 | 35 and 100 |

### 2.3.2 Energy absorption categories

The standard [2] considers three categories of passive safety support structures, high energy absorbing (HE), low energy absorbing (LE), non-energy absorbing (NE).

In the case that a support structure is classified as energy absorbing, the risk of secondary accidents with structures, trees, pedestrians and other road users is reduced, because the vehicle is considerably decelerated. Non-energy absorbing support structures on the other hand, permit the vehicle to continue after the impact with no significant reduction of its speed. Non-energy absorbing support structures can still be passively safe, due to their ability to detach after the impact, and thus they provide a lower primary injury risk than the energy absorbing support structures.

The energy absorption classification of a support structure is performed by relating the exit speed of the vehicle after the impact, to the selected speed class according to Table 2.2.

Table 2.2: Energy absorption categories

| Impact speed, $v_I$ km/h | 50 | 70 | 100 |
|---|---|---|---|
| Energy absorption category | Exit speed, $v_e$ km/h | | |
| HE | $v_e = 0$ | $0 \leq v_e \leq 5$ | $0 \leq v_e \leq 50$ |
| LE | $0 < v_e \leq 5$ | $5 < v_e \leq 30$ | $50 < v_e \leq 70$ |
| NE | $5 < v_e \leq 50$ | $30 < v_e \leq 70$ | $70 < v_e \leq 100$ |

In the case that the actual speed of the vehicle is not the nominal speed, a formula is provided in [2] that can be used to adjust the measured exit speed for the proper energy absorption categorization. In the present thesis, the vehicle impact test is performed with the aid of computer simulation, and thus the actual impact speed can be selected in advance to be equal to the nominal speed of the selected speed class.

### 2.3.3 Levels of occupant safety

There are four levels of occupant safety in [2]. Levels 1,2 and 3 provide increasing levels of safety in that order by reducing impact severity. For these levels two test are required as mentioned in 2.3.1. One low speed test with an impact speed of 35 km/h and one test with the class impact speed according to Table 2.1. Level 4 comprises very safe support structures classified by means of a simplified test at the class impact speed only.

Support structures shall be classified in terms of the occupant safety level by means of the ASI and THIV [2] values, related to the speed class and energy absorption categories in Table 2.3. Occupant safety level NE4 is restricted to non-harmful support structures which is not the case in the present thesis.

[2] The injury criteria ASI (Acceleration Severity Index) and THIV (Theoretical Head Impact Velocity) are analytically described in section 2.1

Table 2.3: Occupant safety

| Energy absorption categories | Occupant safety level | Speeds | | | |
|---|---|---|---|---|---|
| | | Mandatory low speed impact test 35 km/h | | Speed class impact tests 50, 70 and 100 km/h | |
| | | Maximum Values | | Maximum Values | |
| | | ASI | THIV km/h | ASI | THIV km/h |
| HE | 1 | 1,0 | 27 | 1,4 | 44 |
| HE | 2 | 1,0 | 27 | 1,2 | 33 |
| HE | 3 | 1,0 | 27 | 1,0 | 27 |
| LE | 1 | 1,0 | 27 | 1,4 | 44 |
| LE | 2 | 1,0 | 27 | 1,2 | 33 |
| LE | 3 | 1,0 | 27 | 1,0 | 27 |
| NE | 1 | 1,0 | 27 | 1,2 | 33 |
| NE | 2 | 1,0 | 27 | 1,0 | 27 |
| NE | 3 | 1,0 | 11 | 0,6 | 11 |
| NE | 4 | No requirement | No requirement | | |

For a given combination of the energy absorption category and occupant safety level, the ASI and THIV values shall not exceed the maximum values specified in Table 2.3 for both the low impact speed and the high impact speed tests.

### 2.3.4 Particular test parameters for traffic sign supports

The parts of [2] under the title *"Particular test parameters for different roadside objects"* that refer to traffic sign supports, are quoted unedited in the present subsection.

*"A sign plate shall be installed when a sign support is tested. Luminaries or transilluminated signs or other electrical equipment and cables including typical underground cables and connection boxes and/or fuse units, shall be installed if the sign support is intended for use with such items.*

*For multi-legged support structures, with intended installation perpendicular to the carriageway, and where the projected clear openings*[3] *at the* 20° *impact direction between the support structure legs are not less than 1.5 m, the tests shall be carried out against one leg with the test vehicle impact point central to that leg. Where the same projected clear openings between legs are less than 1.5 m, the tests shall be carried out against two legs with the test vehicle impact point aligned midway between two supports."*

*"The test results are valid for sign plates and fixings that do not restrain the impacted legs significantly more than in the specific tests."*

[3] see Fig. 2.6

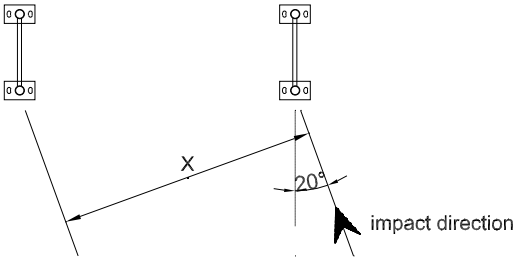


Figure 2.6: Test set-up for multi-legged support structures.

In Fig. 2.6, the test set-up for multi-legged sign support structures is demonstrated. The quantity $x$ represents the projected clear opening at the $20°$ impact angle. In the case studied in the present thesis, $x \approx 1.7\ \mathrm{m} > 1.5\ \mathrm{m}$. As a result, according to the code, the test can be adequately carried out using only the one leg of the structure. Despite that fact, the multi-legged structure is used in almost all the simulations performed in the present thesis, for reasons related to accuracy and realism.

### 2.3.5 Requirements

The performance type of each tested support structure is expressed as a combination of speed class, energy absorption category and occupant safety level, determined by the alternatives in Table 2.4, and noted in the corresponding format, e.g. 100HE2, 70LE1.

Table 2.4: Performance types

| | **Alternatives** |
|---|---|
| Speed class | 50, 70 or 100 |
| Energy absorption category | HE, LE or NE |
| Occupant safety level | 1, 2, 3 or 4 |

- **Basic requirements**
  - **Predictable behaviour**
    *"The test item shall technically behave in a manner predicted by the manufacturer, in terms of shearing or detaching, deforming only, or deforming and shearing. The levels of occupant safety and exit speed need not be predicted.*
    *If the test item fails to behave in the manner predicted, a performance class shall not be declared."*
  - **Road user or vehicle occupant risk**

    **Detached elements and penetration**
    *"The test item or detached elements, fragments or other major debris from the test item shall not penetrate the occupant compartment. The windscreen may be fractured but shall not be penetrated."*

    **Vehicle behaviour**
    *"The vehicle shall remain upright for not less than 12 m beyond the impact point with a roll angle less than* $45°$ *and a pitch angle less than* $45°$*.*
    *NOTE Yawing is accepted."*

**Acceleration severity index (ASI)**
*"The maximum ASI value in relation to each speed class, energy absorption category and occupant safety level shall not exceed the value specified in Table 2.3."*

**Theoretical Head Impact Velocity (THIV)**
*"The maximum THIV value in relation to each speed class, energy absorption category and occupant safety level shall not exceed the value specified in Table 2.3."*

- **Additional requirements for cantilever and gantry sign supports**

*"Fifteen minutes after the impact the lowest point of the support structure or of any signs mounted on it may not be lower than 4.0 m. This time and height applies only to points located over the intended carriageways. Other height limits may be specified by national regulations."*

- **Selection of items for test and product families**

  – **General**
  *"A support structure shall be tested with a load corresponding to the maximum design load in respect of mass and, if critical, area or other dimensions. Specific requirements for certain product types are as follows:*

  *A lighting column shall be tested ...*

  *A traffic sign support shall be tested with the maximum height selected by the manufacturer, and with the largest area of symmetrically mounted sign plate for which that height of support is designed, in terms of a declared bending moment resistance at ground level.*

  *A successful test result shall also be valid for a smaller area of sign plate; for asymmetric mounting of the sign plate; and for the same support structure reduced in height but otherwise of exactly the same detailed construction and dimensions. Due to the risk of penetration of the windscreen of an impacting car, the untested reduced minimum height of the lower edge of the sign shall not be lower than 2,0 m. Lower installations may be used, but risk of windscreen penetration shall be evaluated."*

  – **Product families**
  *"The largest size of any proposed product family shall be tested first, at the speed class selected and at low speed.*

  *NOTE Usually the largest size will have the greatest resistance to load, in terms of bending moment resistance at ground level.*

  *Depending on the results of these tests, further tests shall be carried out as described in Appendix A.2"*

  In the present thesis, the largest among the family of similar products is tested only, and especially the one with the most stiff bottom part of the vertical truss (see Fig. 3.1 left). This assumption is valid, because due to the particular geometry, the higher mass and the stiffer bottom part, the selected support structure will induce higher deceleration to the impacting vehicle. As a result, any other, smaller alternative of the selected structure, will certainly fall to the same or higher occupant safety level.

### 2.3.6 Impact test method

Analytical information concerning the testing method, are provided in [2]. This is, details about the site, the vehicle, the item to be tested, the installation procedure, the position of the impact point and the impact angle, the data to be recorded, the vehicle impact and exit speed, the approach angle measurement, the vehicle instrumentation, the photographic coverage, the test report and the data decimal rounding. It is beyond the scope of the present thesis to quote all of them. A brief reference to the most important aspects of the testing method follows.

- **Test vehicle**
  The test vehicle shall be a standard passenger car with an inertial mass of $825\ \mathrm{kg} \pm 40\ \mathrm{kg}$. One dummy shall be included, with a mass of $78\ \mathrm{kg} \pm 5\ \mathrm{kg}$ and the gross static mass shall be $900\ \mathrm{kg} \pm 40\ \mathrm{kg}$. The front and the rear wheel track should be $1.35\ \mathrm{m} \pm 0.20\ \mathrm{m}$. The dimensions of the centre of gravity along each axis should be: $CGx = 0.90\ \mathrm{m} \pm 0.09\ \mathrm{m}$, $CGy = 0.00\ \mathrm{m} \pm 0.07\ \mathrm{m}$ and $CGz = 0.49\ \mathrm{m} \pm 0.05\ \mathrm{m}$, see also Fig. 2.7.

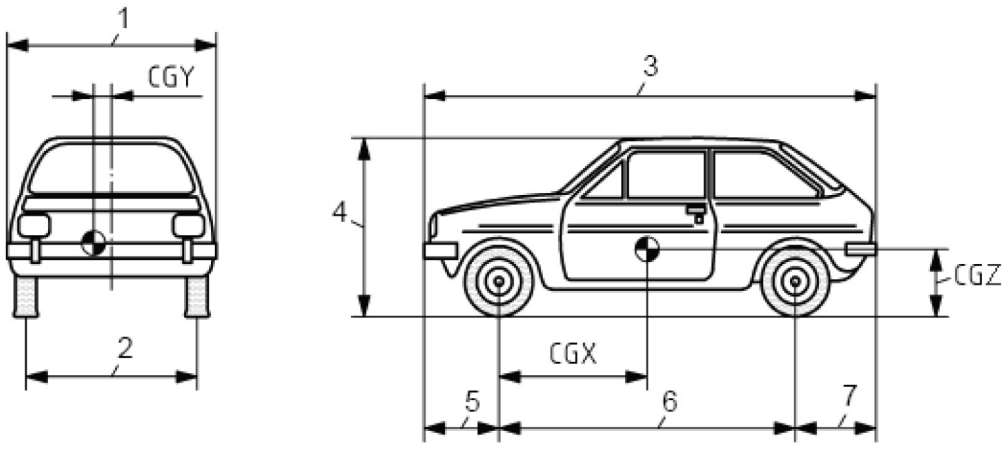


**Key**

1. Width
2. Track width (frontal)
3. Length
4. Height
5. Frontal overhang
6. Wheel base
7. Rear overhang

Figure 2.7: Vehicle dimensions.

- **Position of impact point and impact angle**
  *"The impact point on the test vehicle shall be centred to within* $\pm 0.1\ \mathrm{m}$. *The impact angle shall simulate a vehicle leaving the road at* $20° \pm 2°$.

  *For direction sensitive support structures additional tests with other impact angles may be decided by the approved certification body. If it is possible to impact the support structure from the side or even from behind, corresponding impact angles may be requested.*

  *If the lower part of a vertical sign is located in such a way that it may hit the windscreen of the test vehicle, an additional high speed test at* $20° \pm 2°$ *shall be made at the point regarded as the most critical by the approved certification body. This also applies to any other test items where there is a risk that the windscreen may sustain a direct hit from the test item."*

  For multi-legged test items see subsection 2.3.4.

- **Test data to be recorded**
  The most important test data to be recorded are the following:
  - mass and location of the centre of gravity of the test vehicle in the test condition
  - vehicle dimensions
  - test vehicle speed at impact and exit
  - test vehicle approach angle and impact point
  - linear accelerations and angular rates (the accelerations should be measured in accordance to [4], see *"Filtering"* in section 5.3)
  - damage to the test item and test vehicle
- **Test vehicle impact and exit speed**

  It is mentioned in [2] that the impact speed and the approach angle should be measured $6\ \mathrm{m}$ before the impact point and the exit speed $12\ \mathrm{m}$ beyond the impact point. In the case studied within the present thesis, the impact speed is measured slightly before the impact point, and the exit speed exactly after the vehicle has completely passed through the structure. This assumption has been made for two reasons. First, due to the absence of information concerning the friction between the tyres and the pavement, which is the only factor that would affect the results. And second, because a computer simulation of the car travelling for 18 meters would be computationally expensive.

# 3 NUMERICAL MODEL

The structure was modelled and analysed for impacting by a vehicle, using the commercial software LS-DYNA. This package is developed by the Livermore Software Technology Corporation (LSTC) and is an advanced general-purpose multi-physics simulation software package [37]. It is capable of performing highly non-linear transient dynamic Finite Element Analysis (FEA) using explicit time integration, and for that reason it is very popular in the automotive industry. LS-DYNA is widely used for vehicle impact simulations, also due to the efficient treatment of contact problems.

## 3.1 STRUCTURE

The traffic sign support structure studied in the present thesis is a roadway sign support structure consisting of two vertical trusses (see Fig. 3.1) with a framed sign attached on them. Each vertical column of the truss is welded on a 20 mm thick steel plate. Each truss, or more accurately the two plates that support each truss are bolted on a rigid concrete foundation shown in Fig. A.1 right, upper in Appendix A.1. For that reason displacement of the foundation has not been taken into account.

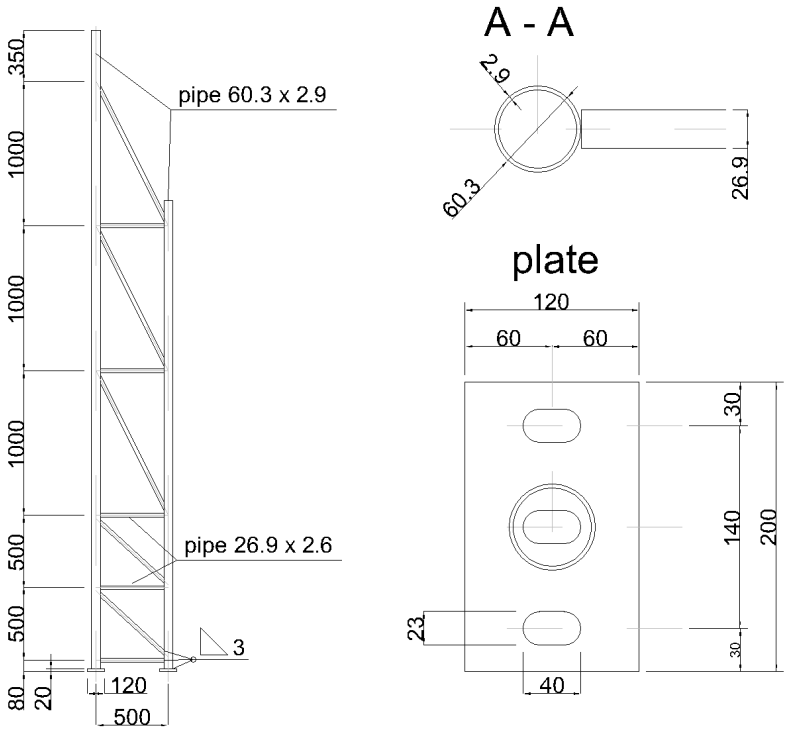


Figure 3.1: Drawings of the truss, all dimensions in mm. **Left**: truss. **Right**: Up: Section cut A - A. Down: Supporting plate.

### 3.1.1 Truss

As shown in Fig. 3.1, the truss consists of two vertical pipes of diameter $60.3\ \mathrm{mm}$ and a number of smaller horizontal and diagonal pipes of diameter $29.9\ \mathrm{mm}$. The geometrical model of the structure was designed and discretized using the preprocessor of the commercial software package Abaqus and subsequently transferred to LS-DYNA for the further steps of the analysis. The mesh of the truss is shown in Fig. 3.2, derived from the LS-DYNA preprocessor LS-PrePost.

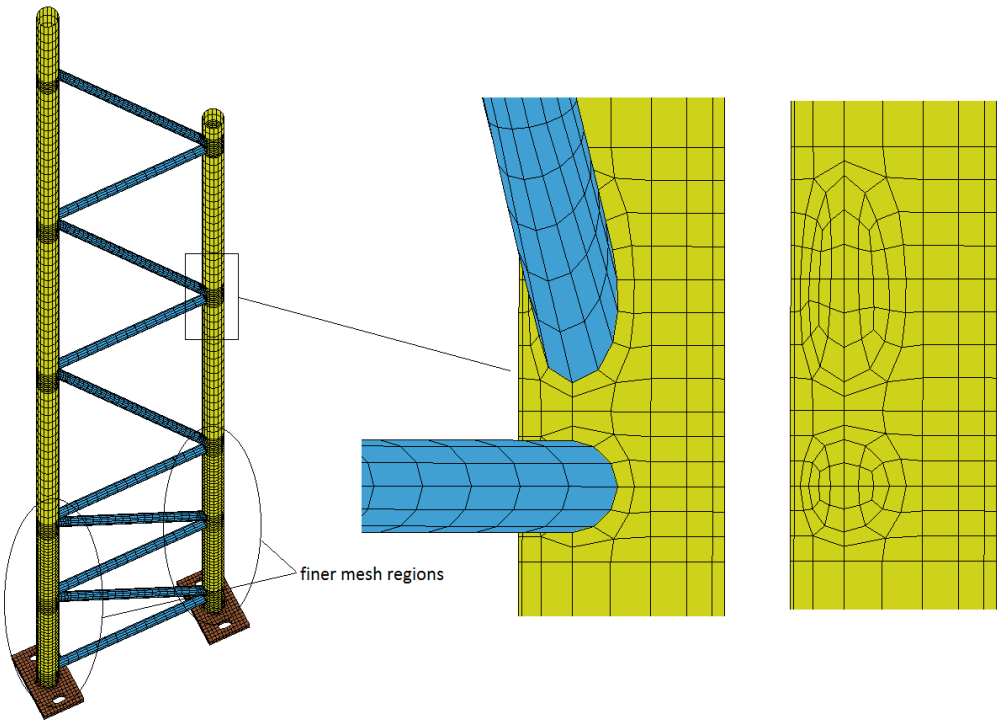


Figure 3.2: Truss mesh. **Left:** perspective view of the truss. **Middle:** mesh detail at the connection. **Right:** mesh detail of the vertical pipe only.

The mesh of the truss consists of 9367 shell elements and is more fine at the bottom part around the impact region, for more accurate simulation of the contact and the element failure and thus more realistic results. For the modelling of the steel pipes, shell elements were preferred compared to solid (brick) elements and unidimensional beam elements. Shell elements are more appropriate than solid elements in that case, due to the fact that the thickness of the pipes is one order of magnitude lower than their diameter. In addition, they were preferred compared to beam elements for realism and accuracy reasons.

A perspective view together with some details of the mesh is shown in Fig. 3.2. It should be noted that for the connection between the vertical and the smaller pipes, shared nodes were used and thus the truss is modelled as a monolithic structure.

### 3.1.2 Plates

The plates that support the truss (see Fig. A.1 right, middle in Appendix A.1), were discretized using 520 solid elements each (see Fig. 3.2 and 3.3), with two elements along the plate thickness.

Solid elements are more appropriate in modelling the geometry and calculating the stresses of that specific part and for that reason they were preferred.

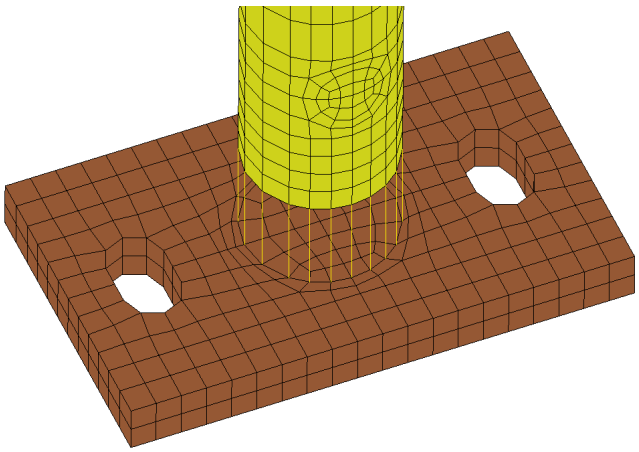

Figure 3.3: Mesh detail at the connection of the vertical pipe to the supporting plate.

The attachment of the columns of the truss to the supporting plates, was managed using welded connections. For that reason the plates were meshed in such a way, so that the bottom nodes of the attaching column to be coincident (but not shared) with nodes on the upper surface of the plate. In Fig. 3.3, the yellow lines show the pairs of coincident nodes welded together. The numerical treatment of the welded connections was achieved using the LS-DYNA keyword *CONSTRAINED_ GENERALIZED_ WELD_ FILLET (see Appendix C.1).

For each pair of nodes a different keyword card was used. For this specific welded connection, it is possible to assume failure criteria for both ductile and brittle failure. These two types of weld failure, were enabled to act together so that failure occurs if one of the two criteria is met.

Ductile failure occurs if the strain of the weld exceeds the specified value of the effective plastic strain at failure $\epsilon^p_{fail}$. This quantity enters the calculations as the internal parameter EPSF and its value was chosen equal to $0.150$ which is close to the effective plastic strain at failure of the steel shown in Fig. 3.11 in section 3.1.5.

The brittle weld failure criterion is described by Eq. (3.1),

$$\sqrt{\sigma_n^2 + 3(\tau_n^2 + \tau_t^2)} \geq \sigma_f \tag{3.1}$$

where

$\sigma_n =$ normal stress
$\tau_n =$ shear stress in direction of weld (local y)
$\tau_n =$ shear stress normal to weld (local x)
$\sigma_f =$ failure stress.

The failure stress $\sigma_f$ has a deterministic value of $0.360$ GPa which is close to the failure stress of the steel. It enters the calculations with the parameter name SIGF. The component $\sigma_n$ is non-zero for tensile values only. In Fig. 3.4 the ordering of the nodes as well as the orientation, is shown for the 2 node fillet welds. This order is with respect to the local coordinate system where the local $z$ axis determines the tensile direction [36].

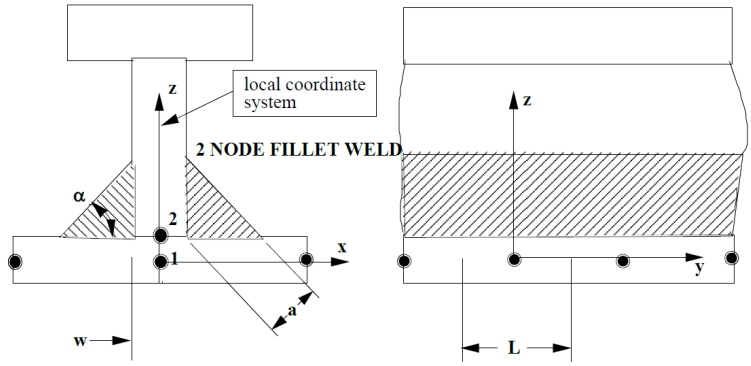


Figure 3.4: Details, nodal ordering and orientation of the local coordinate system for fillet weld.

The additional parameters for the definition of the weld are:

$$\begin{aligned} \text{length } L &= 10.50 \text{ mm} \\ \text{flange width } W &= 70.00 \text{ mm} \\ \text{thickness } a &= 3.00 \text{ mm} \\ \text{angle } \alpha &= 45° \end{aligned}$$

Each plate is being supported by two cylindrical parts used to model the behaviour of bolts (see Fig. 3.5). The nodes of the bottom surfaces of the bolts are fixed. The diameter of the bolts is 22 mm and their length 80 mm. Each of them is meshed using 55 solid elements. It should be noted that the bottom surface of the plates has an offset distance of 30 mm from the road.

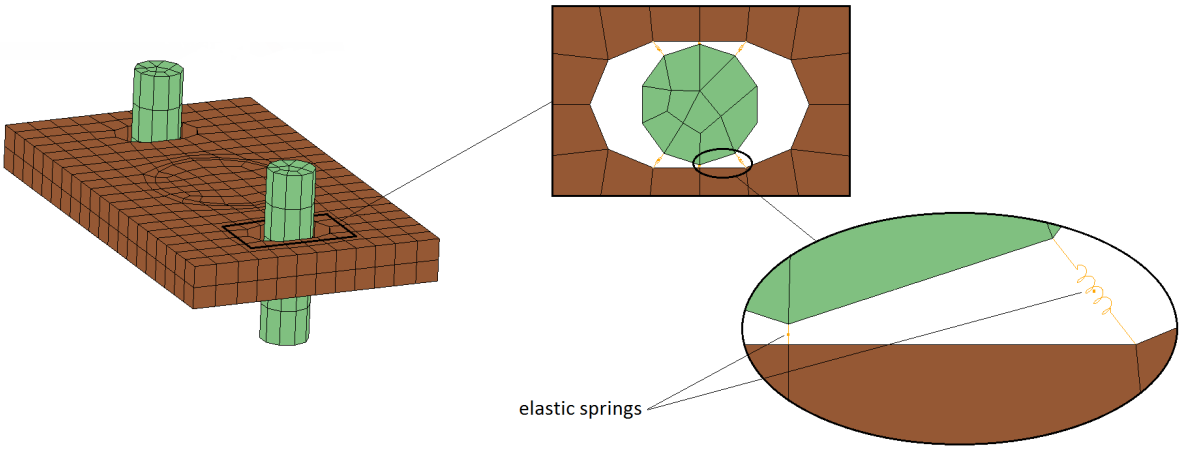


Figure 3.5: **Left:** perspective view of a plate and the bolts. **Right:** details of the connection between plate and bolt using elastic springs.

The connection between one bolt and the plate in modelled using 12 elastic spring elements. The spring elements lie on the horizontal (x - y) plane and connect nodes around the hole, with nodes on the bolt. Six springs are used at the top surface of the hole and another six at the bottom. The use of elastic springs for the representation of that specific connection, is a simple approach and thus the stiffness of the spring does not have an actual physical significance. As a result, the choice of a value for the elastic stiffness is a difficult task and for that reason it was chosen as an uncertain parameter as described in chapter 6. Even so, a deterministic value of that stiffness is needed to be used as an important value for the uncertainty analysis. For that purpose, a test was performed using LS-DYNA.

The idea is to associate the total stiffness of the connection with the elastic constant $K$ of one spring which is the value required as input parameter of the code. The solution of that problem is very difficult to be solved analytically because the total stiffness of the connection does not only depend on $K$ but also on the number of springs, their orientation and the specific connection geometry.

At first, the plate only was fixed at the nodes where the springs are connected (24 nodes). Then a static horizontal body load was applied to the plate and the load multiplier $f$ was chosen so that at the region of the fixities the steel reaches its elastic limit, $\approx 0.235$ GPa (see Fig. 3.6). The horizontal displacement $s$ of a specific node $i$ was measured. Subsequently, the total connection (plate, springs and fixed bolts) was employed, but the plate and the bolts were turned to un-deformable, rigid parts. The same load multiplier $f$ was applied and $K$ was chosen so that the displacement of the same node $i$ was equal to $s$. This value of $K$ was approximately $450$ kN/mm.

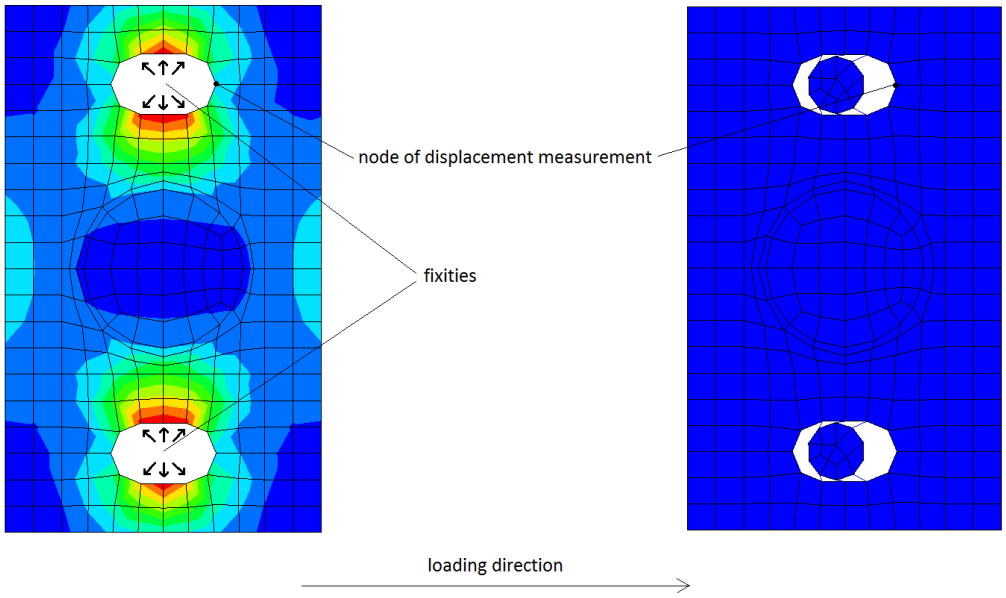


Figure 3.6: Numerical experiment for an approximate assessment of the spring elastic stiffness $K$. **Left:** $1^{st}$ step - Von Misses stresses contour plot, maximum value (red colour) $\approx 0.236$ GPa. **Right:** $2^{nd}$ step - un-deformable parts, deformation of the springs only.

This method, does not by any means provide a realistic value for the constant $K$ of the springs, because several aspects like the actual loading conditions as well as the material and geometrical non-linearities have not been taken into account. The material non-linearities have been excluded by definition due to the usage of elastic springs. The geometrical non-linearity however, arising from the fact that the relationship between $K$ and the total connection stiffness is not linear, is a more significant source of inaccuracy in that case. It has not been taken into account due to the fact that only one point, at the yielding of the steel, was considered. In addition to that, the test is based on the deformation of the plate only and not the bolt and the nut.

In a more realistic approach, a damper could be used parallel to each elastic spring in order to properly describe the dynamical behaviour of the connection. In that case, a similar numerical experiment, dynamic this time, could be employed to determine the damping coefficient.

### 3.1.3 Sign

For the representation of the sign, a plane part 3.0 m x 3.0 m with rounded corners is used (the capital letter S will be occasionally used in the latter to denote that part), and modelled by shell elements. The thickness of the sign is 2.5 mm as suggested by [3]. The sign is attached to a frame which also contains 3 horizontal reinforcing beams in the middle (see Fig. 3.7 and A.1 left, in Appendix A.1). The frame and the reinforcing beams consist one part (part F), thus they are connected to each other using shared nodes and they have the same thickness of 10 mm. The frame has exactly the same dimensions with the sign in the vertical (y - z) plane and a width of 50 mm along the x direction (see Fig. 3.7). These dimensions were derived from actual drawings of a similar structure. The sign and the frame are binned together using shared nodes (connection F - S in Table 3.2). Drawings of the sign with the corresponding dimensions are shown in Fig. 3.8.

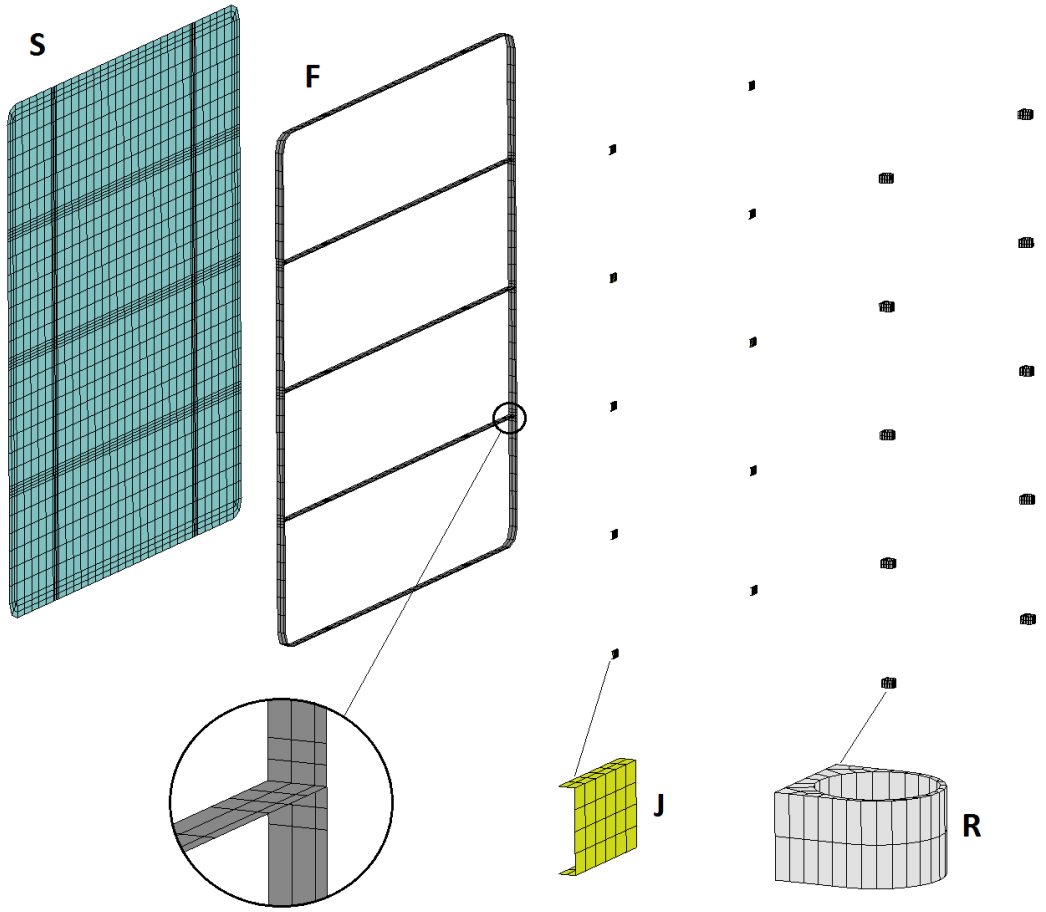


Figure 3.7: Exploded view drawing of the sign, the frame and the connection parts. **Upper:** sign assembly. **Lower:** mesh details of the frame and connection parts.

The sign is supported by two vertical trusses (see Fig. 3.2) at a height of 1.25 m (bottom line of the sign). Each truss is connected to the sign frame at five points, one at the top, one at the bottom and three at the reinforcing beams (see Fig. 3.7). For that connection two additional parts were used, one ring (part R) which is fixed on the column (connection T - R in Table 3.2) of the truss and one rectangular part (part J) welded on the frame (connection J - F). The ring is modelled by solid elements while the rectangular part by shell elements. The connection between these two parts is achieved using one elastic spring (connection R - J) as shown in Fig. 3.9.

Table 3.1, summarizes all the parts used within the numerical model of the structure (sign and supporting trusses) together with some information about the elements used to model each part.

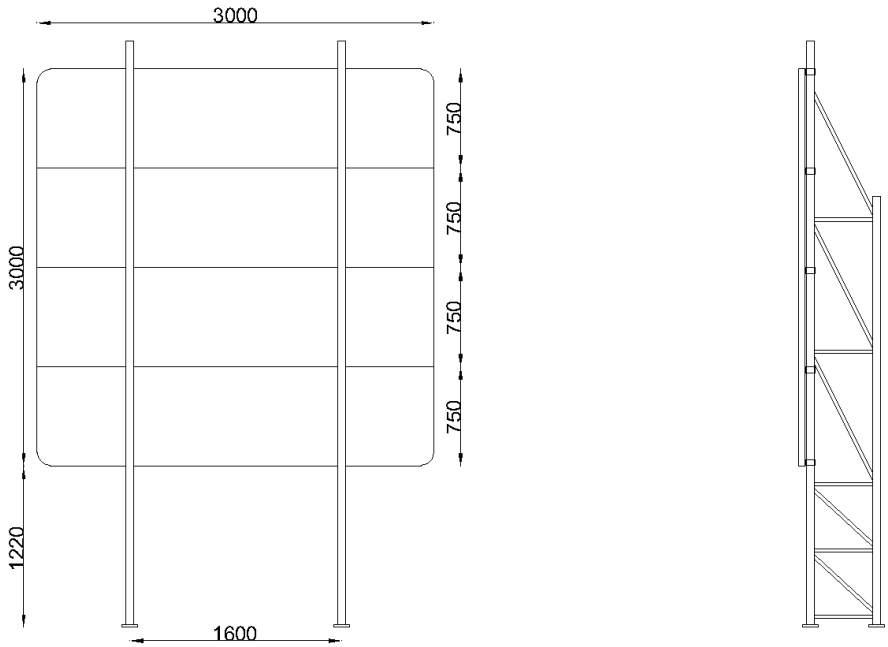


Figure 3.8: Drawings of the sign, dimensions in mm. **Left**: y-z view. **Right**: x-z view.

Table 3.1: Summary table of the parts in the model

| Part | abbreviation | multitude | element type | number of elements | totals |
|---|---|---|---|---|---|
| Truss | T | 2 | shell | 9367 | 2 x 9367 = 18734 |
| Plate | P | 4 | solid | 520 | 4 x 520 = 2080 |
| Bolt | B | 8 | solid | 55 | 8 x 55 = 440 |
| Sign | S | 1 | shell | 1836 | 1 x 1836 = 1836 |
| Frame | F | 1 | shell | 846 | 1 x 846 = 846 |
| Ring | R | 10 | solid | 64 | 10 x 64 = 640 |
| Rectangular connection | J | 10 | shell | 48 | 10 x 48 = 480 |
| Base spring | BS | 96 | spring | 1 | 96 x 1 = 96 |
| Connection spring | CS | 10 | spring | 1 | 10 x 1 = 10 |
| | | | | | 25162 elements |

### 3.1.4 Connections

For the connection between the rectangular part and the frame (connection J - F in Table 3.2), spot welds were used. The numerical treatment of the spot welds was achieved using the LS-DYNA keyword *CONSTRAINED_ SPOTWELD (see Appendix C.1). The purpose of that specific keyword is to define massless spot welds between non-contiguous nodal pairs. The spot weld is a rigid beam that connects the nodal points of the nodal pairs; thus, nodal rotations and displacements are

coupled. The spot welds must be used between nodes having rotary inertias, i.e., beams or shells. Note that shell elements do not have rotary stiffness in the normal direction and, therefore, this component cannot be transmitted. Spot welded nodes must not have the same coordinates.

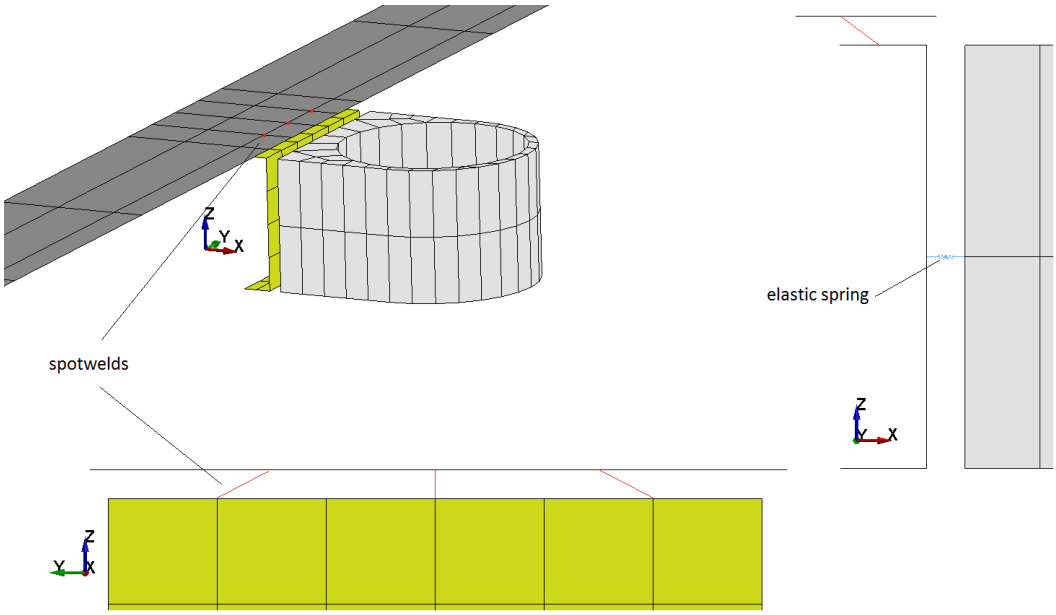


Figure 3.9: Connections details. **Upper left:** Perspective view of the connection. **Right:** X - Z view. **Lower:** Y - Z view.

Moreover, brittle and ductile failures can be specified, but in the present thesis failure of these spot welds has not been taken into account. As a result, the failure of the total connection (T - R, R - J, J - F) between the truss (T) and the frame (F), depends on the strength of the rectangular J part only. It is the part that fails during the simulation and controls the disjoining of the sign and the truss.

The binding of the rectangular part on the ring (connection R - J), is achieved using one elastic spring. The use of the elastic spring for that particular connection, has the meaning of allowing some rotation and for having a connection that is not completely rigid. The elastic constant of that spring was chosen equal to $4000\ \mathrm{kN/mm}$. This is equivalent to an elastic steel rod with cross sectional area $76.2\ \mathrm{mm}^2 \approx \varnothing 10$ [1] or $2\varnothing 7$ according to Eq. (3.2).

$$\left.\begin{aligned} &\text{elastic spring:} && F = K \cdot \delta x \\ &\text{elastic rod:} && \sigma = E \cdot \epsilon \\ & && \sigma = \frac{F}{A} \\ & && \epsilon = \frac{\delta x}{L} \end{aligned}\right\} \Rightarrow A = \frac{K \cdot L}{E} = 76.2\ \mathrm{mm}^2 \tag{3.2}$$

[1] The notation $\varnothing 10$ is equivalent to the expression "rod of diameter $10\ \mathrm{mm}$".

Where

$F =$ axial force
$K =$ elastic constant of the spring $= 4000\ \mathrm{kN/mm}$
$\delta x =$ axial displacement
$\sigma =$ axial stress of the rod
$E =$ young modulud of the material (steel) of the rod $= 210\ \mathrm{GPa}$
$\epsilon =$ axial strain of the rod
$A =$ cross section area of the rod
$L =$ length of the rod $= 4\ \mathrm{mm}$.

The total connection (R - J, J - F) was numerically tested with LS-DYNA to check intuitively the performance of the spot welds and the failure of the rectangular part. The inner nodes of the ring were fixed, while the sign and it's frame, were pulled along the horizontal direction. The result is shown in Fig. 3.10 by means of Von Misses stress distribution for increasing loading step.

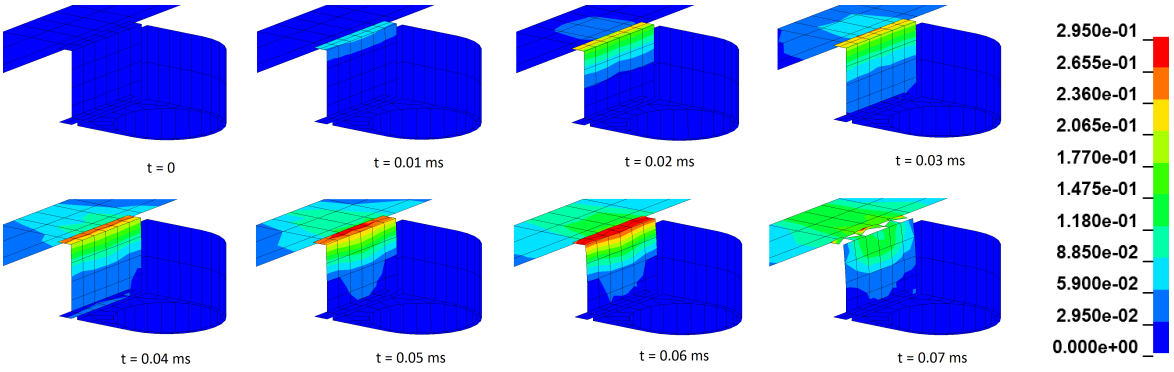


Figure 3.10: Illustration of the failure of the connection using a numerical pull-out test.

Note in Fig. 3.10, that the yielding stress of the steel ($0.235\ \mathrm{GPa}$), was chosen at the transition from yellow to orange colour in the Von Misses stresses contour plot. As a result the regions in orange and red colour are in the post-yielding branch of the stress-strain relationship (see section 3.1.5).

Table 3.2, summarizes all the connections between the mentioned parts.

Table 3.2: Summary table of the connections in the model

| Connecting parts | connection type | number of connecting nodes for one connection | number of connections in the model |
|---|---|---|---|
| B - P | spring (BS) | 12 | 8 |
| P - T | fillet welds | 18 | 4 |
| T - R | tied nodes to surface | 72 (on R) | 10 |
| R - J | spring (CS) | 1 | 10 |
| J - F | spot welds | 3 | 10 |
| F - S | shared nodes | - | 1 |

In the T - R connections, all the 72 inner nodes of the ring (part R) are tied on the surface of the attaching column of the truss. For that connection the LS-DYNA keyword *CONTACT_ TIED_ NODES_ TO_ SURFACE_ CONSTRAINED_ OFFSET (see Appendix C.1, also discussed in section 4.5) is used. This is a contact type keyword that constraints all the translational degrees of freedom of the defined nodes, to move together with the closer segment of the defined surface. As a result, there is not any relative movement between the ring and the corresponding column.

### 3.1.5 Materials

Structural materials used in real world application, almost always exhibit a non-linear, inelastic behaviour which can be observed in the stress-strain diagram. Especially structural steel, exhibits an elasto-plastic stress-strain behaviour characterized by a steep linear elastic pre-yielding part and a post-yielding part where the material becomes gradually incapable in bearing larger stresses without significant deformation (see Fig. 3.11).

In practical applications, often involving numerical calculations, simplicity and computational efficiency is an issue. For that reason, in the present thesis, the simple approach of a bi-linear curve, with hardening plasticity is adopted to describe the non-linear material behaviour. This bilinear curve model, consists of one line for the pre-yielding, elastic part and another one for the post-yielding, plastic part (see Fig. 3.11). This bi-linear material model, is in accordance with [5], where it is suggested that the yielding stress $f_y$ should be equal to the nominal value of the class of the steel, hence $S235 \Rightarrow f_y = 0.235$ GPa. Moreover, due to ductility requirements, the ultimate strain $\epsilon_u$ should be $\geq 15\ \%$ and for the ratio of the ultimate stress to the yielding stress should hold $f_u/f_y \geq 1.10$. In the present thesis, the values $\epsilon_u = 15\ \%$ and $f_u/f_y \approx 1.53 > 1.10$ are adopted (see Table 3.3).

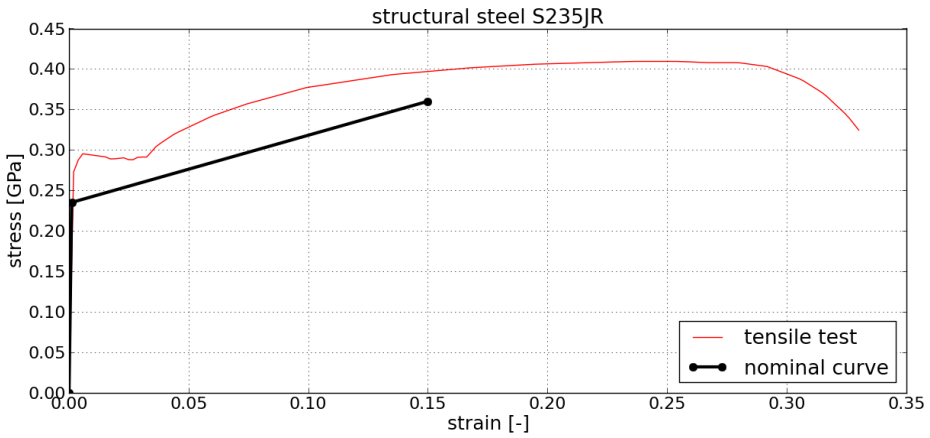


Figure 3.11: Stress-strain diagram of the structural steel of class S235JR.

In Fig. 3.11, the experimental values were derived from [25] after tensile tests in accordance with the testing requirements of [5]. The black line depicts the bilinear stress-strain model adopted in the studies of the present thesis. It should be noted that the term stress, refers to the term *engineering stress* which is calculated with constant cross sectional area [2]. Similarly, the term strain refers to *engineering strain* because it is measured with constant length of specimen [3].

[2] By definition stress is the ratio of the applied force F, divided by the cross sectional area A. In practical applications, it is more convenient to use a constant value for A, equal to its initial value, before the loading. In tensile tests however, the area A may significantly change during the loading process. A stepwise calculation of the stress with consideration of the cross section thinning in each loading step, is referred to as *true stress* to be distinguished from the standard, constant A, calculation which is known as *engineering stress*.

[3] By definition strain is the sum of the differences $\mathrm{d}\epsilon = \mathrm{d}l/l$ during the calculation. Based on that definition, it is possible

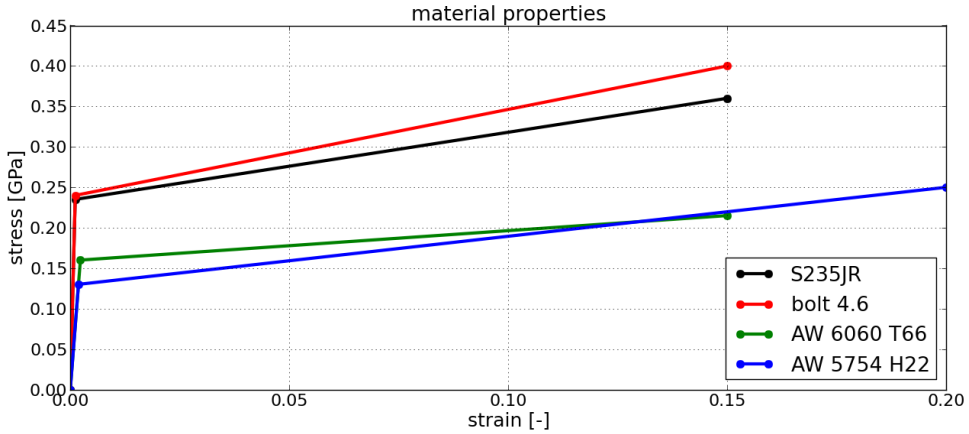


Figure 3.12: Stress-strain assumptions for the structural materials.

Similar bi-linear models with hardening plasticity were employed for the mechanical description of the other three materials used in the numerical model of the structure. Apart from the support structure, for which the standard steel S235JR, in accordance with [5] was used, according to the design the bolts were classified as grade 4.6 in accordance with [8]. Moreover, the frame and the sign were constructed by the aluminium alloys AW 6060 T66 and AW 5754 H22 respectively, in accordance with [6]. The adopted non-linear models for the four materials are shown in Fig. 3.12 and the reference values can be found in Table 3.3. The adopted values were derived equal to the minimum values suggested from the corresponding standards ([5] for steel and [6] for aluminium).

Table 3.3: Summary table of the materials used in the present studies

| Material | Young's modulus E [GPa] | Tangent modulus $E_T$ [GPa] | yield stress $f_y$ [GPa] | ultimate stress $f_u$ [GPa] | yield strain $\epsilon_y$ [-] | ultimate strain $\epsilon_u$ [-] |
|---|---|---|---|---|---|---|
| Steel S235JR | 210 | 0.83960 | 0.235 | 0.360 | 0.00112 | 0.15 |
| Steel bolt 4.6 | 210 | 1.07486 | 0.240 | 0.400 | 0.00114 | 0.15 |
| Aluminium AW 6060 T66 | 69 | 0.37242 | 0.160 | 0.215 | 0.00231 | 0.15 |
| Aluminium AW 5754 H22 | 69 | 0.60571 | 0.130 | 0.250 | 0.00188 | 0.20 |

An important aspect concerning the material properties in the present study, is the relationship between ductility and passive safety of non-energy absorbing structures. Large $\epsilon_u$ means that more energy is being absorbed by the material. In ordinary structural applications, the assumption of lower material ductility ($\epsilon_u = 15\ \% = \epsilon_u^{min}$) than observed in experiments ($\epsilon_u > 30\ \%$) is an action towards safety. The distinctiveness of non-energy absorbing structures, is that the structure is intended to fail, this is what makes it passively safe. Since failure is desirable, it should not be underestimated.

---

to calculate the *true strain* as

$$\epsilon_T = \int \mathrm{d}\epsilon = \int_{l_0}^{l_f} \frac{\mathrm{d}l}{l} = \ln \frac{l_f}{l_0}$$

where $l_0$ and $l_f$ refer to the initial and the final values of the specimen length. Given that the engineering strain $\epsilon_E$ is equal to $(l_f - l_0)/l_0$ it is possible to relate the two strains by,

$$\epsilon_T = \ln \frac{l_f}{l_0} = \ln \frac{l_0 + \Delta l}{l_0} = ln(1 + \epsilon_E)$$

### 3.1.6 Element technology

For the efficient Finite Element Analysis of the vehicle-structure impact problem, appropriate element types are required, that combine numerical efficiency, computational speed, robustness, stability and accuracy. It has been observed, that triangular shells and pentagonal and tetrahedral solids are too stiff and should not be used except where absolutely needed [18]. For that reason, the mesh of the structure consists almost entirely by quadrilateral shells and hexahedral solids (see Fig. 3.2).

The elements for non-linear transient codes can be simple, robust, and highly efficient. It has been shown, that in crash simulations, it is more efficient to have a large number of simple elements than a smaller number of higher-order, multi-point integration elements [18]. For that reason the Hughes-Liu shell element was chosen to describe the behaviour and calculate the stresses of the shell elements in the numerical model of the structure. For the numerical processing of the solid elements involved in the model, the standard, constant stress, one-point integration element was chosen.

#### Hughes-Liu shell element

The Hughes-Liu shell element was introduced by [29, 30] and implemented in LS-DYNA after the work of [23]. It is a simple, one integration point 3D shell element, based on a degenerated brick element formulation. A schematic view of this approach, originated by [9] is shown in Fig. 3.13, where $\xi$, $\eta$ and $\zeta$ are the parametric coordinates. Due to this characteristic, the Hughes-Liu shell element is compatible with brick elements and thus, it allows the use of many efficient and effective techniques developed for brick elements. Moreover, according to [24], it is incrementally objective (rigid body rotations do not generate strains), allowing for the treatment of finite strains that occur in many practical problems. In addition to that, this particular element type includes finite transverse shear strains. The simplicity of the Hughes-Liu shell element, which usually translates into computational efficiency and robustness, makes it quite popular among the non-linear Finite Element Analysis codes.

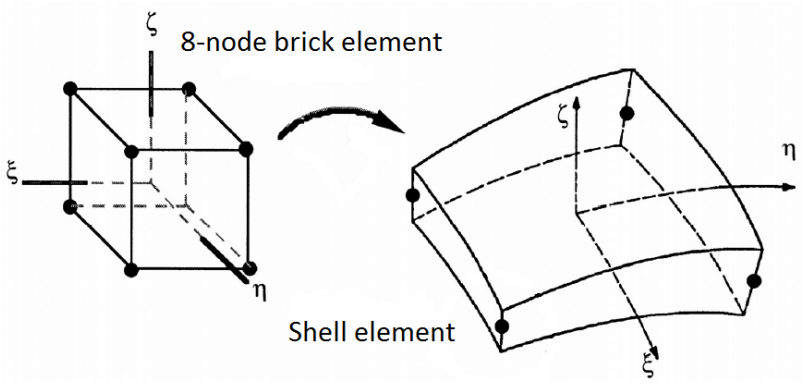


Figure 3.13: Schematic view of the 8-node brick element and the shell element.

In the shell geometry, planes of constant $\zeta$ define the lamina of layers of the shell while fibers are defined by through-the-thickness lines when both $\xi$ and $\eta$ are constant (usually only defined at the nodes and thus referred to as "nodal fibers"). To degenerate the 8-node brick geometry into the 4-node shell geometry, the nodal pairs in the $\zeta$ direction (through the shell thickness) are combined into a single node, for the translational degrees of freedom, and an inextensible nodal fiber for the rotational degrees of freedom. Detailed information concerning the geometry, the kinematics, the

strains and stress update formulas as well as the elements mass matrix can be found in [29] and in [24]. Another efficient, one-point integration shell element widely used in modern codes like LS-DYNA, is the Belytschko-Lin-Tsay shell element introduced by [10].

Nearly 10 % of the elements of the structure are solid elements. The solid elements are modelled using the standard LS-DYNA constant stress element, which is an 8-node brick element with one integration point.

**Element failure**

The applied failure criterion is based on strains; when the effective plastic strain [4] within an element reaches the maximum-specified value, the element is deleted from the calculation. This is a simple approach of failure and requires fine meshing close to the failure region for accuracy. The main advantage of the combination between: a) strain dependent element deletion as failure criterion and b) sufficiently fine mesh at the failure region, is simplicity. This is usually translated to computational efficiency.

In particular, for impact simulations, it is desirable to have small time steps in order to compute the kinematic quantities more accurate. The usage of small time steps, provides accuracy on the one hand but increases the computational cost on the other. In order to confront the high cost, an explicit integration scheme was chosen; based on the same reasoning, this simplified failure criterion was applied.

The fact that failure is based only on the effective plastic strain $\epsilon^p_{eff}$, makes the choice of that value important. It is common in numerical calculations to assume a total strain of 15 %, which is the minimum value defined in [5]. In Fig. 3.11, it is shown that experimental results of tensile tests of the standard steel S235, exhibit total strains larger than 30 %. The choice of the minimum value of 15%, seems sensible in usual applications like buildings, cars, etc. This is because of four reasons, a) higher strength steels fail under much smaller strains, b) the exact loading conditions are not precisely known, c) the uncertainty rising from the simplified calculations and d) a choice of a smaller than the real value for $\epsilon^p_{eff}$, is towards safety.

In passive safety assessment however, an underestimation of the ultimate strain, is not towards safety. In fact, the area under the plastic part of the stress-strain curve, in Fig. 3.11, represents the dissipated energy (through plastic deformation). It is evident that an underestimation of the ultimate strain, results to an underestimation of the dissipated energy. In a structure that it is desirable to fail as in non-energy absorption passive safely structures, if the predicted absorbed energy is lower than the real, then the resulting accelerations may have been underestimated. This is not towards safety because it increases the impact severity and thus the injury risk.

This observation, gives rise to further considerations over the used limit value of $\epsilon^p_{eff}$. A larger value of that parameter may be more appropriate in the case of non-energy absorbing passively safe structures. This is not valid for high energy absorbing structures, like roadside restraint bars, because their passive safety is not based on failure but on energy dissipation only. They are structures that it is not desirable to fail but to deform. As result, the underestimation of the ultimate strain is a secure choice.

[4] The term *effective plastic strain* $\epsilon^p_{eff}$, refers to the post yielding part of the strain. It is though unnecessary to distinguish it from the total strain, because a minimum value of $\epsilon^p_{eff}$ 15 % represents the 99 % of the total strain in steel.

### Locking

Locking is the phenomenon when Finite Elements exhibit an un-physically stiff behaviour. The locking effect appears as *shear locking* and *volumetric locking*.

Shear locking is associated with an error in the Finite Element solution, that occurs because the standard quadrilateral elements cannot accurately approximate the strain distribution associated with bending. This error rises when linear interpolation functions are used in multi-point integration elements. At the integration points, in that case, the ratio $\epsilon_{12}/\epsilon_{11}$ between the shear strain and the tensile strain, is proportional to the aspect ratio *b/h* (element dimensions). This has the effect that as the aspect ratio decreases, the shear strain and not the tensile strain tends to carry the load. Mesh refinement is a simple, but not always feasible solution to that problem. Moreover, the use of one-point integration elements, eliminates that problem because then the linear interpolation functions become sufficiently accurate in describing bending.

Volumetric locking has the same cause (i.e. inaccurate bending representation by linear interpolation functions in multi-point integration quadrilateral elements) and the same effect (stiff behaviour) with shear locking, but a different influencing mechanism. It occurs when incompressible materials (poison's ratio $\nu = 0.5$) are used, because the linear interpolation functions are unable to properly approximate a strain field that satisfies the incompressibility constraint $\epsilon_{11} + \epsilon_{22} = 0$ (for plain, 2D problem). The materials used in the present thesis, as most of the structural materials, are compressible ($\nu \approx 0.3$) and thus volumetric locking is not of concern. It is more important in rubber modelling and difficult to treat because it can not be eliminated by mesh refinement. For the same reasons like in shear locking, volumetric locking vanishes when one-point integration elements are used.

Locking is not of great importance in the studies of the present thesis, because only one integration point elements have been used. Such elements suffer from another unfavourable phenomenon, the *hourglass phenomenon* explained below.

### Hourglass phenomenon

The main disadvantage of the Hughes-Liu shell element, as in all the one integration point elements (also brick elements), is the *hourglass phenomenon*. Especially under bending, adjacent shell elements can deform in-plane into non-physical "hourglass" shapes without expending any energy, also referred to as *zero energy modes*, shown in Fig. 3.14. According to [18], the hourglass phenomenon is one of the main and most common problems in transient analysis of dynamical systems. It can be observed even in shell elements with multiple integration points because all these points are through the centre of the element and thus some of the zero energy modes are still possible to occur.

The solution to the hourglassing problem is achieved by the development of advanced algorithms called *hourglass control* that prevent this phenomenon from occurring. These algorithms, in order to suppress the hourglass deformation modes that accompany the one-point integration elements, hourglass viscous-or stiffness-based stresses are added to the physical stresses at the local element level. However, if too much *hourglass energy* is required to prevent the phenomenon, the solution will not be valid. Consequently, the current codes, like LS-DYNA, calculate and output hourglass energy during a simulation; these values should always be checked by the user to determine if excessive hourglass energy is present.

The hourglass phenomenon is illustrated with the aid of the simulation of a planar plate, pulled along it's plane direction. The results are shown by means of Von Misses stresses in Fig. 3.15, the

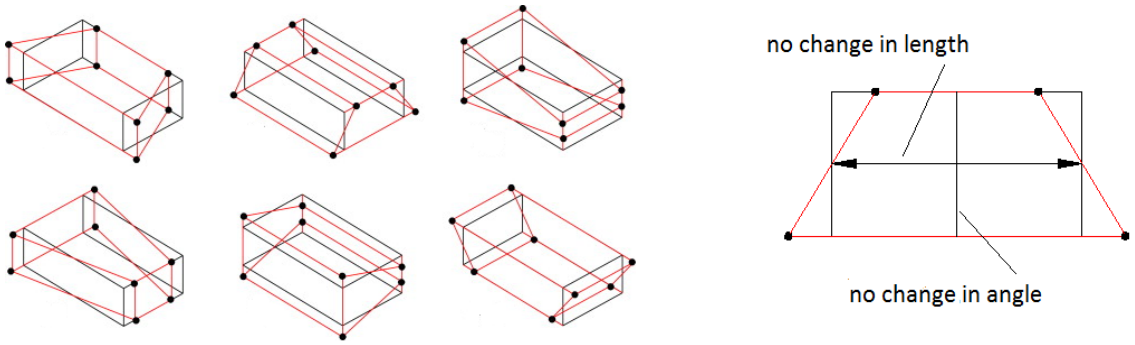


Figure 3.14: Hourglass phenomenon. **Left**: zero energy "hourglass" mode shapes of a brick element. **Right**: illustration of the problem in a 2D shell element.

same fringe levels have chosen and thus the results are comparable from case to case. In the left case, without hourglass control, the deformed shape appears sufficiently affected by hourglass. In the middle case, where viscous form of hourglass control (type 1,2,3 in LS-DYNA) was used, the deformed shape still appears affected and in addition to that a high hourglass energy was required to suppress the phenomenon. Finally, in the right case, the stiffness form of hourglass control (type 4,5 in LS-DYNA), provides the best visual results without the need of extreme values of extra energy.

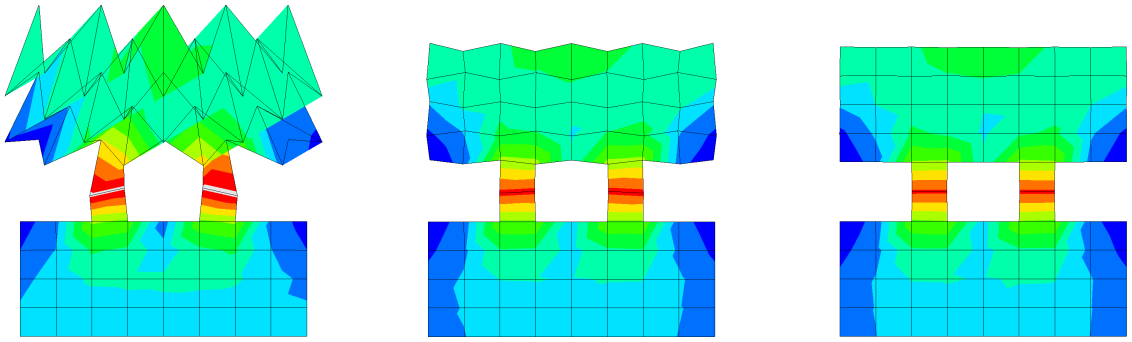

Figure 3.15: Illustration of the hourglass phenomenon. **Left**: no hourglass control, hourglass energy $= 0$. **Middle**: viscous hourglass control, hourglass energy $= 350$ J. **Right**: stiffness based hourglass control, hourglass energy $= 28$ J.

It is suggested by [37], that the use of under-integrated elements together with hourglass control, is extremely economical, in a computational point of view. For that reason this approach was adopted in the studies of the present thesis.

In [36], it is suggested that in crash simulations, the viscous form of hourglass control is more appropriate. Another remark however, states that many users in automotive industry prefer an hourglass control of stiffness form. Both cases were investigated with different assumptions for shell and solid elements, and the conclusion is that stiffness form hourglass control is more effective and is associated with lower levels of additional hourglass energy. For that reason the hourglass type 5, which is the stiffness form of Flanagan-Belytschko hourglass algorithm, that applies to solid and shell elements, was chosen throughout the simulation.

## 3.2 CAR, DUMMY AND ROAD

The numerical model of the vehicle used in the studies of the present thesis, is provided by the National Crash Analysis Center (NCAC) in the U.S. and it contains one Dummy provided by the DYNAmore GmbH, Germany. The car model consist of 16251 elements, the dummy and the seat models consist of 7633 and 7563 elements respectively.

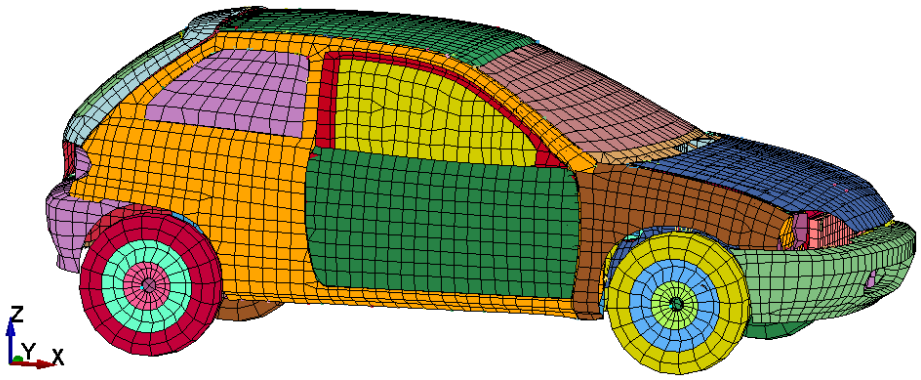


Figure 3.16: Perspective view of the car model.

The road was modelled with the aid of a horizontal (x - y), rectangular plane, discretized by 2500 shell elements. In the calculations, the road is assumed as un-deformable. In addition, no friction is present at the contact between the car tyres and the road.

The dummy used in the simulations, is a numerical model of the standard Hybrid III $50^{th}$ percentile male crash test dummy. It is one of the most widely used humanoid devices for injury assessment in crash tests. The Hybrid III $50^{th}$ dummy, was originally developed by General Motors and it is maintained and developed in conjunction with the Biomechanics Committees of the Society of Automotive Engineers' (SAE). Moreover, it is a regulated test device in the European ECE regulations.

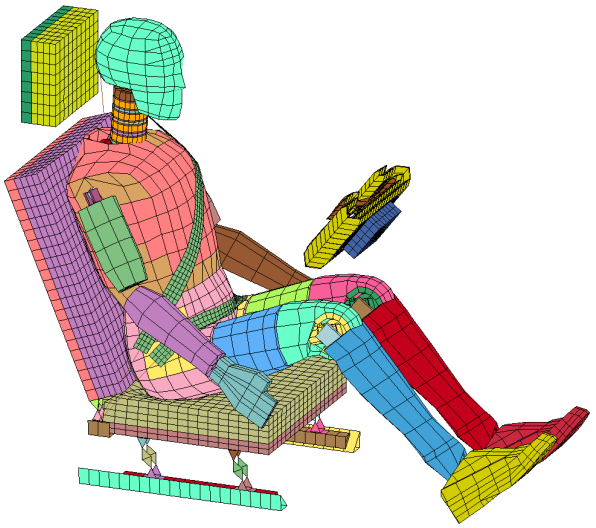

Figure 3.17: Dummy and seat.

The dummy is in contact with the seat, while a numerical model of a seatbelt is used that applies acceleration dependent restraints on the dummy relatively to the seat. In addition to that, a numerical model for the simulation of the behaviour of an airbag is provided as well. The airbag model, is

enhanced by many advanced features available in LS-DYNA, that appropriately treat the difficult task of the airbag simulation. The numerical representation of the membrane that constitutes the outer surface of the airbag, the unfolding process, the inner pressure as well as the activation moment, is possible with the aid of special tools provided by the program.

The masses of the car, the dummy and the seat were calculated from the LS-DYNA output file 'd3hsp' and they are summarized in Table 3.4.

Table 3.4: Mass properties of the car, the dummy and the seat.

| | number of elements | total mass [kg] | mass limits according to [2] [kg] |
|---|---|---|---|
| Car | 16251 | 834.11 | $825 \pm 40$ |
| Dummy | 7633 | 78.52 | $78 \pm 5$ |
| Seat | 7563 | 30.74 | - |
| Total | 31447 | 943.37 | $900 \pm 40$ |

The masses of the vehicle and the dummy, are within the specified mass limits defined in [2]. The total mass exceeds those limits because the car, dummy and seat models have been developed independently and the seat mass has not been taken into account in the car model design.

The dimensional properties of the tested vehicle are summarized in Table 3.5, see also Fig. 3.18 and 3.19. For description of the dimensions of the testing vehicle according to [2], see section 2.3.6. The distances of the centre of gravity, are measured as follows: the longitudinal distance (CGx) from the front axle, the lateral distance (CGy) from the centreline and the height (CGz) from the ground.

Table 3.5: Dimensional properties of the car.

| | dimension [m] | dimensional limits according to [2] [m] |
|---|---|---|
| Width | 1.628 | - |
| Length | 3.750 | - |
| Height | 1.435 | - |
| Frontal overhang | 0.803 | - |
| Wheel base | 2.370 | - |
| Rear overhang | 0.577 | - |
| Front wheel track | 1.385 | $1.35 \pm 0.20$ |
| Rear wheel track | 1.388 | $1.35 \pm 0.20$ |
| CGx | 0.851 | $0.90 \pm 0.09$ |
| CGy | 0.536 | $0.00 \pm 0.07$ |
| CGz | 0.0304 | $0.49 \pm 0.05$ |

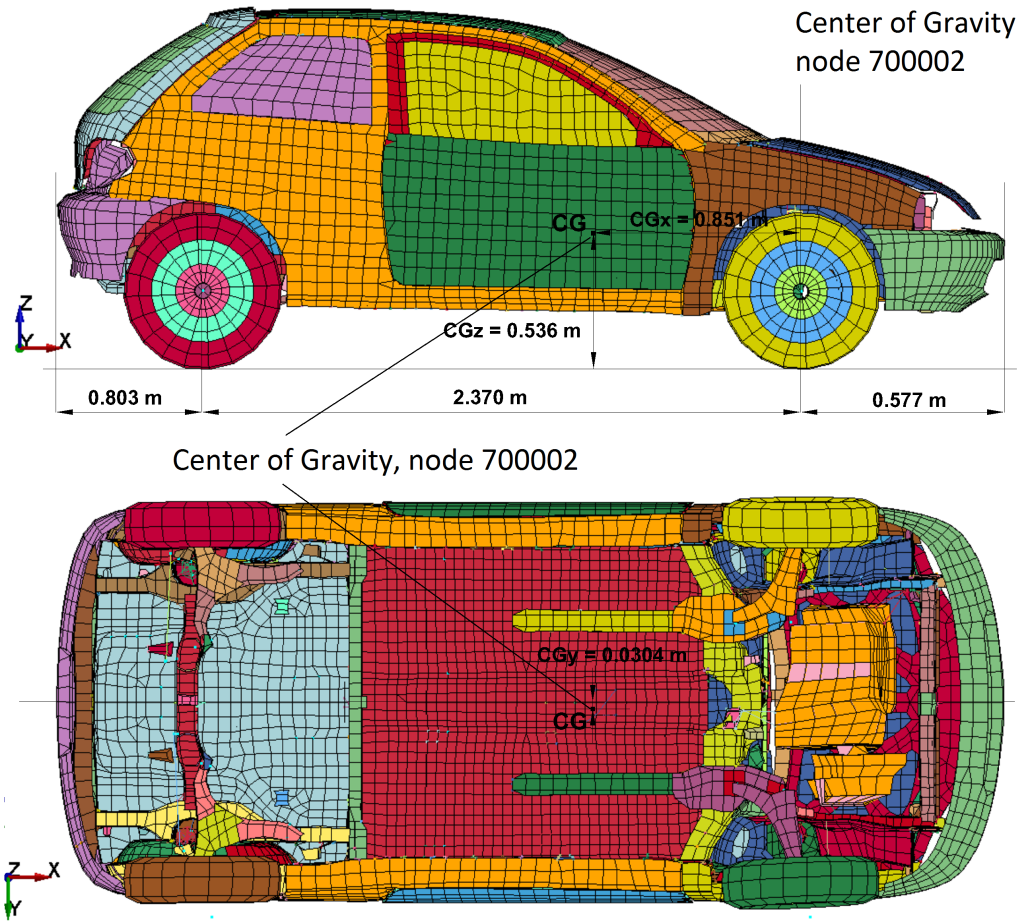


Figure 3.18: Lateral and bottom view of the car model.

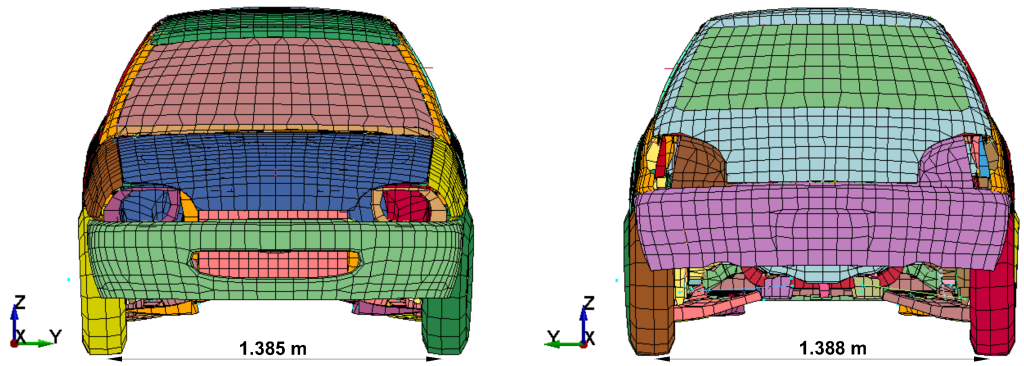


Figure 3.19: Front and back view of the car model.

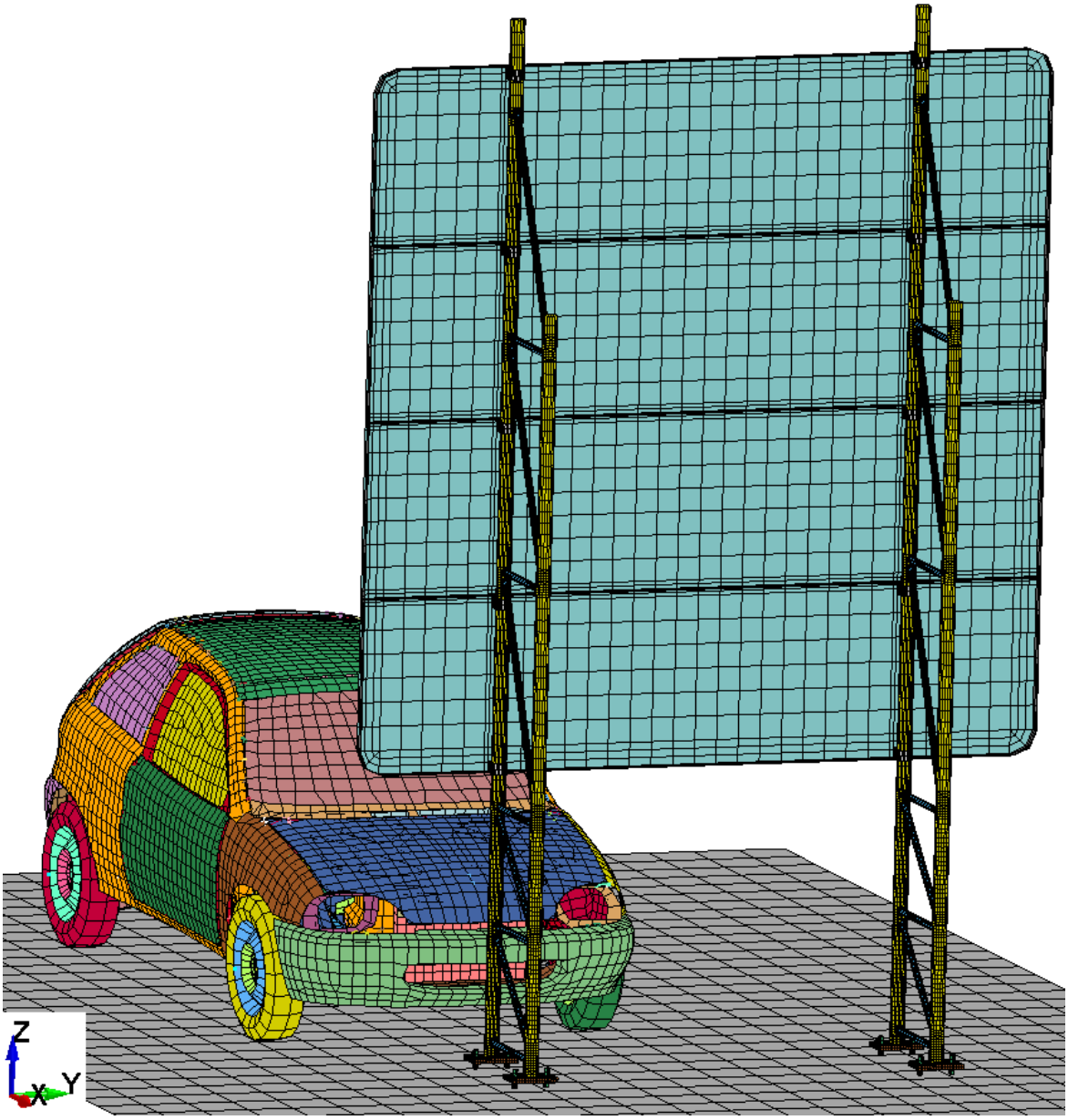


Figure 3.20: Perspective view of the whole simulation.

# 4 ANALYSIS

## 4.1 STRAIN AND STRESS UPDATE

In elastic-plastic materials, stresses are integrated incrementally in time. In the present section the equations for the transition from the stress state n to the state n+1 are quoted. In a typical time step, the coordinates of a body at step n+1 may be represented by a function of the coordinates at step n and the step length $\Delta t$ (see Eq. (4.1)).

$$\mathbf{y}^{n+1} = \mathbf{y}^{n+1}(\mathbf{y}^n, \Delta t) \tag{4.1}$$

The displacement increment over the step is shown in Eq. (4.2). In addition to that consider the 'midpoint' coordinates in Eq. (4.3).

$$\boldsymbol{\delta} = \mathbf{y}^{n+1} - \mathbf{y}^n \tag{4.2}$$

$$\mathbf{y}^{n+1/2} = (\mathbf{y}^n + \mathbf{y}^{n+1})/2 \tag{4.3}$$

It is possible now to define the incremental displacement gradient **G** as the gradient of $\boldsymbol{\delta}$ with respect to $\mathbf{y}^{n+1/2}$. The gradient **G** is shown in component form in Eq. (4.4).

$$G_{ij} = \frac{\partial \boldsymbol{\delta_i}}{\partial \mathbf{y}_j^{n+\frac{1}{2}}} \tag{4.4}$$

The incremental strain and rotation tensors, may be defined as the symmetric and the skew-symmetric parts of **G** respectively, see Eq. (4.5) and (4.6).

$$\Delta\epsilon_{ij}^{n+\frac{1}{2}} = \frac{1}{2}(G_{ij} + G_{ji}) \tag{4.5}$$

$$\Delta\omega_{ij}^{n+\frac{1}{2}} = \frac{1}{2}(G_{ij} - G_{ji}) \tag{4.6}$$

A first, partial update of the stresses, may be understood as the rotation of the Cauchy stress tensor $\boldsymbol{\sigma}^n$ in step n using the incremental rotation tensor $\Delta\boldsymbol{\omega}$, shown in Eq. (4.7) in component notation.

$$\underline{\sigma}_{ij}^{n+1} = \sigma_{ij}^n + \sigma_{ip}^n \Delta\omega_{pj}^{n+\frac{1}{2}} + \sigma_{jp}^n \Delta\omega_{pi}^{n+\frac{1}{2}} \tag{4.7}$$

The bar '_' under the stress symbol in Eq. (4.7), denotes the term 'partial', that the update is not yet complete. A component that describes the material deformation is still required. For that reason the partially updated stress tensor $\underline{\boldsymbol{\sigma}}^{n+1}$ and the incremental strain tensor $\Delta\boldsymbol{\epsilon}^{n+1/2}$ should be transformed to the local coordinate system using the transformation matrix **q** (see Eq. (4.8) and (4.9)).

$$\underline{\sigma}_{ij}^{l^{n+1}} = q_{ik}\underline{\sigma}_{kn}^{n+1} q_{jn} \tag{4.8}$$

$$\Delta\epsilon_{ij}^{l^{n+\frac{1}{2}}} = q_{ik}\Delta\epsilon_{kn}^{n+\frac{1}{2}} q_{jn} \tag{4.9}$$

The superscript 'l' in Eq. (4.8) and (4.9), is used to denote the local coordinate system. The second partial update of the stresses, which gives the final updated Cauchy stress tensor $\boldsymbol{\sigma}^{l^{n+1}}$ in the local coordinate system, is shown in Eq. (4.10).

$$\sigma_{ij}^{l^{n+1}} = \underline{\sigma}_{ij}^{l^{n+1}} + \Delta\sigma_{ij}^{l^{n+\frac{1}{2}}} \tag{4.10}$$

The term $\Delta\sigma_{ij}^{J^{n+\frac{1}{2}}}$ is calculated from the constitutive Eq. (4.11).

$$\Delta\sigma_{ij}^{J^{n+\frac{1}{2}}} = C_{ijkl}\Delta\epsilon_{kl}^{J^{n+\frac{1}{2}}} \tag{4.11}$$

The tensor $C_{ijkl}$, is a material response tensor. Finally the updated stress tensor is rotated back to the global coordinate system using Eq. (4.12).

$$\sigma_{ij}^{n+1} = q_{ki}\sigma_{kn}^{J^{n+1}}q_{nj} \tag{4.12}$$

The material tensor $C_{ijkl}$ is stress dependent in elasto-plastic materials, due to the non-linear stress strain relationship. It also depends on the deformation gradient and the material parameters. Further information for the assessment of the material tensor can be found in [28] and [47]. Moreover, the transformation tensor **q** is not discussed in detail and the reader is referred to [24] and [29] for more information about its calculation.

After the evaluation of the updated stress tensor and its transformation to the global coordinate system, it is possible to calculate the internal forces for each node using Eq. (4.13).

$$f_{\alpha}^{int} = \int T_{\alpha}^{T}B_{\alpha}^{T}\sigma dv \tag{4.13}$$

Where $f_{\alpha}^{int}$ are the internal forces at node $\alpha$, $B_{\alpha}$ is the strain-displacement matrix in the local coordinate system associated with the displacements at node $\alpha$, and $T_{\alpha}$ is the transformation matrix relating the global and local components of the **B** matrix. The superscript T denotes transposed. The **B** matrix depends on the element shape functions; more information about it can be found in [29], [11] and [24].

## 4.2 SOLUTION METHODS

The numerical treatment of non-linear dynamical problems, requires the solution of the discretized equation of motion, shown in Eq. (4.14).

$$\mathbf{M\ddot{u}}(t) + \mathbf{C\dot{u}}(t) + \mathbf{Ku}(t) = \mathbf{f}(t) \tag{4.14}$$

Where $\ddot{\mathbf{u}}$, $\dot{\mathbf{u}}$ and **u** are the vectors of nodal accelerations, velocities and displacements respectively. **M**, **C** and **K** are the mass, damping and stiffness matrices respectively and **f** is the vector of nodal forces. The problem of solving the non-linear differential equations, is treated using *time integration methods*, where the corresponding algebraic equations are being solved within small time steps [46]. This technique is applied in an (over time) iterative scheme, updating the nodal kinematic quantities and the material parameters in each step, and gradually approximating the solution of the non-linear equations.

Time integration methods, are classified in too categories, *explicit* and *implicit methods*. In explicit methods, the state of the system in a later time, is calculated using information provided in the current time only. In implicit methods on the other hand, the state of the system in a later time is determined by solving an equation involving both the current state of the system and the later one.

If $Y(t)$ is the current system state and $Y(t+\Delta t)$ is the state at a later time $t+\Delta t$ system where $0 \leq t \leq t_{END}$ and $\Delta t$ is a small time step, for an explicit method,

$$Y(t+\Delta t) = F(Y(t)) \tag{4.15}$$

while in an implicit method, $Y(t+\Delta t)$ is calculated solving Eq. (4.16).

$$G(Y(t), Y(t+\Delta t)) = 0 \tag{4.16}$$

As a result, an implicit method requires an extra computation for the solution of Eq. (4.16) and can be more complicated to implement. In the case of non-linear structural analysis, this extra computation includes the inversion of the mass matrix, a process that may require high computational effort, see [35].

The use of implicit solution methods, arises from the fact that explicit methods are *conditionally stable* [46],[27]. This means that the method is stable, i.e. the error in the result is bounded, if the time step $\Delta t$ is less than a critical value (see section 4.3). In practice, this critical value can often be impractically small, in which case, an implicit method becomes more efficient.

It is thus dependent on the nature of the problem whether an explicit or an implicit method is more appropriate. In car crash simulation problems, where the modelling and analysis of the contact between different bodies requires small time steps anyway, explicit methods are more appropriate. The most common explicit solution method is the *Central Difference Method* (see section 4.2.1) a modification of which is implemented in LS-DYNA as the explicit time integration method (see section 4.2.2).

### 4.2.1 Central Difference Method

According to [11], the Central Different Method is among the most popular of the explicit methods in computational mechanics. It was developed from central difference formulas for the velocity and acceleration. Geometric and material non-linearities are included, and in fact have little effect on the time integration algorithm. It should be noted, that in the present thesis, only its application on Lagrangian meshes with rate-independent materials is considered [1].

Due to the fact that the Central Difference Method is a time integration method, time should be discretized. Let the time of the simulation $0 \leq t \leq t_E$ be subdivided into time intervals, or time steps $\Delta t^n$, $n = 1...n_{TS}$ where $n_{TS}$ is the number of time steps and $t_E$ is the end-time of the simulation. Time increment $n$ is given by

$$\Delta t^n = t^n - t^{n-1} \tag{4.17}$$

and the midpoint step by

$$\Delta t^{n+\frac{1}{2}} = \frac{1}{2}\left(\Delta t^n + \Delta t^{n+1}\right) \tag{4.18}$$

Assume that in the equation of motion, $\mathbf{u}$, $\dot{\mathbf{u}}$ and $\ddot{\mathbf{u}}$ are the displacement, velocity and acceleration respectively, then the central difference recursive formula for the velocity $\dot{\mathbf{u}}^{n+\frac{1}{2}} \equiv \dot{\mathbf{u}}(t^{n+\frac{1}{2}})$ is

$$\dot{\mathbf{u}}^{n+\frac{1}{2}} \equiv \mathbf{v}^{n+\frac{1}{2}} = \frac{1}{\Delta t^{n+\frac{1}{2}}}\left(\mathbf{u}^{n+1} - \mathbf{u}^n\right) \Rightarrow \mathbf{u}^{n+1} = \mathbf{u}^n + \Delta t^{n+\frac{1}{2}}\mathbf{v}^{n+\frac{1}{2}} \tag{4.19}$$

where the second equation gives the corresponding integration equation. The acceleration is given by

$$\ddot{\mathbf{u}}^n \equiv \mathbf{a}^n = \frac{1}{\Delta t^n}\left(\mathbf{v}^{n+\frac{1}{2}} - \mathbf{v}^{n-\frac{1}{2}}\right) \Rightarrow \mathbf{v}^{n+\frac{1}{2}} = \mathbf{v}^{n-\frac{1}{2}} + \Delta t^n \mathbf{a}^n \tag{4.20}$$

It can be observed, that the velocities are defined in midpoints of the time intervals, or at half time-steps. By substituting Eq. (4.19) and its counterpart for the previous time step into Eq. (4.20), the acceleration can be expressed directly in terms of the displacements

$$\ddot{\mathbf{u}}^n \equiv \mathbf{a}^n = \frac{\Delta t^{n-\frac{1}{2}}\left(\mathbf{u}^{n+1} - \mathbf{u}^n\right) - \Delta t^{n+\frac{1}{2}}\left(\mathbf{u}^n - \mathbf{u}^{n-1}\right)}{\Delta t^n \Delta t^{n-\frac{1}{2}} \Delta t^{n+\frac{1}{2}}} \tag{4.21}$$

[1] The term rate-dependent material, refers to materials where the deformation depends on the rate at which loads are applied

and for the case of equal time steps, Eq. (4.21) reduces to

$$\ddot{\mathbf{u}}^n \equiv \mathbf{a}^n = \frac{\left(\mathbf{u}^{n+1} - 2\mathbf{u}^n + \mathbf{u}^{n-1}\right)}{\left(\Delta t^n\right)^2} \tag{4.22}$$

which is the well known central difference formula for the second derivative of a function.

The time integration of the undamped equation of motion for rate-independent materials, which at time $n$ are given by

$$\mathbf{M}\mathbf{a}^n = \mathbf{f}^n = \mathbf{f}^{ext}\left(\mathbf{u}^n, t^n\right) - \mathbf{f}^{int}\left(\mathbf{u}^n, t^n\right) \tag{4.23}$$

subjected to

$$g_l\left(\mathbf{u}^n\right) = 0, \quad l = 1...n_c \tag{4.24}$$

where Eq. (4.24) is a generalized representation of the $n_c$ displacement boundary conditions. The mass matrix in Eq. (4.23) is considered constant because it is time independent for a Lagrangian mesh [11]. The internal and external nodal forces are functions of the nodal displacements and the time.

The nodal velocities can be updated using Eq. (4.25) which is derived from the combination of Eq. (4.22) and Eq. (4.23).

$$\mathbf{v}^{n+\frac{1}{2}} = \Delta t^n \mathbf{M}^{-1}\mathbf{f}^n + \mathbf{v}^{n-\frac{1}{2}} \tag{4.25}$$

The nodal displacements can then be updated using Eq. (4.19).

At any time step $n$, the displacements $\mathbf{u}^n$ will be known. The nodal forces $\mathbf{f}^n$ can be determined using in sequence the strain-displacement equations, the constitutive equation and the relation for the nodal internal forces. Thus the entire right hand side of Eq. (4.25) can be computed, which yields the evaluation of $\mathbf{v}^{n+\frac{1}{2}}$, and the displacements $\mathbf{u}^{n+1}$ at time step $n+1$ can be determined by Eq. (4.19). It can be observed, that the entire update can be accomplished without solving any system of equations provided that the mass matrix $\mathbf{M}$ is diagonal.

### 4.2.2 Time integration in LS-DYNA

The time integration scheme that is implemented in LS-DYNA, is based on the Central Difference time integration Method. Moreover, due to the fact that in LS-DYNA the actual geometry $\mathbf{x}$ is used instead of the displacements $\mathbf{u}$. The difference formula for the velocities is

$$\dot{\mathbf{x}}^{n+\frac{1}{2}} = \frac{1}{\Delta t^{n+\frac{1}{2}}}\left(\mathbf{x}^{n+1} - \mathbf{x}^n\right) \tag{4.26}$$

and for the accelerations

$$\ddot{\mathbf{x}}^n = \frac{1}{\Delta t^n}\left(\dot{\mathbf{x}}^{n+\frac{1}{2}} - \dot{\mathbf{x}}^{n-\frac{1}{2}}\right). \tag{4.27}$$

The damped equation of motion at time $t^n$ for the non-linear case is

$$\mathbf{M}\ddot{\mathbf{x}}^n = \mathbf{f}^{ext}\left(\mathbf{x}^n, t^n\right) - \mathbf{f}^{int}\left(\mathbf{x}^n, t^n\right) - \mathbf{C}\dot{\mathbf{x}}^n \tag{4.28}$$

where $\mathbf{M}$ and $\mathbf{C}$ are the mass and damping matrix respectively. The term $\dot{\mathbf{x}}^n$ is the unknown velocity at the current time $t^n$, and for that reason the assumption of asynchronous damping, $\mathbf{C}\dot{\mathbf{x}}^{n-\frac{1}{2}} \approx \mathbf{C}\dot{\mathbf{x}}^n$. This yields the formula for the update of the accelerations

$$\ddot{\mathbf{x}}^n = \mathbf{M}^{-1}\left(\mathbf{f}^{ext}\left(\mathbf{x}^n, t^n\right) - \mathbf{f}^{int}\left(\mathbf{x}^n, t^n\right) - \mathbf{C}\dot{\mathbf{x}}^{n-\frac{1}{2}}\right) \tag{4.29}$$

and subsequently for the velocities and the nodal coordinates

$$\dot{\mathbf{x}}^{n+\frac{1}{2}} = \dot{\mathbf{x}}^{n-\frac{1}{2}} + \Delta t^n \ddot{\mathbf{x}}^n \tag{4.30}$$

$$\mathbf{x}^{n+1} = \mathbf{x}^n + \Delta t^{n+\frac{1}{2}} \dot{\mathbf{x}}^{n+\frac{1}{2}}. \tag{4.31}$$

The time integration procedure implemented in LS-DYNA, can be schematically depicted in Fig. 4.1.

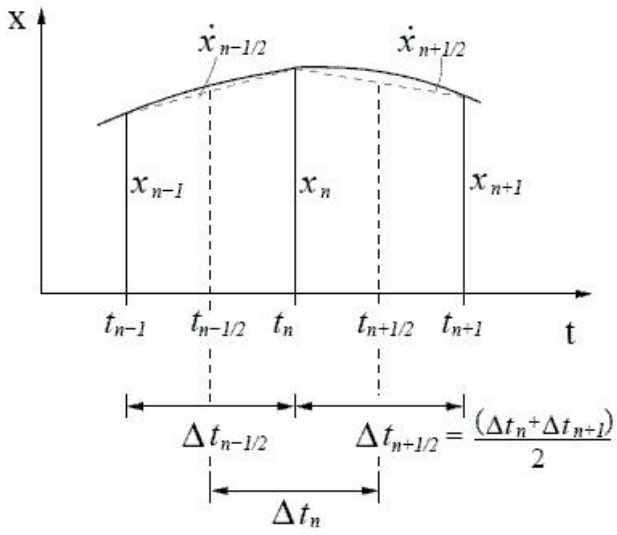


Figure 4.1: Time integration in LS-DYNA. [24]

For the implementation of the time integration scheme, the initial conditions should be specified. As a result, the actual geometric coordinates at time zero are

$$\mathbf{x}^0 = \bar{\mathbf{x}}^0 + \mathbf{u}_{stat} \tag{4.32}$$

where $\bar{\mathbf{x}}^0$ is the undeformed actual geometry, $\mathbf{u}_{stat}$ are the initial displacements from the static loading. The initial velocities are calculated by

$$\mathbf{v}^0 = \frac{1}{2}\left(\dot{\mathbf{x}}^{-\frac{1}{2}} - \dot{\mathbf{x}}^{\frac{1}{2}}\right) \tag{4.33}$$

and the initial acceleration can be calculated by

$$\ddot{\mathbf{x}}^0 = \mathbf{M}^{-1}\left(\mathbf{f}^{ext}\left(\mathbf{x}^0, t^0\right) + \mathbf{f}^{stat} - \mathbf{f}^{int}\left(\mathbf{u}_{stat}, t^0\right) - \mathbf{C}\mathbf{v}^0\right) \tag{4.34}$$

where $\mathbf{f}^{ext}\left(\mathbf{x}^0, t^0\right)$ is any possible external loading at time zero, $\mathbf{f}^{stat}$ is the static loading before the time integration starts and $\mathbf{f}^{int}\left(\mathbf{u}_{stat}, t^0\right)$ is the internal forces resulting from the static loading of the structure. Finally it is possible to calculate $\dot{\mathbf{x}}^{\frac{1}{2}}$ from Eq. (4.30) with Eq. (4.34).

$$\dot{\mathbf{x}}^{\frac{1}{2}} = \mathbf{v}^0 + \frac{1}{2}\Delta t^0 \ddot{\mathbf{x}}^0 \tag{4.35}$$

Note that $\mathbf{f}^{stat} - \mathbf{f}^{int}\left(\mathbf{u}_{stat}, t^0\right) = 0$ due to the assumption of static equilibrium before the beginning of the time integration process.

## 4.3 CRITICAL TIME STEP

Proofs about the stability of the Central Difference Method can be found in [11],[46],[27] and [24]. These proofs, conclude to the fact that the central difference time integration method is conditionally

stable. This is, the error in the calculation is bounded if and only if the time step is not larger than a critical time step value. This value is calculated from the stability proof and equals to

$$\Delta t_{crit} = \frac{2}{\omega_{max}} \left( \sqrt{1 + \xi^2} - \xi \right) \tag{4.36}$$

for the damped case where $\omega_{max}$ is the maximum eigenfrequency of the system and $\xi$ is the damping coefficient. For the undamped case it holds, $\xi = 0$.

The time step size is calculated for a rod of length $l$, cross-sectional area $A$, density $\rho$ and Young modulus $E$ with its mass lumped at the edges. Given that the wave propagation velocity in the rod is

$$c = \sqrt{\frac{E}{\rho}} \tag{4.37}$$

and after the calculations that can be found in [24], the critical time step for the rod is

$$\Delta t_{crit}^{rod} = \frac{l}{c}. \tag{4.38}$$

This is the time needed for the wave to propagate through the rod of length $l$ and is also referred to as the *Courant-Friedrichs-Lewy condition*.

The critical time step is being calculated for each element and the time step of the simulation is the minimum among all the time steps. The time step is possible to change in the simulation, due to alternations in the geometry, and for that reason a new time step size is being calculated in every time loop using Eq. (4.39).

$$\Delta t^{n+1} = \alpha \cdot \min\{\Delta t_1, \Delta t_2, \Delta t_3, ..., \Delta t_N\} \tag{4.39}$$

Where $N$ is the total number of elements and $\alpha$ is a scale factor used for stability reasons which by default equals to $0.90$.

In LS-DYNA, there are solutions for the critical time step for different material types. Here only the case of elastic material with constant bulk modulus is shown. As a result, the critical time step for a beam element is identical to the one calculated for the rod in Eq. (4.38). The critical time step for a shell and a solid element is evaluated by comparing the wave propagation velocity to the case of a rod. For shell elements it holds

$$c_{2D-continuum} = \sqrt{\frac{E}{(1 - \nu^2)\rho}} \tag{4.40}$$

where $\nu$ is the Poisson ratio and thus, we can calculate the critical time step using the relationship

$$\frac{\Delta t_{2D-continuum}}{\Delta t_{rod}} = \frac{c_{rod}}{c_{2D-continuum}} = \sqrt{(1 - \nu^2)}. \tag{4.41}$$

For solid elements it holds

$$c_{3D-continuum} = \sqrt{\frac{E(1 - \nu)}{(1 + \nu)(1 - 2\nu)\rho}} \tag{4.42}$$

and thus, we can calculate the critical time step using the relationship

$$\frac{\Delta t_{3D-continuum}}{\Delta t_{rod}} = \frac{c_{rod}}{c_{3D-continuum}} = \sqrt{\frac{1 - \nu}{(1 + \nu)(1 - 2\nu)}} \tag{4.43}$$

### 4.3.1 Time-step control

Due to the Courant-Friedrichs-Lewy condition for the critical time step, the calculated time-step size is often very small, and makes the analysis inefficient. For that reason, a procedure is followed that adds small amounts af lumped mass at the nodes of the stiffer elements that caused this small time-step. This procedure is called *dynamic mass scaling* and can increase the time step sufficiently, making the analysis feasible. The extra mass added for this purpose, should not be too much so that the calculation is affected, and for that reason it is required to be checked after the end of the analysis. This time-step control, is applied using the parameter dt2ms in the keyword *CONTROL_ TIMESTEP shown in Appendix C.1.

Another procedure that can be used to increase the time step size, is called *sub-cycling*. In that procedure, a smaller time step is used for the stiffer elements, and thus the rest of the elements can be treated using larger time steps. Sub-cycling has not been employed in the present thesis.

## 4.4 IMPLEMENTATION

In the present section, a structogram of the algorithm for the explicit time integration of dynamical problems is presented, and followed by a short discussion. The structogram is based on the standard Central Difference Method, with the assumption of un-damped equation of motion.

**Explicit time integration**

1. Initialize:
   a. Set $t = 0$ and $n = 0$
   b. Set the initial velocities $\mathbf{v}^0$ and displacements $\mathbf{u}^0 = \mathbf{0}$ at the nodes
   c. Set the initial stresses $\boldsymbol{\sigma}^0$ at the element integration points
   d. Compute the lumped mass $\mathbf{M}$ at the nodes
2. Call subroutine **get_forces**
3. Do while $t^n \leq t_{END}$
   a. Compute accelerations $\mathbf{a}^n = \mathbf{M}^{-1}\mathbf{f}^n$
   b. Update time: $\Delta t^{n+\frac{1}{2}} = \Delta t, \quad t^{n+1} = t^n + \Delta t^{n+\frac{1}{2}}, \quad t^{n+\frac{1}{2}} = \frac{1}{2}(t^n + t^{n+1})$
   c. For each node I:
      i. Update of the velocity: $\mathbf{v}_I^{n+\frac{1}{2}} = \mathbf{v}_I^{n-\frac{1}{2}} + \Delta t \cdot \mathbf{a}_I^n$
      ii. Apply velocity boundary conditions: if node I on $\Gamma_{\mathbf{v}}$, then $\mathbf{v}_I^{n+\frac{1}{2}} = \bar{\mathbf{v}}(I, t^{n+\frac{1}{2}})$
      iii. Update displacements: $\mathbf{u}_I^{n+1} = \mathbf{u}_I^n + \Delta t \cdot \mathbf{v}_I^{n+\frac{1}{2}}$
   d. Call subroutine **get_forces**
   e. Update the counter: $n = n + 1$

**1.b.** Initial values for the nodal velocities should be provided. The initial displacements are assumed to vanish because they are meaningless in non-linear analysis (except for hyper-elastic materials since the stress generally depends on the history of deformation).

**1.c.** Initial values of the Cauchy stresses should be provided.

**1.d.** The computation of the mass matrix $\mathbf{M}$, depends on the used element type, see [29] and [24].

**2.** The subroutine **get_forces** is called to calculate the external forces, the internal forces based on the initial stresses and the total forces. This first call of **get_forces**, does not include any strain or stress computation, and the constitutive equations do not apply.

**3.** Main loop, the explicit time integration equations are applied in each time step.

**3.a.** Computation of the accelerations using the nodal forces $\mathbf{f}^n$, output of the subroutine **get_forces**, according to Eq. (4.23). This equation usually contains a damping factor. Here it has not been considered for simplicity. Moreover, this equation, takes an explicit form (no need for solving system of equations) if the mass matrix **M** is diagonal.

**3.b.** The current time-step $\Delta t$, is output of the subroutine **get_forces**, because the loop over the elements is performed within this subroutine.

**3.c.** Loop over the nodes for the application of the explicit equations

**3.c.i.** The update of the velocities is performed according to Eq. (4.20).

**3.c.ii.** The boundary conditions can be given in terms of prescribed displacements or velocities as function of time. If node I lies on the boundary $\Gamma_{\mathbf{v}}$, then set the velocity (or displacement) according to the given time dependent function $\bar{\mathbf{v}}(I, t^{n+\frac{1}{2}})$.

**3.c.iii.** The update of the displacements is performed according to Eq. (4.19).

**3.d.** The subroutine **get_forces**, is called in the main loop to calculate the external, internal and total forces after applying the constitutive equations for the determination of the element stresses. Note that the critical time step size $\Delta t_{crit}$ is calculated in each time step. The subroutine **get_forces**, is described in the following.

<table>
<tr><td colspan="2">Subroutine get_forces</td></tr>
<tr><td colspan="2">1. Set $\mathbf{f}^n = 0$ and $\Delta t_{crit} = 0$</td></tr>
<tr><td colspan="2">2. Compute global external nodal forces $\mathbf{f}^n_{ext}$</td></tr>
<tr><td colspan="2">3. For each element (at the integration points):</td></tr>
<tr><td>$n = 0$</td><td>$n \neq 0$</td></tr>
<tr><td>SKIP</td><td>a. Compute measures of deformation: $\Delta\boldsymbol{\epsilon}$ and $\Delta\boldsymbol{\omega}$<br>b. Compute stress $\boldsymbol{\sigma}^n$ by constitutive equation</td></tr>
<tr><td colspan="2">c. Compute the element internal forces: $\mathbf{f}_e^{int,n}$<br>d. Compute the element external forces $\mathbf{f}_e^{ext,n}$ by the global external forces<br>e. Compute the element total forces: $\mathbf{f}_e^n = \mathbf{f}_e^{ext,n} - \mathbf{f}_e^{int,n}$<br>f. Scatter the element forces $\mathbf{f}_e^n$ to the global forces $\mathbf{f}^n$<br>g. Compute the element critical time step $\Delta t^e_{crit}$, if $\Delta t^e_{crit} < \Delta t_{crit}$ then $\Delta t_{crit} = \Delta t^e_{crit}$</td></tr>
<tr><td colspan="2">4. Set $\Delta t = \alpha \Delta t_{crit}$</td></tr>
<tr><td colspan="2">5. Return $\mathbf{f}^n$, $\Delta t$</td></tr>
</table>

**1.** The global array of nodal forces $\mathbf{f}^n$ is set to zero as well as the critical time step size $\Delta t_{crit}$, because it is calculated in each time step.

**3.** Loop over the elements for the application of the constitutive equations and the calculation of the nodal forces.

**3.a.** The incremental strain and rotation tensors $\Delta\boldsymbol{\epsilon}$ and $\Delta\boldsymbol{\omega}$ respectively, are calculated according to Eq. (4.4)-(4.6).

**3.b.** The stresses are being updated with consideration of possible rotations and material response as well, according to Eq. (4.7)-(4.11).

**3.c.** The internal nodal forces are computed in the local coordinate system, according to Eq. (4.13).

**3.d.** The external nodal forces are computed in the local coordinate system, using the computed global external nodal forces.

**3.f.** The element total nodal forces, are assigned in the global array of nodal forces.

**3.g.** The critical time step size is computed in each step according to section 4.3.

**4.** The critical time step is scaled with the factor $\alpha = 0.90$ for numerical stability reasons.

**5.** Finally, the global nodal forces as well as the time step size of the next step are returned into the main program.

It should be noted, that the structogram in the present section, provides a general overview of an explicit time integration algorithm and does not describe all the important aspects for the implementation od the process. Aspects like the mass matrix calculation, the exact application of the boundary conditions, the **B** matrix assessment for the calculation of the internal forces in Eq. (4.13), the calculation of the incremental displacement gradient **G** involved in the computation of the deformation measures $\Delta\boldsymbol{\epsilon}$ and $\Delta\boldsymbol{\omega}$ in Eq. (4.5) and (4.6), are not treated analytically.

## 4.5 CONTACT/IMPACT ALGORITHM

Many problems in the simulation of prototype tests and manufacturing processes involve contact and impact. The computational treatment of such problems, requires the employment of a separate contact/impact model which applies two basic operations in a through time step-wise manner. In each time step, the first operation identifies the contact and the second enforces the contacting bodies to behave (deform, translate, rotate etc.) according to the geometric and kinematic conditions of the problem at the current time.

According to [11], there are four methods to treat the contact surface conditions. The *Lagrange multiplier method*, the *penalty method*, the *augmented Lagrangian method* and the *perturbed Lagrangian method*. The most common method used in LS-DYNA, is the penalty method, and according to [24], it the most efficient especially in common contact problems. In LS-DYNA, a further distinction among different alternatives of the penalty method has been implemented to improve the efficiency of special application's contact modelling. Among these alternatives, the *Standard Penalty Formulation* is the most convenient and the most efficient. It is the only method used in LS-DYNA ordinary contact problems that involve bodies with similar material properties, and will be the only one explained in the present thesis.

### 4.5.1 Contact identification

Consider a time dependent problem involving the motion of two bodies occupying regions $B^1$ and $B^2$. If $\partial B^1$ and $\partial B^2$ are the boundaries of $B^1$ and $B^2$ respectively, in the undeformed configuration at time zero, it holds

$$\partial B^1 \cap \partial B^2 = 0. \tag{4.44}$$

Contact has assumed the situation that in some later time, it holds, for the now deformed bodies $b^1$ and $b^2$

$$\partial b^1 \cap \partial b^2 \neq 0. \tag{4.45}$$

As a result, the condition in Eq. (4.45) should be checked in each time step.

Some additional statements should be made concerning the terminology. The surfaces $\partial b^1$ and $\partial b^2$ of the discretized bodies $b^1$ and $b^2$ become the master and the slave surfaces respectively. The choice of the master and the slave surface will be discussed in the later.

In each time step, the so-called *slave search* is performed. Slave search finds for each slave node, the nearest point on the master surface. Lines drawn from a slave node to its nearest point will be perpendicular to the master surface, unless the point lies on the intersection of two *master segments*. A segment can be defined as a 3 or 4 node element of the master surface.

Let $\mathbf{t}$ be the position vector of a slave node $n_s$ and that the nearest point has been identified to lie on the master surface segment $s_m$ defined by the nodes $1, 2, 3, 4$ see Fig. 4.2.

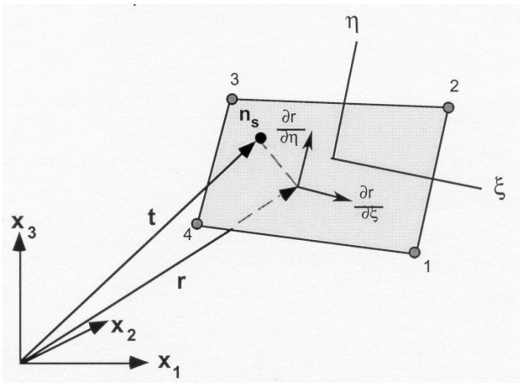


Figure 4.2: Location of contact point when $n_s$ lies above master segment. [24]

In Fig. 4.2, $\xi, \eta$ denotes the parametric coordinate system of segment $s_m$ and the position vector $\mathbf{r}(\xi_c, \eta_c)$, defines the nearest point which has the coordinates $\xi_c, \eta_c$.

Penetration of the slave node $n_s$ through the master segment $s_m$ which contains its nearest point, is indicated if

$$l = \mathbf{n}_m \times [\mathbf{t} - \mathbf{r}(\xi_c, \eta_c)] < 0 \tag{4.46}$$

where

$$\mathbf{n}_m = \mathbf{n}_m(\xi_c, \eta_c) \tag{4.47}$$

is the normal to the master segment at the contact point.

### 4.5.2 Contact stiffness calculation

In the Standard Penalty Formulation contact method, if the slave node does not penetrate nothing is done. If it does penetrate, an interface force is applied between the slave node and it's contact point. The magnitude of this force is proportional to the amount of penetration. This is may thought of as the addition of an interface spring.

If the slave node $n_s$ has penetrated in the master segment $s_m$, an interface force vector $\mathbf{f}_s$ is added

$$\mathbf{f}_s = -lk_i \cdot \mathbf{n}_m \qquad if \quad l < 0 \tag{4.48}$$

to the degrees of freedom corresponding to $n_s$ and

$$\mathbf{f}_m^i = \varphi_i(\xi_c, \eta_c) \cdot \mathbf{f}_s \qquad if \quad l < 0 \tag{4.49}$$

to the four nodes ($i = 1, 2, 3, 4$) that comprise the master segment $s_m$; $\varphi_i(\xi, \eta)$ is the shape function of the $i^{th}$ node. The stiffness factor $k_m$ for the master segment $s_m$ is given in terms of the bulk modulus $K_m$, the volume $V_m$ and the face area $A_m$ of the element that contains $s_m$ as

$$k_m = \frac{f_{si} K_m A_m^2}{V_m} \tag{4.50}$$

for solid (brick) elements, and

$$k_m = \frac{f_{si} K_m A_m}{\max(\textit{shell diagonal})} \tag{4.51}$$

for shell elements. Where $f_{si}$ is a scale factor for the interface stiffness and is normally defaulted to 0.10. According to [24], larger values may cause instabilities unless the step size is scaled.

### 4.5.3 Contact types

The contact types implemented in LS-DYNA, can be classified in many different ways. Some of the most important will be discussed in the present subsection.

Contact types can be classified according to their capability of transmitting tensile forces. The ordinary contact which does not transmit tensile forces is more appropriate for modelling impact and was used throughout the present thesis. This type of contact allows the compression loads to be transferred between the slave nodes to the master segments. Tangential loads are also transmitted if relative sliding occurs when contact friction is active. Friction is calculated based on a Coulomb formulation and using the friction coefficients (static and dynamic) and other parameters. Contact damping is accounted for, using a damping value as a percentage of the critical damping $2m\omega$.

On the other hand, contacts that are capable of transmitting tensile forces as well, are denoted as *tied contacts*. Their use is rare because in many practical problems the choice of single constraints between the master and the slave nodes is much more efficient. Despite that fact, in some cases, e.g. complex geometry, tied contacts can be helpful, because the may be more convenient to define than the single constraints.

Another classification of the contacts, concerns the symmetry in the calculation and distinguishes between *one-way* and *two-way* contacts. In the one-way contacts, only the user-specified slave nodes are checked for penetration into the master segments. In the two-way contacts, the sub-routines which check the slave nodes for penetration, are called a second time to check the master nodes for penetration into the slave segments. As a result, the definition of the master and slave surface is arbitrary since the results will be the same. Despite the additional cost of the two-way contact type, it was the only one used in the present thesis. The fact that the contacting bodies have similar material properties and mesh density, made this type of symmetric treatment more suitable.

An important aspect in practical problems, is the definition of the contact surfaces. In LS-DYNA, the definition can be done using sets of nodes, elements, segments or parts. Proper definition of the contact surface may result in improved computational stability. Concerning the contact surface definition option, a classification can be made between *single-surface* and *surface-to-surface* contacts. In the present thesis, the surface-to-surface type was used for the contact between the car and the structure. In this type, the master and slave surfaces are defined separately, even if it is irrelevant which is which because the two-way treatment is applied.

In the single-surface type, the user defines only one surface usually through sets of parts and LS-DYNA searches for self contact of the defined surface. As a result, all possible contacts between

parts including in the set are covered, as well as self contact of the parts to themselves. For that reason, one single-surface contact that included the whole structure was defined. Another single-surface contact containing all the parts of the car existed in the given car model. According to [37], if the model is accurately defined, these contact types are very reliable and accurate. However if there is a lot of interpretations in the initial configuration, energy balances may show either a growth or a decay of energy as the calculation proceeds.

Table 4.1 summarizes all the contacts used in the impact simulation model. Details about the different keywords used for the definition of the various types of contacts, can be found in Appendix C.1.

Table 4.1: Summary table of the contacts defined in the present studies

| Contact | type | friction | keyword |
|---|---|---|---|
| Structure - Structure | single surface | yes | *CONTACT_ AUTOMATIC_ SINGLE_ SURFACE |
| Car - Structure | surface to surface | yes | *CONTACT_ AUTOMATIC_ SURFACE_ TO_ SURFACE |
| Car - Road | surface to surface | no | *CONTACT_ AUTOMATIC_ SURFACE_ TO_ SURFACE |
| Structure - road | surface to surface | no | *CONTACT_ AUTOMATIC_ SURFACE_ TO_ SURFACE |
| Bolts - Road | tied | - | *CONTACT_ TIED_ NODES_ TO_SURFACE |
| Rings - Column a) | tied | - | *CONTACT_ TIED_ NODES_ TO_ SURFACE_ CONSTRAINED_ OFFSET |
| Rings - Column b) | tied | - | *CONTACT_ TIED_ NODES_ TO_ SURFACE_ CONSTRAINED_ OFFSET |

### 4.5.4 Contact energy calculation

Contact energy $E_{contact}$ is incrementally updated from time $n$ to time $n+1$ for each two-way contact interface as

$$E_{contact}^{n+1} = E_{contact}^{n} + \left[ \sum_{i=1}^{nsn} \Delta F_i^{slave} \times \Delta dist_i^{slave} + \sum_{i=1}^{nmn} \Delta F_i^{master} \times \Delta dist_i^{master} \right]^{n+\frac{1}{2}}.$$

Where,

$nsn$ = number of slave nodes
$nmn$ = number of master nodes
$\Delta F_i^{slave}$ = interface force between the $i^{th}$ slave node and the contact master segment
$\Delta F_i^{master}$ = interface force between the $i^{th}$ master node and the contact slave segment
$\Delta dist_i^{slave}$ = incremental distance the $i^{th}$ slave node has moved during the current time step
$\Delta dist_i^{master}$ = incremental distance the $i^{th}$ master node has moved during the current time step.

According to [24], in the absence of friction the master and the slave side energies should be close in magnitude but opposite in sign. Large negative contact energy is usually caused by undetected penetrations. In the presence of damping and friction followed by relative sliding, the contact energy can take substantial positive values.

Finally some improvements implemented in the LS-DYNA contact algorithm will be only mentioned. These are, improved contact search strategy in special applications like metal-forming, the accounting of the shell element thickness and the initial contact interpretations.

## 4.6 ANALYSIS PARAMETERS

The numerical analysis of the simulation problem was performed using LS-DYNA, as already mentioned. All the pre-processing steps (geometry definition, meshing, definition of solution parameters etc.), conclude to the construction of a text file, the LS-DYNA input file which has the extension ".k". All the information required by the solver are stored in the input file under specific commands, the so called *keywords*. Only some important parameters of the analysis are discussed in the present section. In addition, in Appendix C.1, the keywords associated with the impact simulation problem of the present thesis are being discussed in an alphabetical order.

The main keywords required by any LS-DYNA Finite Element model, are shown in Fig. 4.3 together with the inter-connections between them.

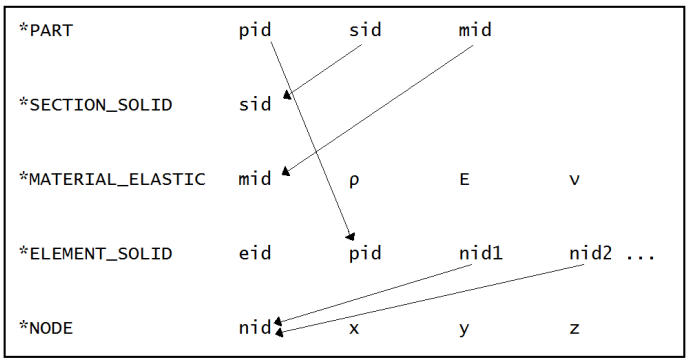


Figure 4.3: Basic keywords and their inter-connections, for an LS-DYNA input file.

### Units

The consistent set of units used in the numerical simulation with LS-DYNA, is summarized in Table 4.2.

Table 4.2: Units

| Mass | Length | Time | Force | Stress | Energy |
|---|---|---|---|---|---|
| $\mathrm{kg}$ | $\mathrm{mm}$ | $\mathrm{ms}$ | $\mathrm{kN}$ | $\mathrm{GPa}$ | $\mathrm{kN} \cdot \mathrm{mm} (= J)$ |

### Energy balance

A first verification of a Finite Element solution, is a plausible energy balance. As a result, it is necessary to compute the energy balance accurately and for that reason, all the possible energy loses should be taken into account. The keyword *CONTROL_ ENERGY, provides the options of including hourglass, sliding, damping and rigid wall energy, in the energy balance. After the end of the calculation, the energy balance should be checked, because it is likely to reveal possible coarse numerical errors.

### Accuracy

In order to achieve higher levels of accuracy, it is possible to include the $2^{nd}$ order terms in the stress update formulas. This option, has a significant effect in the case of large rotations (spins) like in the tyres of the car. This option can be enabled using the keyword *CONTROL_ ACCURACY, see Appendix C.1.

### Termination

The termination of the analysis is controlled by assigning a termination time, after the exhaustion of which, all the calculations stop. This termination time is defined in the keyword *CONTROL_ TERMINATION, see Appendix C.1.

# 5 RESULTS

The numerical test of the impact was performed for two cases, single truss structure without sign and double truss structure including sign. In the second case, the impact was more severe, and hence, this case was adopted for further investigations, where four different experiments for the four impact speed classes 35, 50, 70, 100 km/h were performed. The results of these experiments are presented in the present section. The impact against one single truss, is only depicted in Fig. C.1 and C.2 in Appendix C.2 for the different time steps.

## 5.1 TEST REPORT

Table 5.1: Test report according to [2]: section 6. Test procedure.

| **6. Test procedure** | |
|---|---|
| a) Target data | |
| - target impact speed in km/h: | 35, 50, 70, 100 |
| - target impact angle in degrees: | 20° |
| - target inertial vehicle test mass in kg: | $825 \pm 40$ |
| - predicted behaviour: | - |
| b) Test installation | |
| - detailed description of the installation tested: | sections 3.1 and 3.2 |
| - backfill properties: | rigid |
| - test cite drawings: | Fig. 3.20 |
| - photographs: | Fig. 3.20 |
| c) Test vehicle | |
| - model: | FE model |
| - model year: | - |
| - vehicle identification number, VIN: | - |
| - inertial test mass (including ballast) in kg: | 864.85 |
| - ballast, position and mass in kg: | yes, front seat, 30.74 |
| - dummy, position, type and mass, seat belt type: | yes, driver, Hybrid III $50^{th}$, 78.52 kg , - |
| - gross static mass in kg: | 943.37 |
| - dimensions of vehicle: | Table 3.5 |
| - position of centre of gravity: | Table 3.5 |
| - photographs: | Fig. 3.16, 3.18 and 3.19 |
| d) Calibration test vehicle | not required |

The results from the standard impact test according to [2] of the impact against the double truss structure, are shown by means of standard test report. Note that only sections 6. 'Test procedure' and 7. 'Results' of the standard test report are shown because they are the most important.

Table 5.2: Test report according to [2]: section 7. Results.

| **7. Results** | speed classes | | | |
|---|---|---|---|---|
| | 35 | 50 | 70 | 100 |
| a) General | | | | |
| - test No: | 1 | 2 | 3 | 4 |
| - date: | - | - | - | - |
| - weather conditions: | - | - | - | - |
| - impact angle in degrees: | 20° | 20° | 20° | 20° |
| - impact speed in km/h: | 35 | 50 | 70 | 100 |
| - exit speed in km/h: | 16.1 | 32.3 | 58 | 89.8 |
| - general description of test sequence, chapter: | (3) | (3) | (3) | (3) |
| - photographs, figures: | (5.2) | (5.3) | (5.4) | (5.5) |
| b) General Performance requirements | | | | |
| - did the test item behaved as predicted?: | yes | yes | yes | yes |
| - were there any risks according with [1]: | no | no | no | no |
| - did the vehicle behaved in accordance with [2]: | yes | yes | yes | yes |
| - Acceleration Severity Index, ASI: | 0.7 | 0.9 | 0.9 | 1.3 |
| - Theoretical Head Impact Velocity, THIV, in km/h : | 3.1 | 2.7 | 1.0 | 2.8 |
| - Was there any penetration of the occupant compartment?: | no | no | no | no |
| c) Additional requirements for particular items | | | | |
| - lowest point in accordance with [3]: | - | - | - | - |
| - Roof penetration?: | no | no | no | no |
| d) Additional restrictions regarding the installation: | - | | | |
| e) Acceleration graphs, figures | Fig. 5.6 | | | |

[1] section 2.3.5 Basic requirements, Road user or vehicle occupant risk, Detached elements and penetration.
[2] section 2.3.5 Basic requirements, Road user or vehicle occupant risk, Vehicle behaviour.
[3] section 2.3.5 Additional requirements for cantilever and gantry sign supports.

## 5.2 FIGURES

In the present section, Von-Misses stresses are being shown in contour plots for different time steps of the impact for the different speed classes (35, 50, 70 and 100 km/h). A value close to the yield stress of the steel ($\approx 0.250$ GPa) has been set at the threshold between orange and red colour in all the contour plots. The behaviour of the system is deemed to be predictable in Fig. 5.1-5.5. Moreover, the fact that the head of the dummy does not contact the airbag in none of the experiments shows that the impact is not very sever.

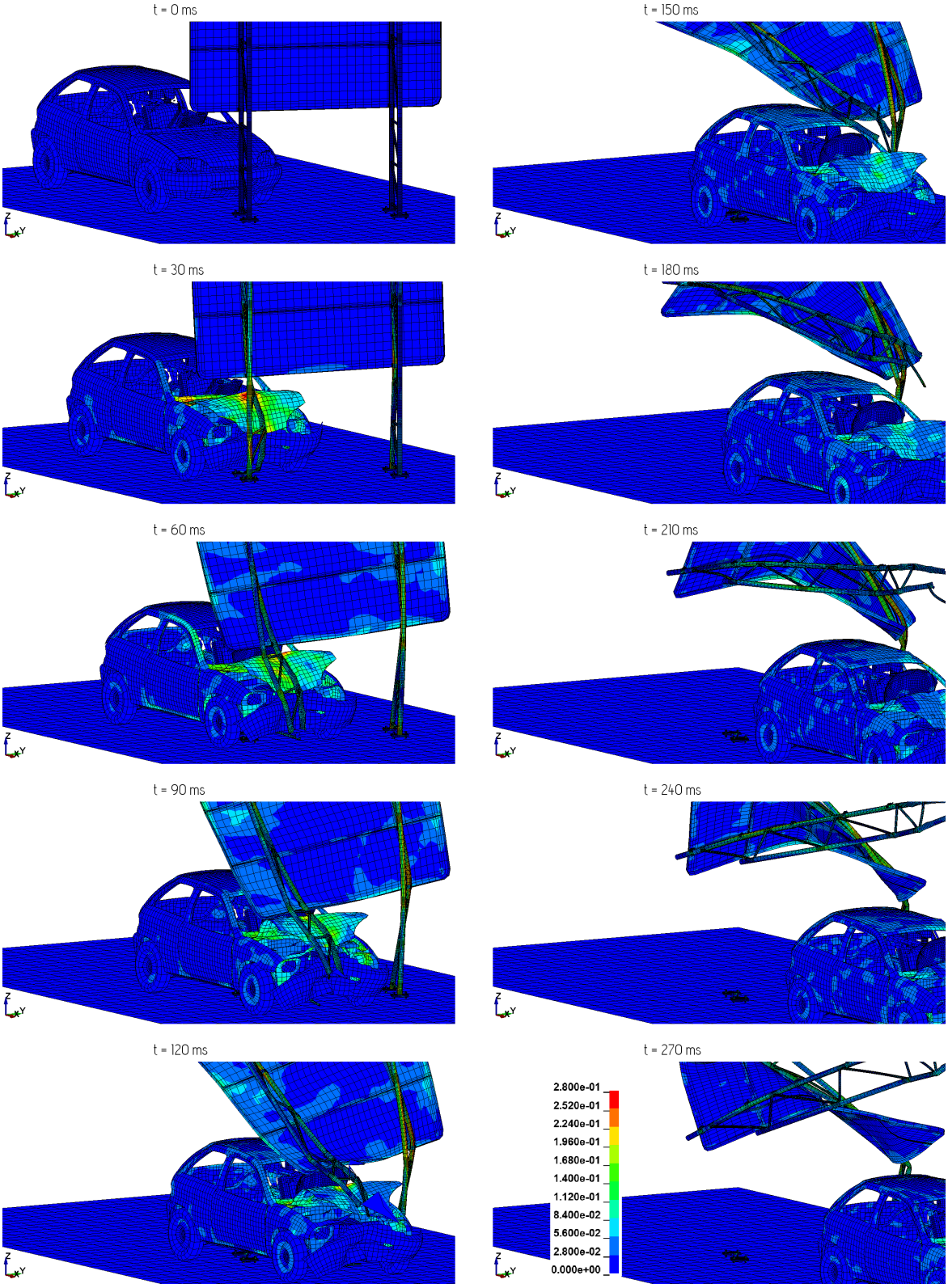


Figure 5.1: Von-Misses stress distribution in GPa for different time steps in perspective view for the 100 km/h speed class.

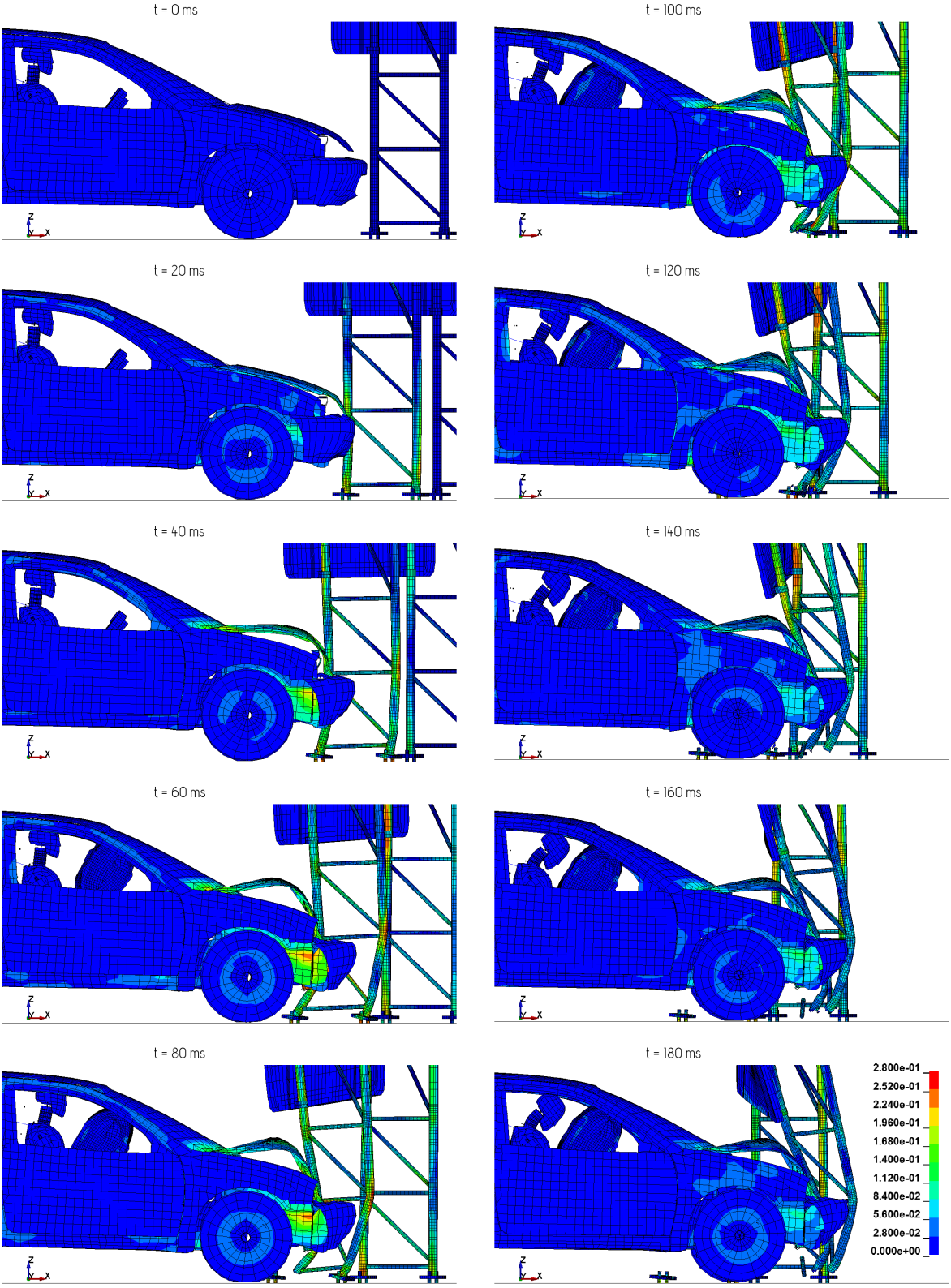


Figure 5.2: Von-Misses stress distribution in GPa for different time steps in side view for the 35 km/h speed class.

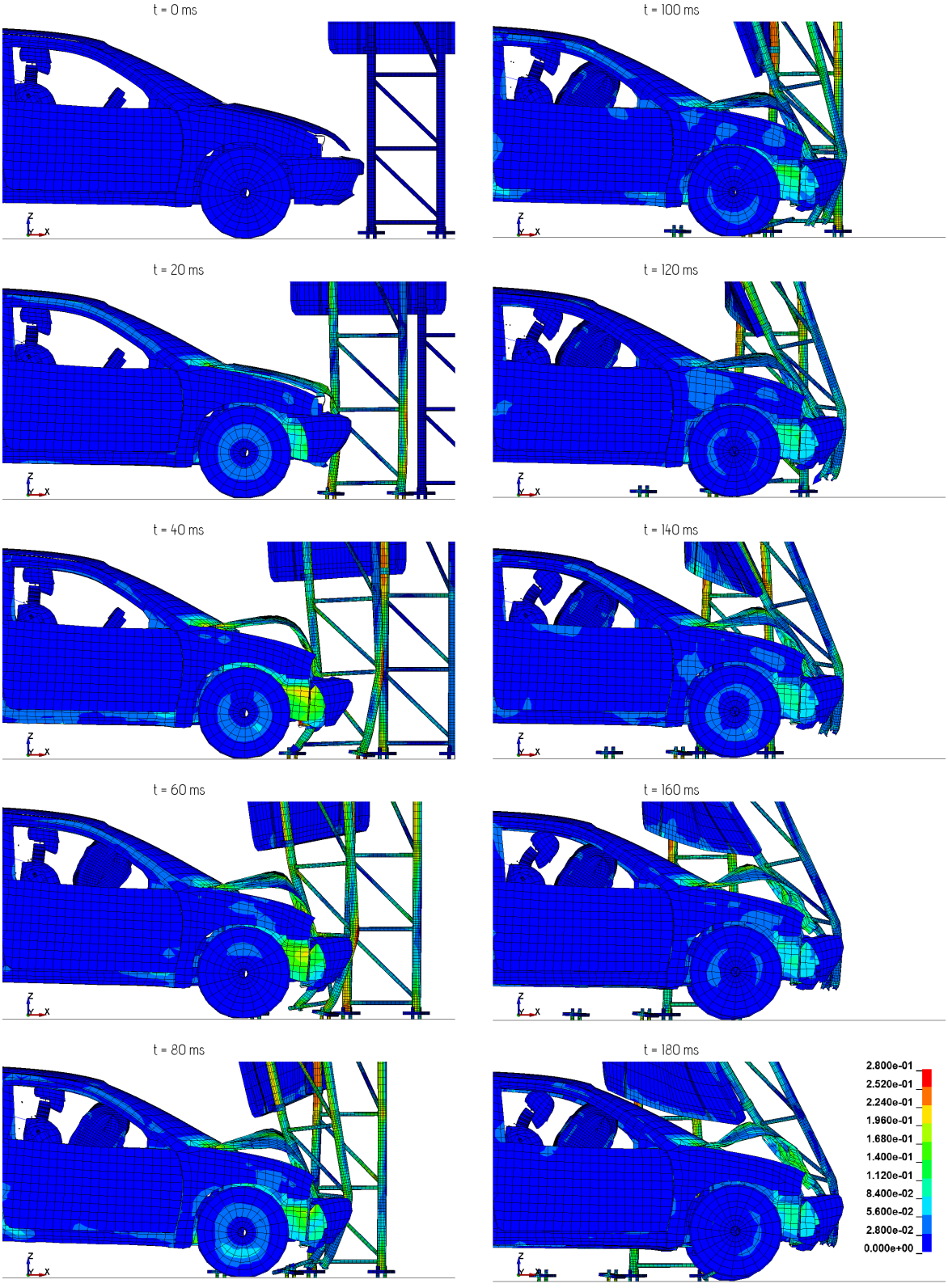


Figure 5.3: Von-Misses stress distribution in GPa for different time steps in side view for the 50 km/h speed class.

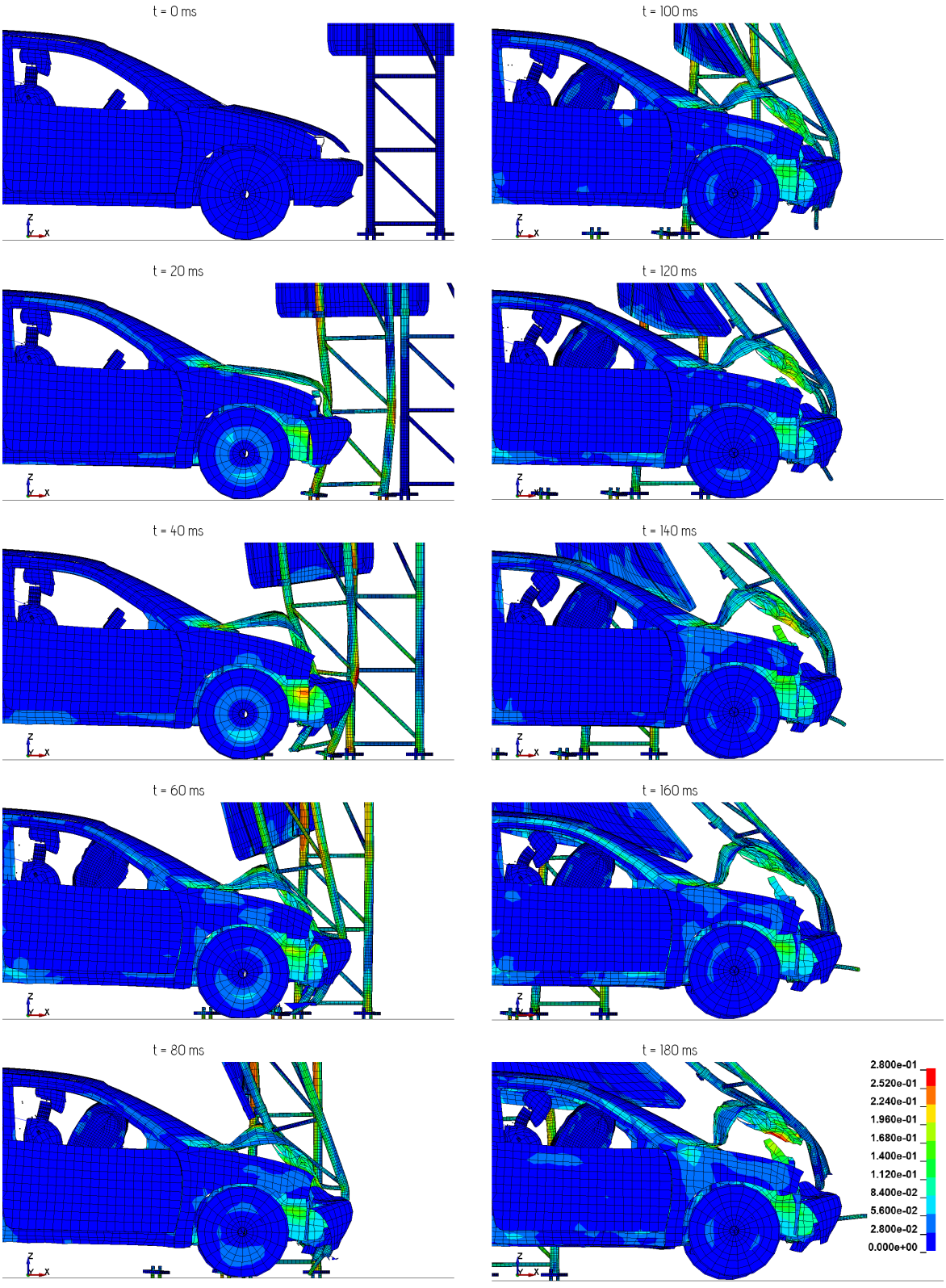


Figure 5.4: Von-Misses stress distribution in GPa for different time steps in side view for the 70 km/h speed class.

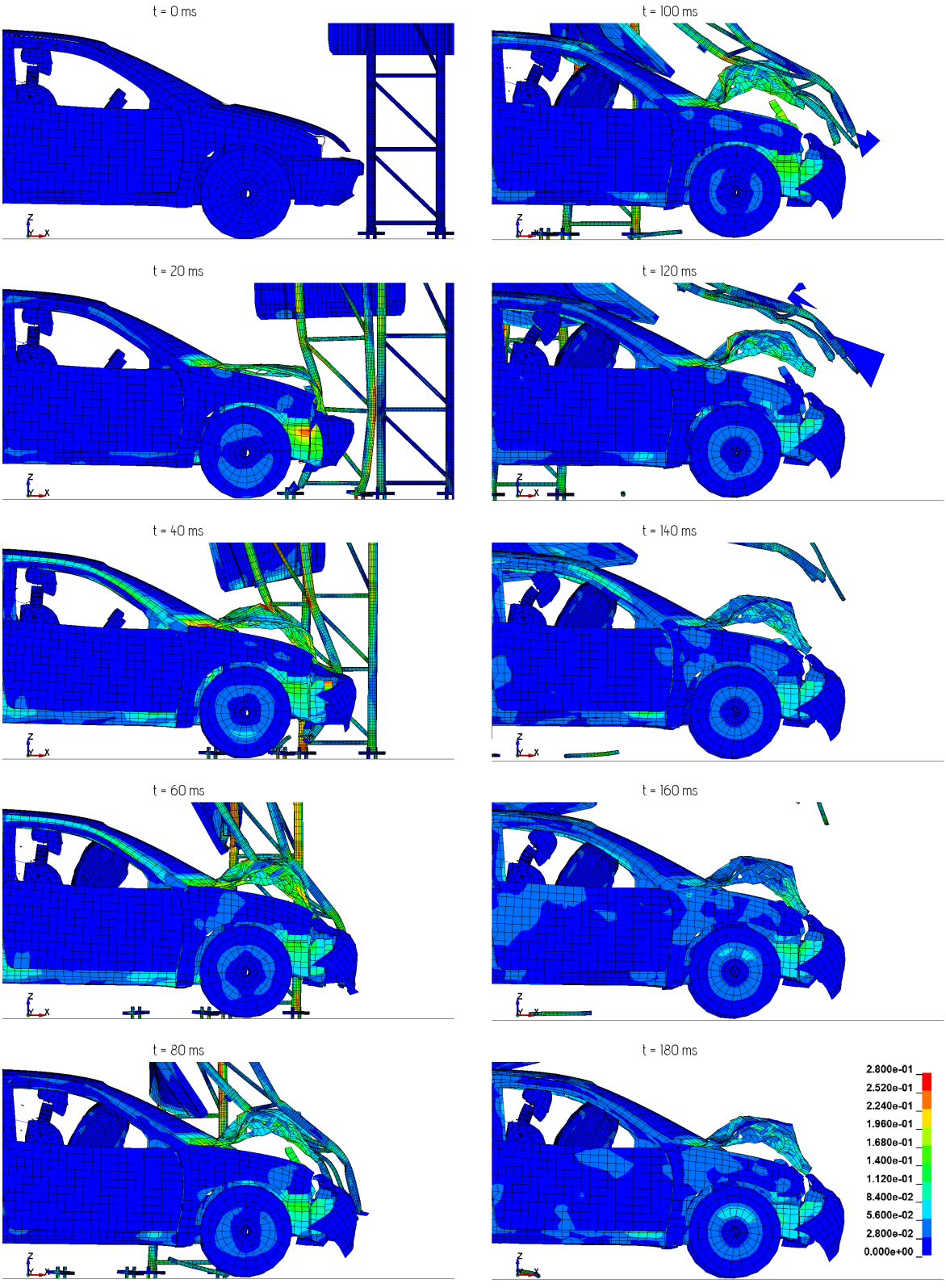


Figure 5.5: Von-Misses stress distribution in GPa for different time steps in side view for the 100 km/h speed class.

## 5.3 GRAPHS

In the present section, plots of acceleration and velocity time-histories of one node in the centre of mass of the dummy's head (node 8000001) and one in the centre of mass of the car (node 700002), are shown. As generally stated in [13],[16],[18],[34],[39] and [49], acceleration measurements during real or simulated crash tests, usually suffer from high amounts of numerical noise. As a result, these data need to be filtered using a low-pass digital filter.

**Filtering**

The acceleration time-histories of particular nodes in a crash simulation model usually contain unphysical, high frequency components. These high frequency accelerations result from vibrations within the body that contains the particular node as well as vibrations of all the other bodies rigidly connected to the referred one. The problem is that these high frequency accelerations interfere in the recordings of the real impact pulses, often making them undetectable. For the solution of that problem, present practice is to use a Butterworth digital low-pass filter applied forward and backward in time (4-pole filter) to avoid phase shifts in time (see Appendix A.2). The so called *cut-off frequency* of the filter is of major importance and engineering judgement should be used to extract the important physical information such as peak accelerations [18].

A common classification of digital filters distinguishes them according to the Channel Frequency Class (CFC) [31], [7]. According to [4], accelerations at the centre of mass of the car, should be filtered using a 4-pole Butterworth digital low-pass filter of class CFC_180 for the calculation of the severity indices ASI and THIV and a same filter of class CFC_60 for plotting acceleration time-history graphs (see Fig. 2.3). In addition to that, according to [16], crash acceleration data compare fairly well with experimental results when both filtered using a CFC_180 class filter. Moreover, in [1] and in [39], it is stated that before the calculation of the HIC, the Cartesian components of the acceleration time-histories of the head, should be filtered separately using a CFC_1000 digital filter. Then the HIC is calculated in the resultant of the filtered acceleration components [1]. The formulas for the application of a 4-pole Butterworth digital filter can be found in Appendix A.2 and the Python script used in the present thesis in Appendix B.2.2 (this algorithm was derived from [7]).

Another common problem in acceleration measurements is the so called *aliasing* phenomenon [18]. Aliasing errors appear when the sampling period (time difference between two adjacent measurements) is too large compared to the (high-frequency) vibration period. It is evident that, this phenomenon is closely related to filtering but it can not be compensated by filtering. The most effective solution against aliasing errors, is the usage of a sufficiently small sampling period, see subsection 5.4.2. In addition to this, the assignment of a small amount of lumped mass at the node of measurement is reducing aliasing errors [18].

### 5.3.1 Accelerations

In the present section, acceleration time-histories are given for the centre of mass of the car (node 700002) in Fig. 5.6 left and for the centre of mass of the dummy's head (node 8000001) in Fig. 5.6 right for all the speed classes. Moreover, the calculated values of ASI and HIC36 are shown at the corresponding acceleration time-history plots.

[1] It should be noted that the internal code for the calculation of the HIC in LS-DYNA, filters the resultant accelerations directly and the HIC results are misleading.

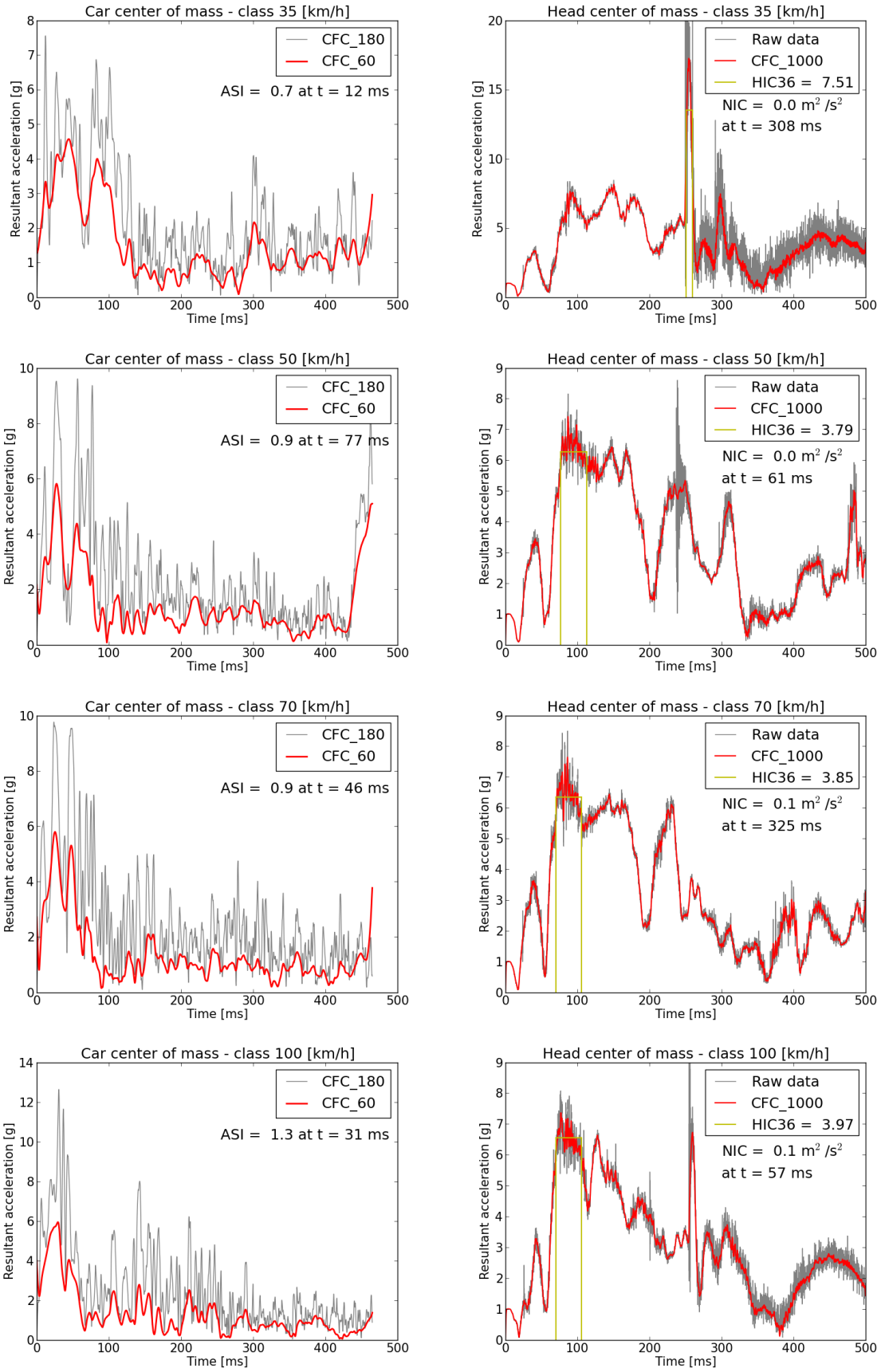


Figure 5.6: Acceleration time-histories for speed classes 35, 50, 70 and 100 km/h. **Left** filtered accelerations of node 700002 at the car centre of mass. **Right** filtered and raw accelerations of node 8000001 at the head centre of mass.

The amplitude of high frequency vibrations at the acceleration recordings of node 700002 is 100 times larger than the physical acceleration values. For that reason, only the filtered acceleration data and not the raw data are shown for this node. This is not evident in the acceleration data of node 8000001, because the amplitude of high frequency vibrations is much lower, and thus the raw data are shown as well. The fact that the high frequency vibrations do not influence the acceleration recordings of that node, can be explained by the fact that neither the head nor the dummy is rigidly connected to any part of the car and vibrations are not being transferred to that node. In other words, the neck and/or the dummy and/or the seat, act as vibrational isolators of the head.

The difference between the filtered accelerations in Fig. 5.6 left, is explained by the fact that the raw measurements for this node are dominated by the high amplitude (and high frequency) vibrations. As a result, the values of acceleration decreases for decreasing filter cut-off frequency because the filtering is applied for each acceleration component separately. This is not evident in Fig. 5.6 right, because these non-physical vibrations are not dominant in the acceleration recordings of this particular node.

### 5.3.2 Velocities

The velocity measurements are not generally influenced by high frequency vibrations, and thus, their time-histories are much less 'noisy' compared to the accelerations. In the present section, plots of raw and filtered velocity data are being shown for the different impact speed classes, see Fig. 5.7. The corresponding THIV value is plotted as well.

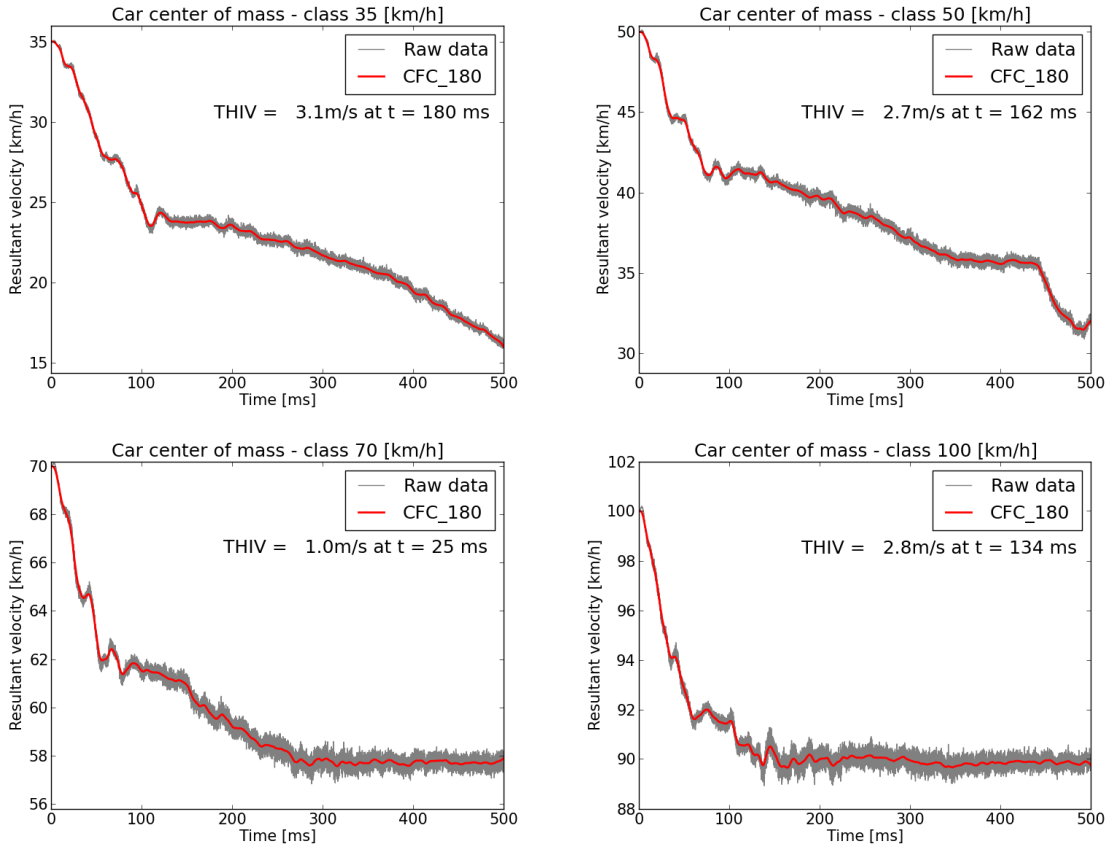


Figure 5.7: Velocity time-histories of node 700002 at the centre of mass of the car for speed classes 35, 50, 70 and 100 km/h.

In Fig. 5.7, it can be observed that the value $v_{impact} - v_{exit}$ increases as the impact speed decreases, for the speed classes 35, 50, 70 and 100 km/h, $v_{impact} - v_{exit} = 18.9$, 17.7, 12.0 and 10.2 km/h respectively. In addition to this, the THIV value is larger for the low impact speed test of 35 km/h. The same holds for the HIC36 value in Fig. 5.6 right. As a result, the THIV, an index of severity of the impact that refers to the head, and the HIC36, an injury index that also refers to the head are larger for the impact test of 35 km/h. The ASI value on the other hand, which is an impact severity index that refers to the car is larger for the speed class of 100 km/h. As a result, from Fig. 5.6 and 5.7, we can extract the conclusion that in high impact speeds, the impact is more severe by means of car body accelerations, but in view of head loading and injury, the low speed test is more critical.

In all the impact tests of the different speed classes, the occupant safety criteria in Table 2.3 for the ASI and THIV values are totally fulfilled. In addition to that, the HIC36 values were all much lower than the maximum value tolerated by the human body which equals to 1000.

## 5.4 VERIFICATION

In the present section, the quality of the numerical solutions is verified in three different ways. First, the energy balance of the impact simulations of the different speed classes is checked for validity. Second, the integration of the 'noisy' raw acceleration data of node 700002 (centre of mass of the car) is performed and compared to the velocity time-histories. This is done for two reasons, a) to check if the numerical noise influences the results and b) if the sampling rate for the accelerations does not result to aliasing errors. Finally, a numerical experiment of the car impacting a rigid wall is curried out to verify the car and dummy model behaviour and compare it to other experimental results.

### 5.4.1 Energy balance

In the present subsection, the energy balance of the system in the impact simulation is given for all the time steps of the analysis for the different speed classes.

In Fig. 5.8, it can be observed that the hourglass energy is small, which indicates that the quality of the solution is not influenced by the hourglass phenomenon. Moreover, a small amount of sliding energy exists because friction has been assumed between the vehicle and the structure. The internal energy appears to increase with decreasing kinetic energy as expected, but an increase can be observed in the total energy of the system, especially for the low speed classes. This is not valid because the system is closed and does not interact with the environment energetically.

The increase in the total energy does not dramatically influence the quality of the solution, because in [36], it is mentioned that the use of single-surface contacts (contact of an object to itself, see 4.5.3) like the one that refers to the whole structure, tend to increase the total energy of the system. This explains the increase in the total energy of the low speed classes. In low speeds, the deformation of the structure is slower, and thus the amount of calculations concerning the single-surface contact is higher compared to higher speed cases. This is the reason why in the energy balance for the speed class 100 km/h no increase in the total energy is observed.

In addition to that, given that the total mass of the car with the dummy (and the seat) is $m_{tot} \approx 940$ kg, it is possible to verify the initial kinetic (and total) energy of the plots in Fig. 5.8 using the formula

$$E_{kinetic} = \frac{1}{2} \cdot m_{tot} \cdot v_0^2. \tag{5.1}$$

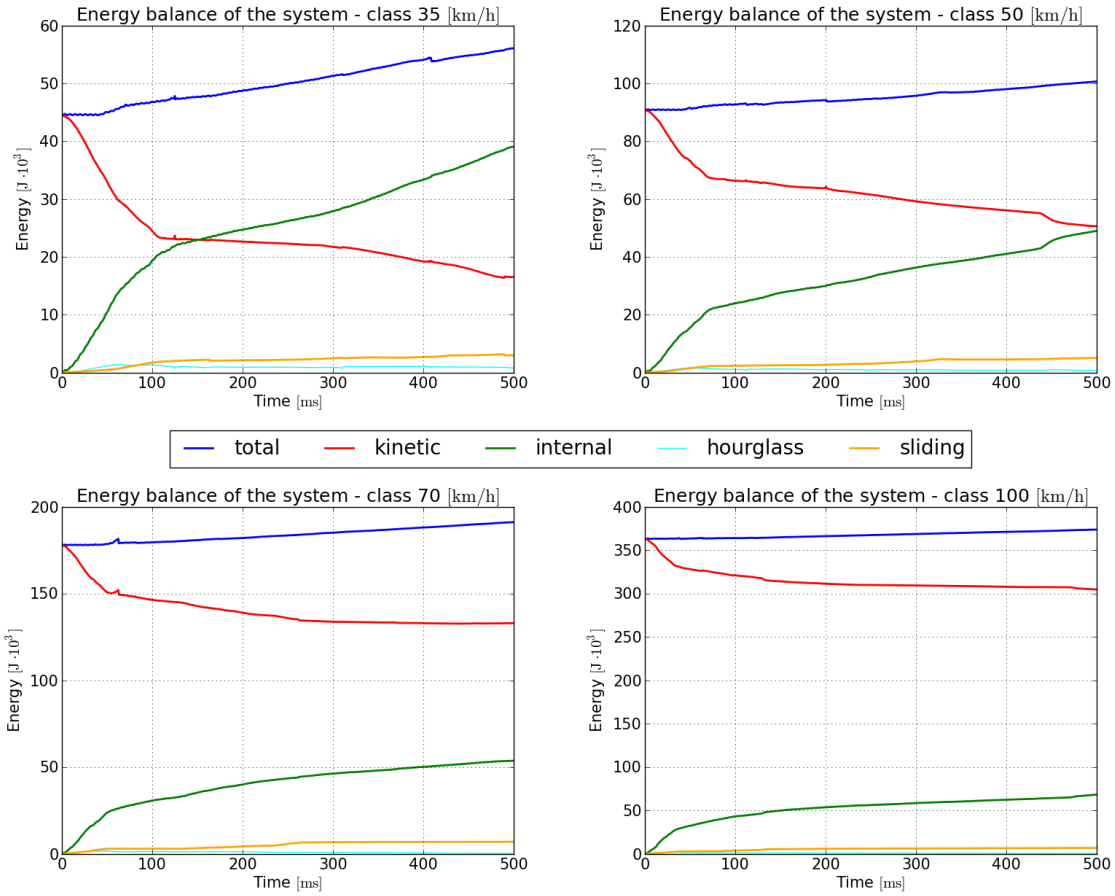


Figure 5.8: System energy time-histories for speed classes 35, 50, 70 and 100 km/h.

For $v_0 = 35, 50, 70, 100$ km/h the initial kinetic energy is $E_{kinetic} = 44.425, 90.663, 177.700, 362.654$ J $\cdot 10^3 =$ MJ. These values can be verified from Fig. 5.8.

### 5.4.2 Integration of accelerations

In order to verify the quality of the acceleration measurements for node 700002, the coincidence between the corresponding velocity measurements and the integrated accelerations, is being checked for a 113.6 km/h impact test. Due to the fact that acceleration $a$ is the first time derivative of velocity $v$, it holds

$$a = \dot{v} \Rightarrow v(t) = v(0) + \int_0^{t_{end}} a(t)\mathrm{d}t, \tag{5.2}$$

where $v(0)$ is the impact speed. In Fig. 5.9, the plots of velocity and the acceleration integral are given against time for increasing sampling rate (decreasing sampling period).

It can be observed in Fig. 5.9, that the acceleration measurements are not correct for sampling periods 0.5 and 0.05 ms. This happens because of the aliasing phenomenon (see subsection 5.3 *"Filtering"*), which practically means that the sampling period is larger than the period of the unphysical high-frequency vibrations. As a result, these vibrations are only partially recorded and the acceleration measurements are useless. If on the other hand, the sampling period is smaller than the vibration period, these vibrations are fully recorded and they influence the accelerations in

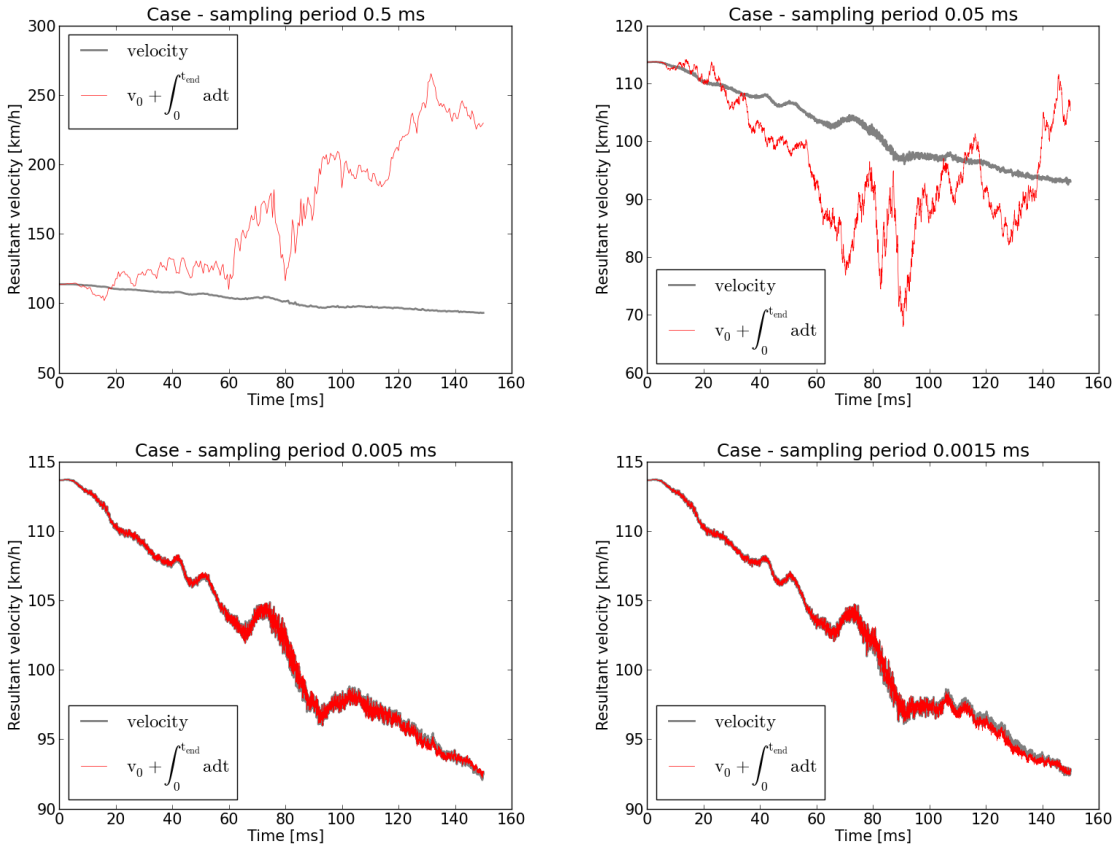


Figure 5.9: Velocity and integral of acceleration time-histories of node 700002 at the centre of mass of the car for sampling periods 0.5, 0.05, 0.005 and 0.0015 ms.

uniform manner. In that case the acceleration measurements are correct (see Fig. 5.9 for sampling periods 0.005 and 0.0015 ms), and useful information can be extracted after proper filtering.

### 5.4.3 Impact against rigid wall

In the present subsection, the results of a numerical experiment of the car impacting against a rigid wall with an impact speed of 50 km/h are being shown.

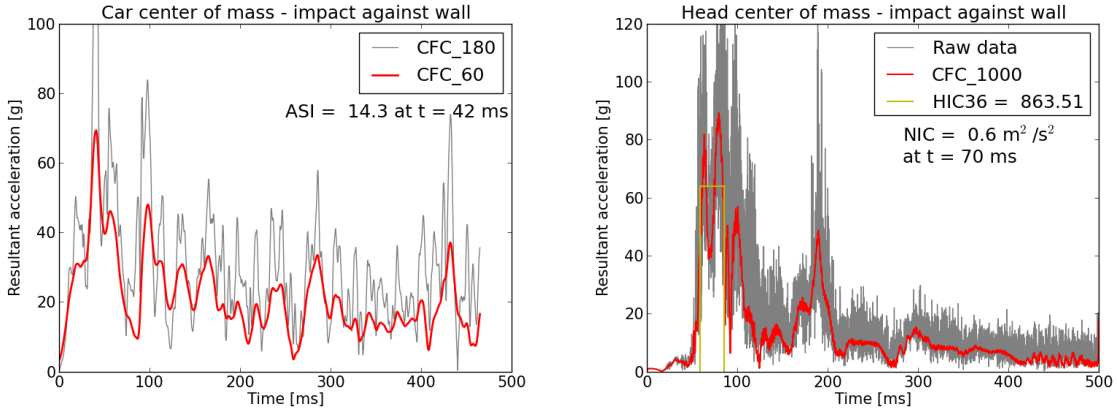


Figure 5.10: Acceleration time-histories for impact against wall, with impact speed equal to 50 km/h. **Left:** filtered accelerations of node 700002 at the car centre of mass. **Right:** filtered and raw accelerations of node 8000001 at the head centre of mass.

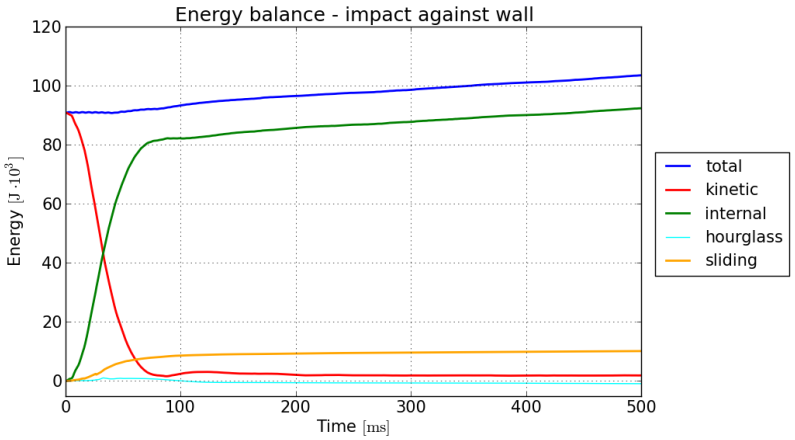


Figure 5.11: System energy time-histories for impact against rigid wall with initial speed equal to 50 km/h.

This experiment is performed in order to check the behaviour of the car and the dummy and to compare the measured accelerations with experimental results. In Fig. 5.10, the acceleration time-histories are given for this experiment. The acceleration values are much higher compared to the impact against the support structure case. The same holds for the severity and injury indices; the ASI value is 14.3, the HIC36 value is 863.5 where the limit for serious injury is 1000 and the NIC value is 0.6 $m^2/s^2$ where the maximum is 15 $m^2/s^2$. As a result, the occupant faces a small risk of head injury because the HIC36 value is close to the maximum. This risk is not very large, as expected for a car crash against a rigid wall including seatbelt and airbag, because the HIC36 is still below the maximum.

In Fig. 5.11, the energy balance during the impact is shown. The energy balance seems to be valid except the small increase in the total energy due to the presence of single-surface contacts within

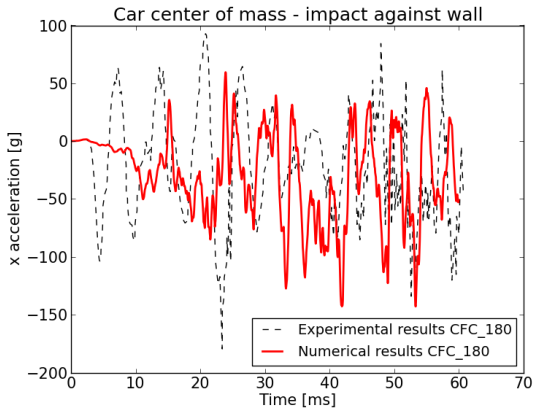


Figure 5.12: Experimental results of impact of unknown car model against wall, with impact speed 56 km/h and numerical results from impact-against-wall simulation both filtered with CFC_180.

the car model. The sliding energy is sufficiently higher than for the impact test against the support structure for the speed class of 50 km/h. This happens because the wall is undeformable which is translated to higher normal forces between car and wall and thus higher friction forces along this contact surface. The influence of hourglass is omittable due to the fact the hourglass energy is almost zero.

In Fig. 5.12, the $x$ acceleration component filtered using CFC_180 low pass filter (see Appendix B.2.1) is plotted together with the same acceleration component derived from a real car crash test of an unknown car model against rigid wall. The experimental results were derived from [16] where they are already filtered using a low pass filter of class CFC_180. In [16] it is stated that experimental and numerical results can be compared to each other when they are both filtered using low pass filter of class CFC_180. This statement is verified in Fig. 5.12, where it can be observed that the two acceleration components are fairly similar.

Images of the impact for different time steps are being shown in Fig. 5.13. The severity of the impact is obvious in the behaviour of the dummy and its head, which comes in contact with the airbag in contrast to the impact against the support structure.

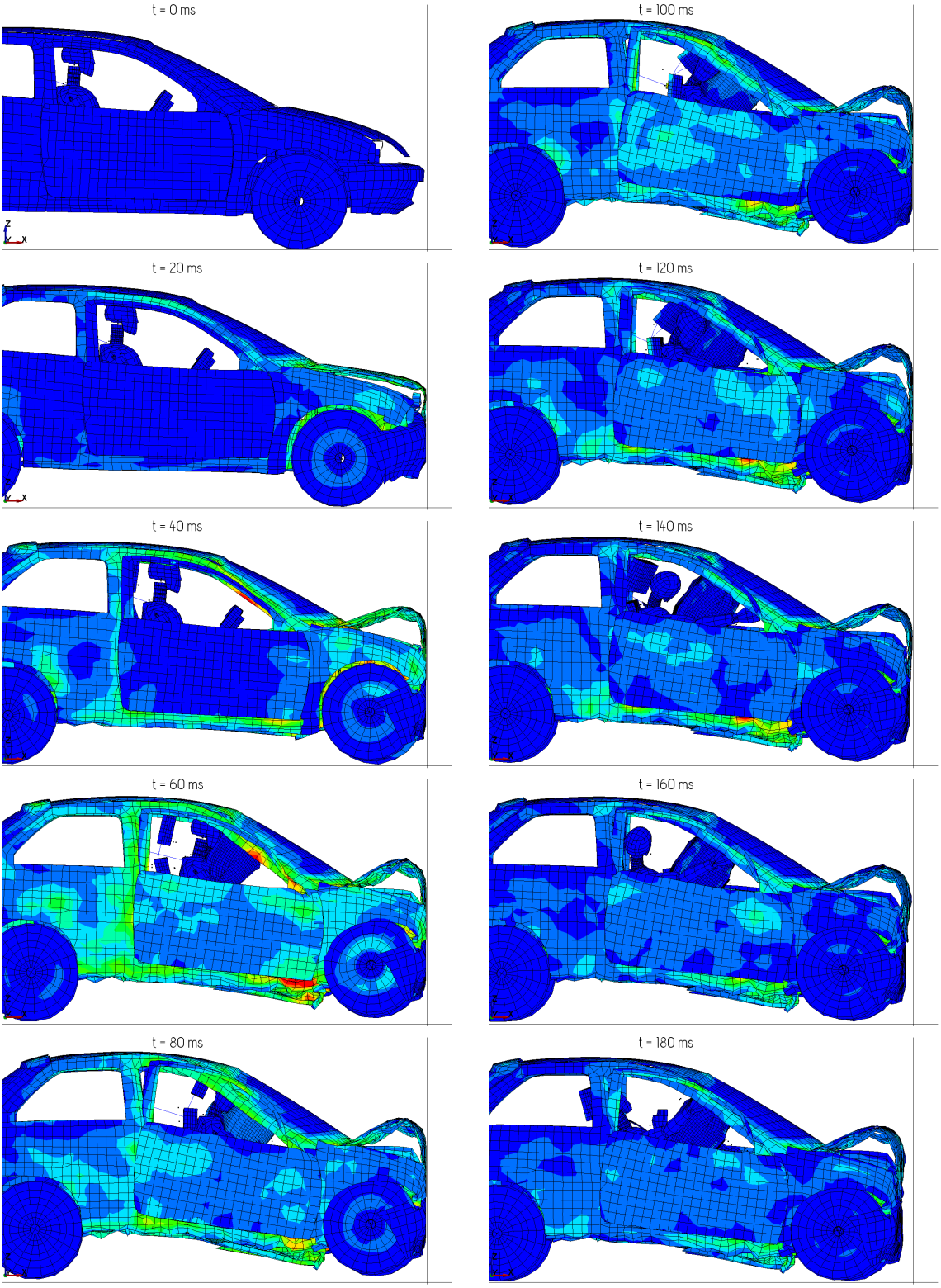


Figure 5.13: Von-Misses stress distribution in GPa for different time steps in side view for a 50 km/h impact against wall numerical experiment.

### 5.4.4 Comparison with real impact test

In the present subsection, the results of a real impact test against a sign support structure fairly similar to the studied one, are being shown and compared to the numerical results. The sign support structure used in the real test is shown in Fig. 5.14 left, while the test set-up in Fig. 5.14 right.

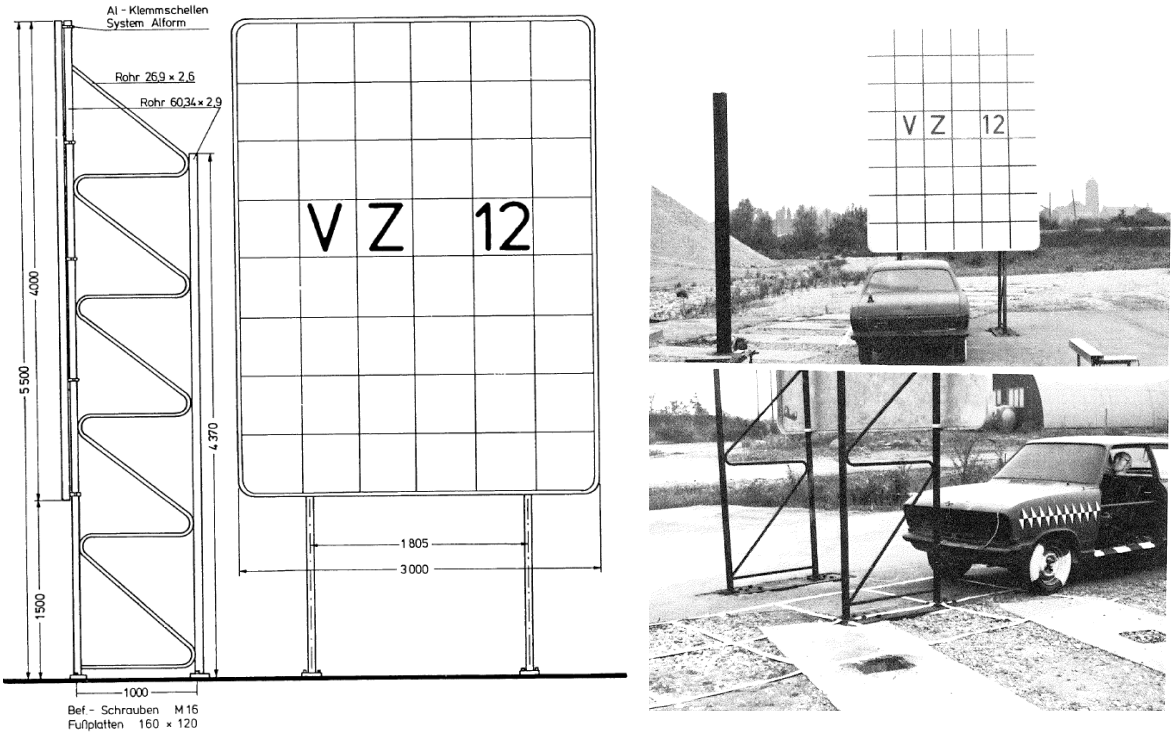


Figure 5.14: Real impact test. **Left:** tested sign support structure. **Right:** set-up of the test. [45]

The results were derived from [45] and are summarized in the test report which can be found in Appendix A.3. It can be observed, that the geometry of the tested structure is only slightly different compared to the one studied in the present thesis. The height and the elevation of the sign in the real test are $4\ \mathrm{m}$ and $1.5\ \mathrm{m}$ respectively, while in the numerical test they are $3\ \mathrm{m}$ and $1.22\ \mathrm{m}$. Moreover, in the real test, the distance between the vertical pipes of the truss, is $1\ \mathrm{m}$ while in the numerical test, it is $0.5\ \mathrm{m}$. The dimensions of the pipes of the truss are exactly the same in both cases. The impact speed and angle in the numerical test were chosen equal to $93\ \mathrm{km/h}$ and $90\ °$ (or $0\ °$), which are the actual boundary conditions of the real test.

The accelerations measured at the centre of mass of the car for the numerical test, are shown in Fig. 5.16.

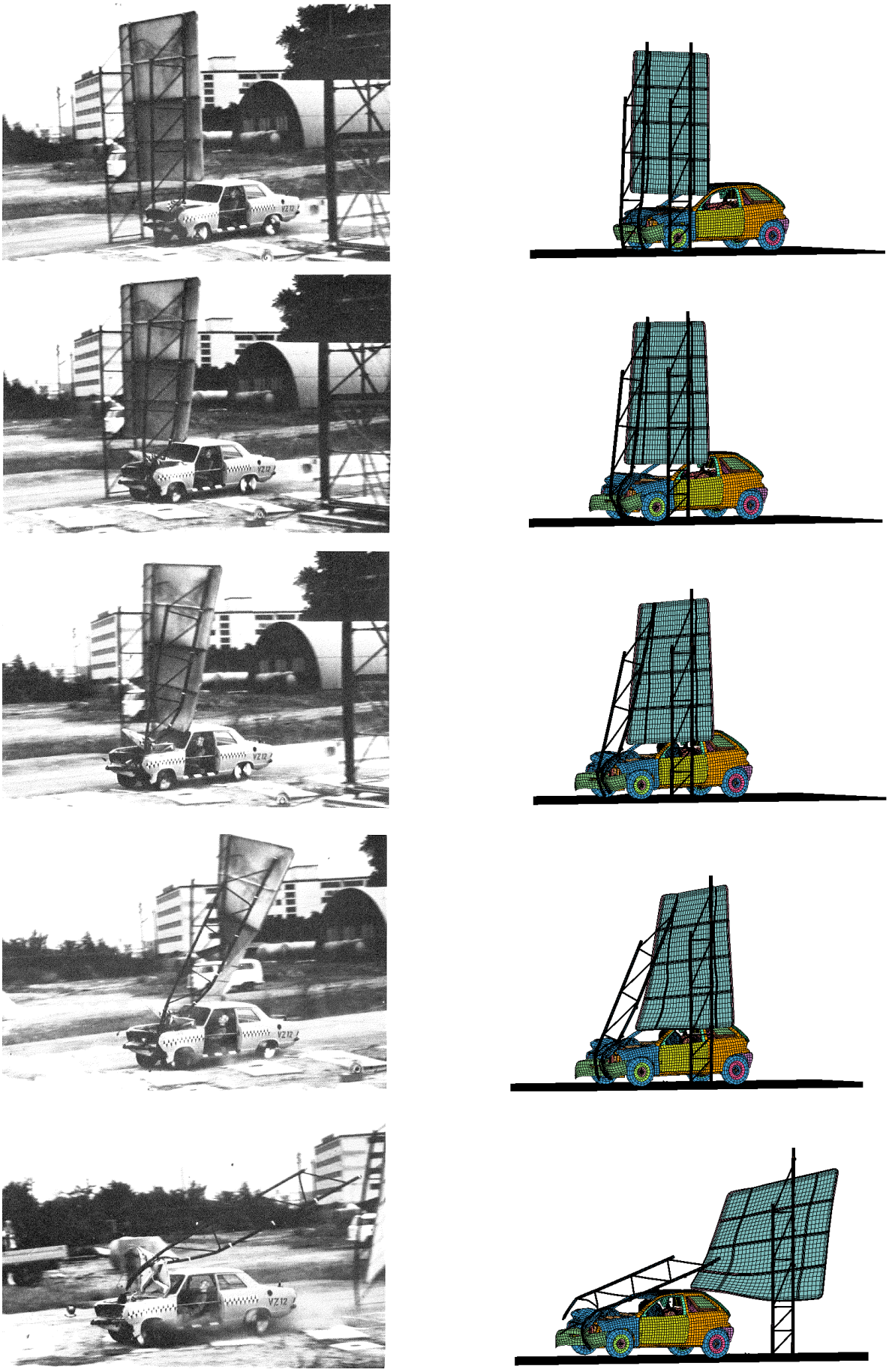

Figure 5.15: Vehicle and structure impact behaviour. **Left:** real impact test [45]. **Right:** numerical impact test.

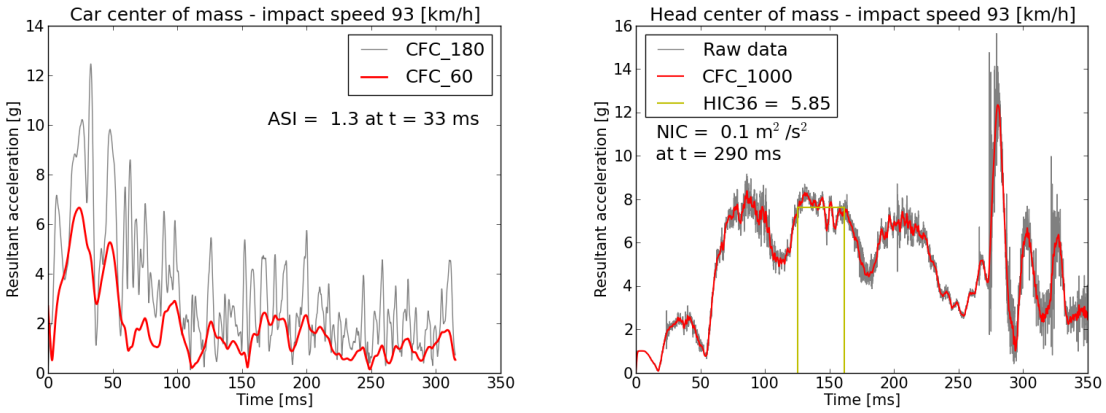


Figure 5.16: Acceleration time-histories for frontal impact with impact speed equal to 93 km/h. **Left:** filtered accelerations of node 700002 at the car centre of mass. **Right:** filtered and raw accelerations of node 8000001 at the head centre of mass.

In the test report, the maximum acceleration of the vehicle is reported equal to 9 g (see Appendix A.3). This value is exactly between the maximum CFC_60 and CFC_180 filtered accelerations, as can be observed in Fig. 5.16 left. As a result, the computational maximum acceleration is verified by the real test results, despite the fact that the filtering frequency used for the calculation of the real test value is not known. The ASI value of the real test is reported equal to 0.31 (see Appendix A.3), which is significantly lower than the value derived from the numerical test. This can be attributed to the fact that the real test was performed many years before, and the ASI calculation process as well as the digital filtering technology may have change. Additionally, in is stated in [4], that for the calculation of the ASI, the accelerations should be recorded many seconds before and after the impact. This is not possible in the computer simulation due to numerical efficiency reasons.

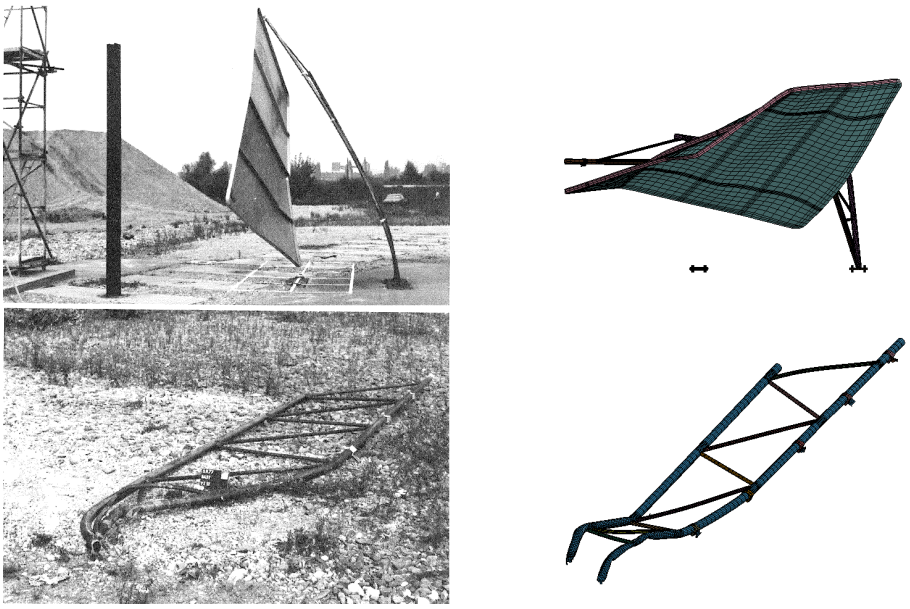

Figure 5.17: Condition of the structure after the impact. **Left:** real impact test [45]. **Right:** numerical impact test.

The general behaviour of the vehicle in the two cases, real impact test and numerical impact test, are compared in Fig. 5.15. It can be observed, that the behaviour of the vehicle is fairly comparable in the two cases. Moreover, in Fig. 5.17, the condition of the structure after the impact is compared

for the two cases and found also fairly similar.

In the test report of the real test in Appendix A.3, the test procedure is summarized in the following statement, that can suitably summarize the test procedure of the numerical test as well.

> *" The test vehicle tore-off the approached stand and continued, while the stand was thrown over the vehicle. The sign touched the roof and which was slightly damaged. "*

### 5.4.5 Comparison with real traffic accident

In Fig. 5.18, the destroyed truss of the numerical test, is compared with a similar destroyed truss after an traffic accident in the highway BAB A44 near Hagen, Germany at 15.04.2013. In this incident, an Audi car, crashed against a sign support structure of type DU76, which is similar to the studied one.

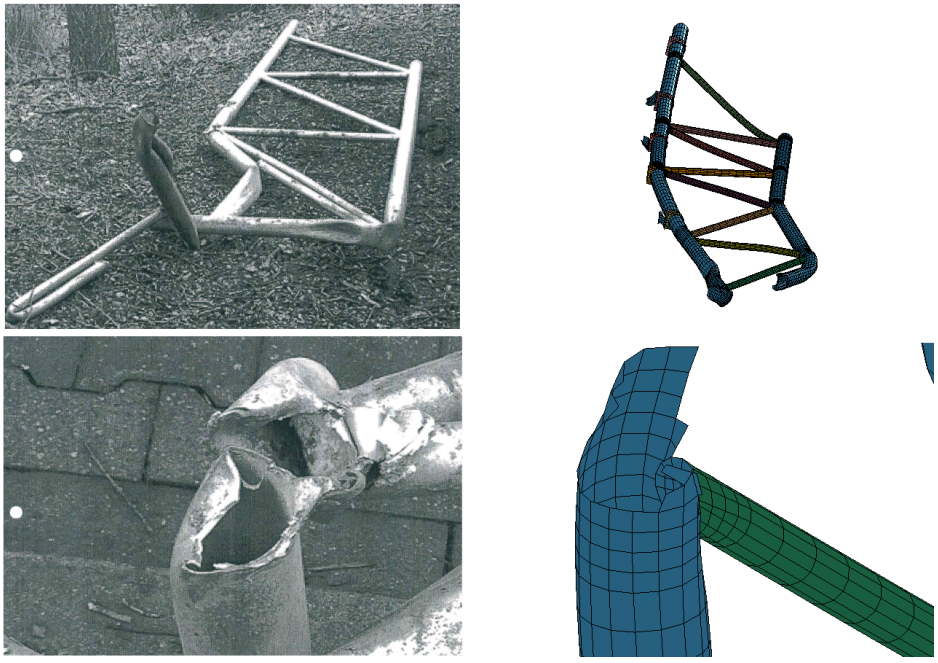

Figure 5.18: Destroyed truss. **Left:** real accident. **Right:** numerical impact test.

The two cases are generally comparable. The differences in the deformation of the pipes between the two cases, is attributed to different initial geometry, vehicle type, foundation type and impact boundary conditions (speed and angle). Moreover, in the real accident, the influence of surrounding objects such as trees and highway embankments is possible.

# 6 UNCERTAINTY

## 6.1 INTRODUCTION

Structural analysis of dynamical problems such as the problem of vehicle-structure impact simulation, involve a sufficient amount of uncertainty. It arises from physical variations and imprecise knowledge of loading conditions, material parameters etc. as *data uncertainty* and from simplifications of the numerical model employed for the calculations, as *model uncertainty*.

Data uncertainty is a comprehensible term; it refers to the input parameters and it exists before the structural design and analysis starts. As the steps of the analysis proceed, data uncertainty propagates and it finally influences the results which become uncertain. Data uncertainty is quantifiable, i.e. it is possible to use experimental results and evaluate the statistical properties of the uncertain data. Given that these statistical properties have been accurately estimated (e.g. by a large number of effective experiments), then the only characteristic of uncertainty in the data, is *variability*. In this later case, if the data are not characterized *a priori* by variability, then the experimental results produce deterministic values, which means that the data is not uncertain any more. This type of uncertainty is referred to as *aleatoric uncertainty*.

In practical applications however, the statistical properties of the uncertain data are not always reliable, because of two reasons. First, only a small number of experiments is usually available, i.e. the data is incomplete, and second, the quality of the experiments is possible to be low, i.e. the data is imprecise. *Incompleteness* and *impreciseness* are two uncertainty characteristics generally based on lack of information. The type of uncertainty associated with lack of information is referred to as *epistemic uncertainty*.

Model uncertainty on the other hand, refers to the numerical analysis of the studied problem. It arises due to simplifying assumptions and approximations during the development of both the physical and the numerical model. In some cases, it is possible to decrease model uncertainty (e.g. mesh refinement), but it is not possible to quantify it; moreover, it is often difficult to detect it. Parameters of the numerical model that have no actual physical significance, tend to introduce uncertainty, especially if they are not carefully chosen. Usually, only lexically stated assessments (e.g. small, large, very large etc.) of such parameters are available and thus they are characterized by impresiceness, which is a characteristic of epistemic type.

## 6.2 DETERMINISTIC SOLUTION

Uncertainty analysis is based on a deterministic fundamental solution of the studied problem. This solution has to be evaluated many times (usually more than 10000) during the analysis, with different variants of the set of input parameters. In the present study, the deterministic fundamental solution is the computationally expensive Finite Element Analysis of the impact simulation problem. It is obvious that the multiple evaluation of the deterministic solution in that case, increases dramatically the computational cost of the uncertainty analysis, which in most of the cases becomes unfeasible.

The *metamodel* approach has been adopted as a practical solution to the computational efficiency problem [20]. This approach is based on the idea of constructing a very simple numerical model that is able to surrogate the complex original model by means of importing a set of input values and approximate one or more output values. The original model, is described by the mapping

$$f := \mathbb{R}^m \rightarrow \mathbb{R}^k : \mathbf{x} \mapsto \mathbf{y},$$

while the metamodel is described by the mapping

$$f_{MM} := \mathbb{R}^m \rightarrow \mathbb{R}^k : \mathbf{x} \mapsto \mathbf{y}^*.$$

Where $m$ is the number of dimensions of the input vector, and $k$ the number of dimensions of the output vector. The symbol $*$ is used to denote approximated (by the metamodel) values and the subscript MM stands for metamodel.

The ranges of the values of the input parameters are specified in advance; this is the second important step of an uncertainty analysis after the choice of the uncertain parameters. Subsequently, the response parameter(s) is evaluated by the original model using a number of $n$ different combinations of the input parameters within the specified ranges. As the number $n$ of the original solutions-experiments increases, the quality of the metamodel approximation increases as well.

For the construction of the metamodel, various methods have been introduced. Two of the most effective are *Artificial Neural Networks* (ANN) [43],[41] and *Radial Basis Function Networks* (RBFN) [15]. The second approach was chosen in the present study because it is faster and more accurate for small sample sizes [32]. In the RBFN approach, the metamodel is approximated by a sum of Gaussian functions properly positioned in the input $x$ space, weighted by appropriate shape factors. The choice of the positions of the Gaussian functions as well as the shape factor of each of them, is of major importance in this approach. In the present study, the metamodel was constructed using the tool 'MetaModelMaker'.

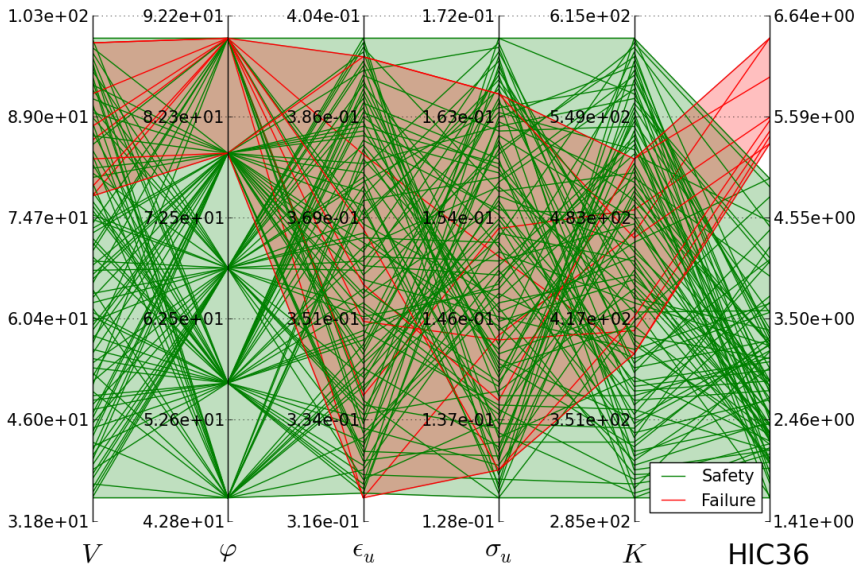


Figure 6.1: Parallel coordinate plot of the 100 original analyses. The red and green lines indicate variants that lead to failure and safety respectively.

At first, the input data set (100 $\times$ 5 matrix, 5 dimensions by 100 experiments) is determined within the specified intervals (see Table 6.1) using the Latin Hypercube Method (LHS); this procedure is

referred to as *Design of Experiments*. For each input vector (of length 5), an impact simulation is performed using LS-DYNA and one value of HIC36 is being calculated; this procedure, together with the Design of Experiments, is referred to as *variation analysis*. Subsequently, the 100 input vectors together with the 100 calculated HIC36 values were introduced in the tool 'MetaModelMaker', which constructed the metamodel. The result is a very simple model that imports an arbitrary input vector (the values should be within the specified intervals) and outputs a HIC36 value based on the original solutions. It should be noted that 70 % of the data was used to train (develop) the metamodel while the rest 30 % was used to test it.

The range of the output values, (HIC36 values) is [1.65, 6.40]. These HIC36 values are very low compared to the maximum HIC value tolerated by the human body which is 1000. This means that there is no risk for serious injury. For that reason a limit value of 5.3 is introduced; HIC36 values more than 5.3 are assumed as injury (failure). In Fig. 6.1 a parallel coordinate plot of the 5 input parameters is shown.

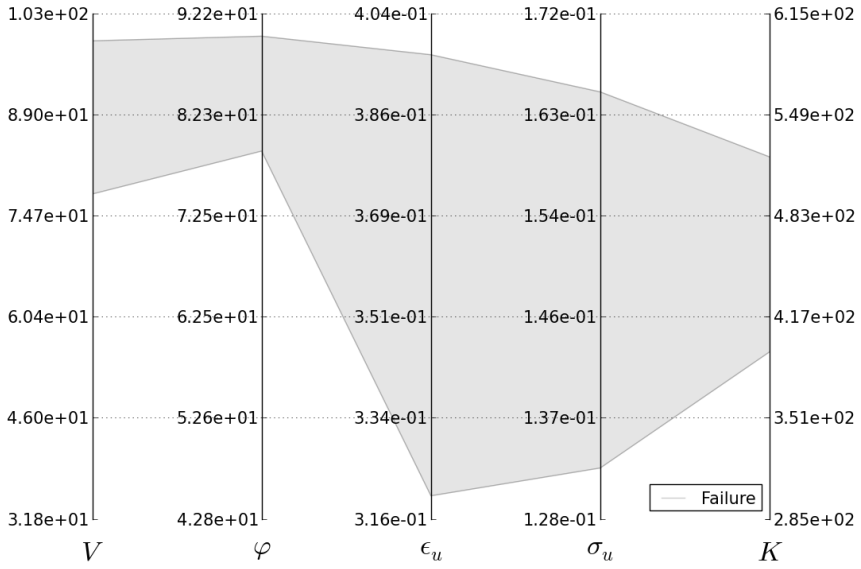


Figure 6.2: Parallel coordinate plot of the non-permissible design subspace.

Each one of the first five vertical black lines represents one input parameter while the sixth vertical line represents the output value. The green lines represent combinations of input parameters that lead to HIC36 values lower than 5.3 (no failure) and the red lines to HIC36 values larger than 5.3 (failure). In Fig. 6.2 another parallel coordinate plot is shown which contains the input parameters only. The shaded part depicts the non-permissible design subspace of the input $x$ space, i.e. input values within that space lead to failure, while values out of it lead to safety. The procedure for detecting the permissible and non-permissible design subspaces which concludes to the plot in Fig. 6.2, was introduced in [21].

## 6.3 UNCERTAINTY MODELLING

Different mathematical models have been developed to assess uncertainty characteristics within the computational framework. Parameters of the numerical model that possess aleatoric uncertainty (variability) only, can be modelled using *random variables*[1], see [22] and [44]. Parameters associated with epistemic uncertainty (impreciseness and/or incompleteness), for which only subjective, lexical or linguistic assessments are available, can be modelled as *fuzzy variables*[2] or *fuzzy sets*, according to [42] and [40]. Random variables derived from probability theory and fuzzy variables derived from fuzzy set theory, can be combined into generalized models that can describe parameters that exhibit different uncertainty characteristics simultaneously (e.g. variability-incompleteness, variability-incompleteness-impreciseness) [22],[42].

In the impact simulation problem of the present thesis, five input parameters were chosen as uncertain. These parameters include the test boundary conditions impact speed $v$ and impact angle $\varphi$ (see Fig. 6.3), the parameters stress at failure $\sigma_u$ and effective plastic strain at failure $\epsilon_u$ of the welded connection between truss and plate (see subsection 3.1.2), as well as the elastic constant $K$ of the spring used at the connection between plate and bolt (see subsection 3.1.2). The output variable which has been chosen as the critical response parameter is the Head Injury Criterion (HIC) value, measured within a time interval of maximum $36$ ms, which is denoted as HIC36.

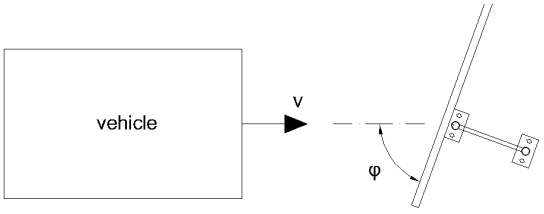


Figure 6.3: Depiction of the uncertain parameters impact speed $v$ an impact angle $\varphi$.

The test boundary conditions $v$ and $\varphi$, are characterized by the uncertainty characteristic incompleteness, because extended statistical information about their values are not available. They are also characterized by variability, because even if the available data were complete, these parameters still posses a physical variation. As a result, they can be best modelled using fuzzy random variables [22]. The failure parameters $\sigma_u$ and $\epsilon_u$ of the welded connection are characterized by the uncertainty characteristic impreciseness, due to the fact that both the physical and the numerical models that describe the behaviour of the weld introduce some approximation error. In addition to this, these parameters exhibit some physical variation, and thus they can be best modelled as fuzzy random variables as well. A fuzzy random variable can be understood as a random variable described by a distribution function the parameters of which are defined as fuzzy variables (see definition B.3 in Appendix B.1).

Finally, the stiffness of the elastic spring $K$, is a parameter of the numerical model only and has no physical significance. As a result it is characterized only by the uncertainty characteristic impresiceness and thus it can be best modelled as fuzzy variable. The uncertain variables involved in the present study are summarized in Table 6.1.

[1] See definition B.1 in Appendix B.1.
[2] See definition B.2 in Appendix B.1.

Table 6.1: Uncertain variables

| Parameter | | Deterministic value | Interval | Uncertainty characteristics | Uncertainty model |
|---|---|---|---|---|---|
| Impact speed | $v$, $\left[\frac{\mathrm{km}}{\mathrm{h}}\right]$ | 67.5 | [35, 100] | variability, incompleteness | fuzzy random variable |
| Impact angle | $\varphi$, [°] | 67.5 | [45, 90] | variability, incompleteness | fuzzy random variable |
| Weld failure stress | $\sigma_u$, [ GPa] | 0.36 | [0.32, 0.40] | variability, impreciseness | fuzzy random variable |
| Weld failure strain | $\epsilon_u$, [-] | 0.15 | [0.13, 0.17] | variability, impreciseness | fuzzy random variable |
| Spring stiffness | $K$, $\left[\frac{\mathrm{kN}}{\mathrm{mm}}\right]$ | 450 | [300, 600] | impreciseness | fuzzy variable |

## 6.4 UNCERTAINTY ANALYSIS

For the computational realization of the fuzzy analysis a global optimization concept is selected as $\alpha$-level optimization in conjunction with a modified evolution strategy, see [40] and [42]. For different levels $\alpha \in (0, 1]$ of membership, the crisp subspace $\mathbf{X}_\alpha \subset \mathbb{R}^n$ is defined as the intersection between the membership functions of the $n$ input parameters and the horizontal plane at level $\alpha$. In Fig. 6.4, the yellow rectangle represents the subspace $\mathbf{X}_\alpha$ for a two dimensional case. In

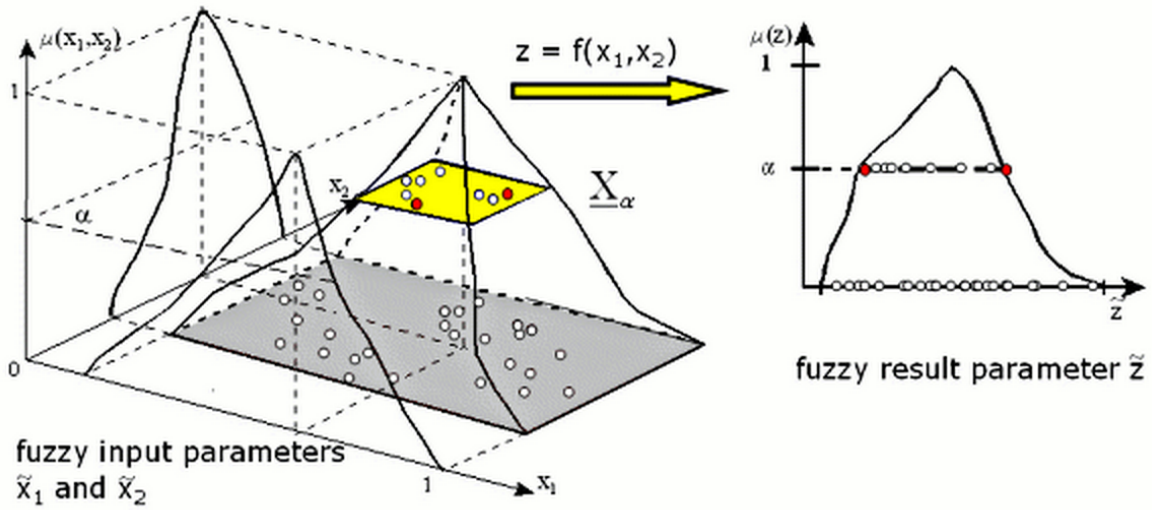


Figure 6.4: Mapping of the fuzzy input variables $\tilde{x}_1$ and $\tilde{x}_2$ onto the fuzzy result variable $\tilde{z}$

order to calculate the limit values of the membership function of $\tilde{z}$ at the membership level $\alpha$, the optimization problem in Eq. (6.1) and (6.2) needs to be solved.

$$z_{\alpha,right} = f(x_1, ..., x_n) \Rightarrow \max | (x_1, ..., x_n) \in \mathbf{X}_\alpha \tag{6.1}$$

$$z_{\alpha,left} = f(x_1, ..., x_n) \Rightarrow \min | (x_1, ..., x_n) \in \mathbf{X}_\alpha \tag{6.2}$$

The solution of (6.1) and (6.2) is performed numerically using the modified evolution strategy, a combination of evolution strategy, the Monte Carlo simulation method and the gradient method according to [40] and [42].

Due to the fact that some uncertain parameters in the present study are characterized by variability and they are modelled as fuzzy random variables, the combined approach of Fuzzy Stochastic Analysis (FSA) is used, see [40] and [48]. The procedure of the FSA is summarized in Table 6.2 where $F_{FA}$, $F_{SA}$ and $F_{FSA}$ stand for fuzzy analysis, stochastic analysis and fuzzy stochastic analysis respectively. The symbol $\mathrm{d}$ represents the deterministic fundamental solution.

Table 6.2: Fuzzy stochastic analysis (FSA)

| | | | | | |
|---|---|---|---|---|---|
| $F_{FSA} := F_{FA}(F_{SA}(d))$ | | $\tilde{x}_1$ | $\boldsymbol{X}_2$ | $\tilde{\boldsymbol{X}}_3 := \boldsymbol{X}_3(\tilde{\boldsymbol{p}})$ | |
| $F_{FA}$: for $i = 1, ..., nf$ | | $x_1^i$ | | $\boldsymbol{X}_3(\boldsymbol{p}^i)$ | $\leftarrow$ |
| | $F_{SA}$: for $j = 1, ..., ns$ | | $x_2^j$ | $x_3^{ij}$ | $\uparrow$ |
| | $\mathrm{d}$ | $x_1 = x_1^i$ | $x_2 = x_2^j$ | $x_3 = x_3^{ij}$ | $z^{i*j}$ |
| $\tilde{P}_f$, $\tilde{\mu}_z$, $\tilde{\sigma}_z$ | | | | | |

In Table 6.2, a 3-dimensional problem that involves a fuzzy variable $\tilde{x}_1$, a random variable $\boldsymbol{X}_2$ and a fuzzy random variable $\tilde{\boldsymbol{X}}_3$, which is defined as a random variable that depends on the set of fuzzy parameters $\tilde{\boldsymbol{p}}$, is illustrated. In the fuzzy analysis loop (i loop), realizations $x_1^i \in \mathbb{R}$ of $\tilde{x}_1$ and $\boldsymbol{p}^i \in \mathbb{R}$ of $\tilde{\boldsymbol{p}}$ are generated during the $\alpha$-level optimization. $x_1^i$ is passed directly to the mapping model $\mathrm{d}$ while the parameters $\boldsymbol{p}^i$ are passed to the stochastic loop (j loop). In this loop, random realizations $x_2^j, x_3^{ij} \in \mathbb{R}$ are generated according to $\boldsymbol{X}_2$ and $\boldsymbol{X}_3(\boldsymbol{p}^i)$ respectively. Finally $x_2^j$ and $x_3^{ij}$ are passed to the mapping model $\mathrm{d} = \mathrm{d}(x_1, x_2, x_3)$ and the result value $z^{i*j}$ is evaluated and passed back to the fuzzy analysis loop.

The parameter *ns* represents the number of iterations of the stochastic analysis loop and is specified in advance. It is the sample size of each Monte Carlo Simulation and in the present studies it was chosen equal to 1000. The parameter *nf* on the other hand, which is the total number of iterations of the fuzzy loop, is not necessarily a fixed value. It may change according to the convergence properties of the optimization algorithm, but it's maximum value is specified in advance.

The results of the fuzzy analysis are probabilistic measures given in fuzzy interpretations. More specifically, the fuzzy probability of failure (given a limit state threshold value) $\tilde{P}_f$, the fuzzy mean value $\tilde{\mu}_z$ and the fuzzy standard deviation $\tilde{\sigma}_z$ of the result variable, are being calculated.

Table 6.3: Fuzzy parameters in the calculation

| Parameter | $\mu(x)_{LEFT} = 0$ | $\mu(x) = 1$ | $\mu(x)_{RIGHT} = 0$ | Units |
|---|---|---|---|---|
| $\tilde{v}_{min}$ | 35.0 | 38.0 | 41.0 | [km/h] |
| $\tilde{v}_{max}$ | 94.0 | 97.0 | 100.0 | [km/h] |
| $\tilde{\mu}_{\varphi}$ | 62.5 | 67.5 | 72.5 | [°] |
| $\tilde{\sigma}_{\varphi}$ | 5.9 | 7.9 | 9.9 | [°] |
| $\tilde{\mu}_{\sigma_u}$ | 0.355 | 0.360 | 0.365 | [ GPa] |
| $\tilde{\sigma}_{\sigma_u}$ | 0.013 | 0.014 | 0.015 | [ GPa] |
| $\tilde{\mu}_{\epsilon_u}$ | 0.145 | 0.150 | 0.155 | [–] |
| $\tilde{\sigma}_{\epsilon_u}$ | 0.0068 | 0.0070 | 0.0072 | [–] |

In Table 6.3, the fuzzy parameters that define the fuzzy random variables of the problem of the impact simulation are summarized. Triangular membership functions are used for their representation with lower limit (zero membership) $\mu(x)_{LEFT} = 0$, midpoint $\mu(x) = 1$ and upper limit (zero membership) $\mu(x)_{RIGHT} = 0$. The fuzzy parameters are realized in the fuzzy loop of the FSA, see Table 6.2.

Table 6.4: Fuzzy random variables in the calculation

| Fuzzy random variable | Distribution | defined by | fuzzy parameter 1 | fuzzy parameter 2 |
|---|---|---|---|---|
| $\tilde{v}$ | Uniform | limits | $\tilde{v}_{min}$ | $\tilde{v}_{max}$ |
| $\tilde{\varphi}$ | Normal | moments | $\tilde{\mu}_{\varphi}$ | $\tilde{\sigma}_{\varphi}$ |
| $\tilde{\sigma}_u$ | Normal | moments | $\tilde{\mu}_{\sigma_u}$ | $\tilde{\sigma}_{\sigma_u}$ |
| $\tilde{\epsilon}_u$ | Normal | moments | $\tilde{\mu}_{\epsilon_u}$ | $\tilde{\sigma}_{\epsilon_u}$ |

In Table 6.4, the fuzzy random variables of the problem, defined by the fuzzy parameters of Table 6.3 are summarized.

Table 6.5: Fuzzy variables in the calculation

| Fuzzy variable | $\mu(x)_{LEFT} = 0$ | $\mu(x) = 1$ | $\mu(x)_{RIGHT} = 0$ | Units |
|---|---|---|---|---|
| $\tilde{K}$ | 300 | 450 | 600 | $[\mathrm{kN/mm}]$ |

Table 6.5 contains the only fuzzy variable within the impact simulation problem which is the elastic stiffness of the spring $\tilde{K}$.

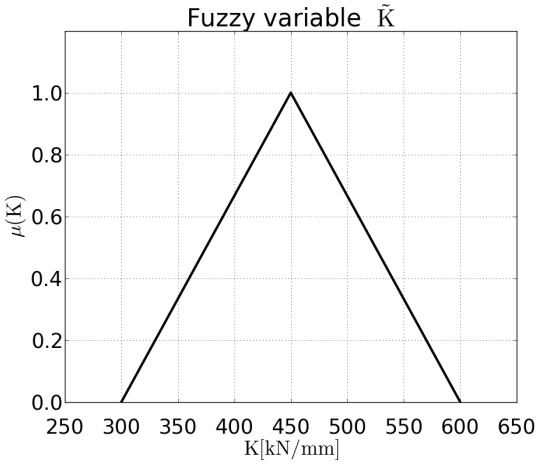


Figure 6.5: Membership function of the fuzzy variable $\tilde{K}$.

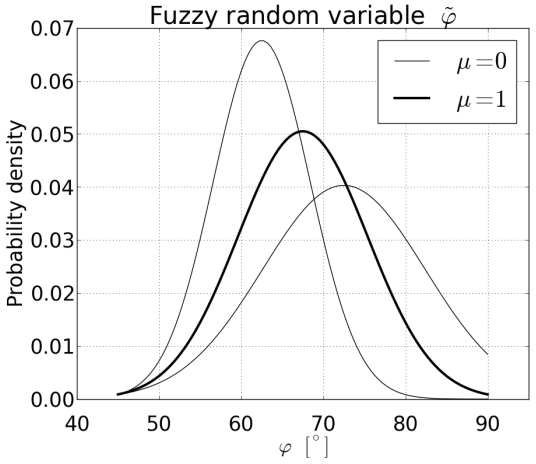


Figure 6.6: Family of probability density functions of the fuzzy random variable $\tilde{\varphi}$.

In Fig. 6.5 and 6.6, the membership function of the fuzzy variable $\tilde{K}$ and the family of probability density functions of the fuzzy random variable $\tilde{\varphi}$ are shown indicatively. In Fig. 6.6, the two zero membership probability density functions have been calculated using the combinations $\mu(\mu_{\varphi})_{LEFT}$-$\mu(\sigma_{\varphi})_{LEFT}$ and $\mu(\mu_{\varphi})_{RIGHT}$-$\mu(\sigma_{\varphi})_{RIGHT}$ for the mean values and standard deviations. It also possible to use the cross combinations $\mu(\mu_{\varphi})_{LEFT}$-$\mu(\sigma_{\varphi})_{RIGHT}$ and $\mu(\mu_{\varphi})_{RIGHT}$-$\mu(\sigma_{\varphi})_{LEFT}$, which would provide a mirror view of the plot in Fig. 6.6. Only one of these two possibilities is shown indicatively.

Subsequently, the input variables are discretized in a number of levels $\alpha$ of increasing membership, before the $\alpha$-level optimization (see Fig. 6.4) starts. In the present study, five $\alpha$-levels are used to discretize the fuzzy quantities, $\alpha$ = 0, 0.25, 0.5, 0.75, 1, see Fig. 6.7 and 6.8.

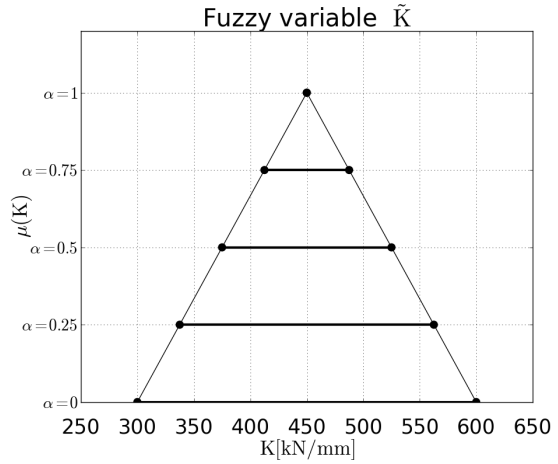


Figure 6.7: Membership function and $\alpha$-levels of the fuzzy variable $\tilde{K}$.

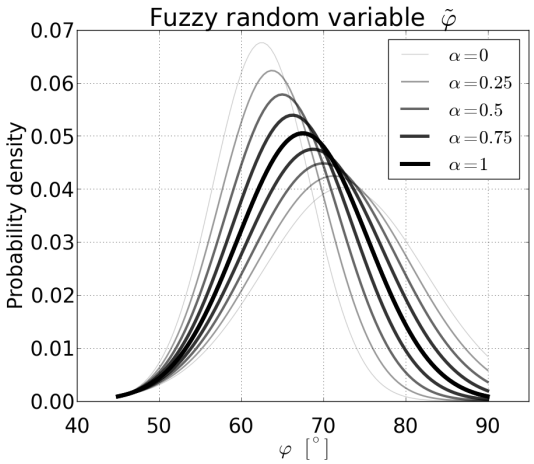


Figure 6.8: Family of probability density functions for the $\alpha$-levels of the fuzzy random variable $\tilde{\varphi}$.

## 6.5 RESULTS

As already mentioned, the results of the fuzzy stochastic analysis, are probabilistic measures with fuzzy interpretations. Hence, the fuzzy probability of failure $\tilde{P}_f$, the fuzzy mean value of HIC36 $\tilde{\mu}_{HIC36}$ and the fuzzy standard deviation $\tilde{\sigma}_{HIC36}$ are calculated and shown in Fig. 6.9-6.11.

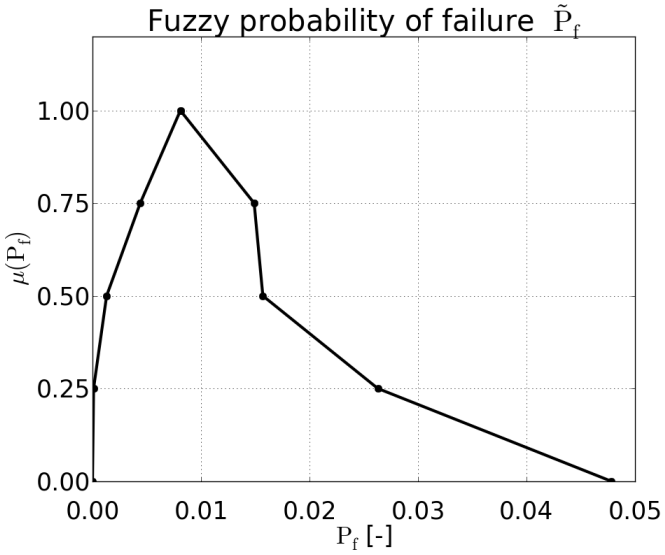


Figure 6.9: Fuzzy probability of failure $\tilde{P}_f$.

The membership function of the probability of failure, in Fig. 6.9, is gradually getting narrow and shifts to the left for higher $\alpha$-levels. This is evident because the threshold value of HIC36 that separates failure from survival was chosen equal to 5.3, which is close to the maximum HIC36

value and thus the probability of failure is small. In addition to that, the wide bottom part in the membership function, is because the ranges of the variables vehicle speed and the impact angle are wide as well. These variables are the most influential by means of the HIC36 value and for that reason the observed differences in the calculated values of the probability of failure are large in the lower $\alpha$-levels.

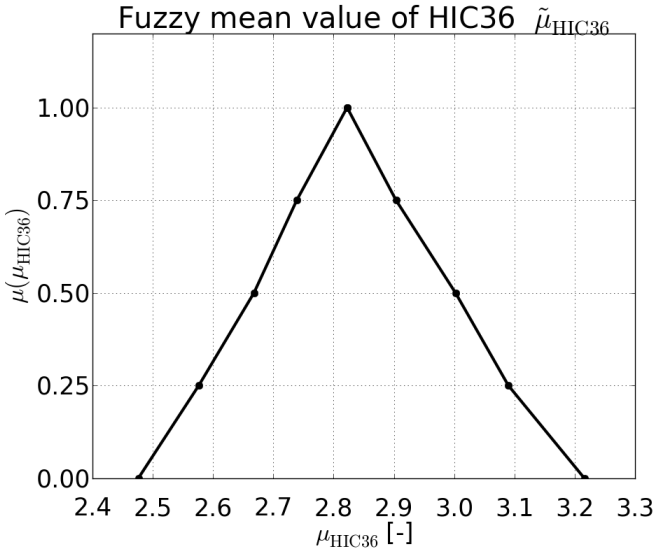


Figure 6.10: Fuzzy mean value of HIC36 $\tilde{\mu}_{\mathrm{HIC36}}$.

In Fig. 6.10, the fuzzy mean HIC36 value has an almost triangular membership function. This indicates that the relationship between the input variables and the mean HIC36 value is quite linear. This is because, variations of the input variables according to triangular membership functions yielded triangular membership of the result variable as well. This assumption is valid only if the number of stochastic iterations is sufficiently large, i.e. the stochastic results are unbiased.

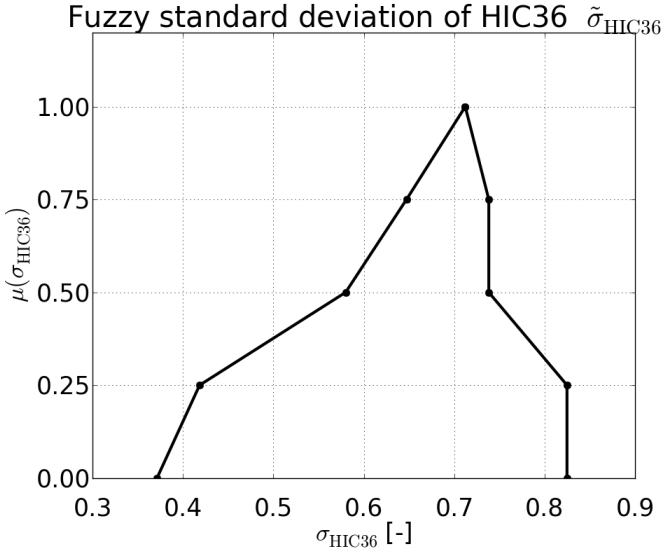


Figure 6.11: Fuzzy standard deviation of the HIC36 $\tilde{\sigma}_{\mathrm{HIC36}}$.

Finally, the membership function of the Fuzzy standard deviation of the HIC36, in Fig. 6.11, shows a wide bottom part and a narrow upper part, displaced to the right. It is a membership function that fairly differs from the triangular. This indicates that the relationship between the input variables

and the HIC36 value is non-linear. Because despite the fact that the mean HIC36 value has a linear relationship with the input variables, the scatter around the mean value (standard deviation) is not linearly explained by the variations in the input. The fact that this membership function is displaced to the right, indicates that the scatter (standard deviation) of the HIC36 value, is larger than expected. This holds, because symmetric (triangular) membership functions of the input variables, yielded a non-symmetric, shifted to the right (high values) standard deviation membership function.

## 6.6 STATISTICAL EVALUATION

In simulation results from explicit time integration of dynamical systems, numerical noise is often observed [18],[16]. In the present section, the results from the 100 original analyses are used to investigate how much of the resulting variations in the HIC36 values is coming from numerical noise [49]. For that reason, the statistical method of regression analysis in linear and in quadratic form is used to determine the so called *coefficient of determination* $\mathrm{R}^2$.

The standard regression analysis, is a statistical process for investigating the relationship between one dependent $(x)$ and one independent $(y)$ variable. More specifically, the constants of a specified mathematical model are estimated in such a way so that this model is capable of accurately predicting values of the independent variable $y$ given the dependent variable $x$. The estimation of the constants of the prediction model are estimated using the *least squares* approach. Due to the fact that the problem in the present study involves five uncertain input variables and one result variable, it is only possible to investigate the relationship of each input variable with the output variable separately. In such an approach, the total influence of the input variables to the result, can not be investigated due to the multiple dependency of the output variable. For that reason, a generalized approach of multivariate regression analysis is used [12].

### 6.6.1 Multivariate regression analysis

Assume a $p$-dimensional input vector $x_i = (x_{i1}, x_{i2}, ..., x_{ip})$ and that it is required to predict the real-valued output $Y_i$'s for $i = 1, ..., n$ where $n$ is the length of the sample. The linear regression model has the form

$$Y_i = \beta_0 + \sum_{j=1}^{p} x_{ij}\beta_j + \epsilon_i, \tag{6.3}$$

where $epsilon_i$ is a residual term. The $\beta_j$'s are unknown and are being estimated using the least squares criterion.

### 6.6.2 Least Squares

Given a set of training data set $((x_1 1, x_1 2, ..., x_1 p, y_1), (x_2 1, x_2 2, ..., x_2 p, y_2), ..., (x_n 1, x_n 2, ..., x_n p, y_n))$, the most popular estimation method for the calculation of the optimum $\beta_j$ coefficients is least squares. In this approach, the $\beta_j$'s are chosen according to the demand of minimization of the *residual sum of squares*

$$RSS(\boldsymbol{\beta}) = \sum_{i=1}^{n} \left( y_i - \beta_0 - \sum_{j=1}^{p} x_{ij}\beta_j \right). \tag{6.4}$$

It can be shown [33],[12] that the unique solution of the optimization problem of minimizing $RSS(\beta)$ in Eq. (6.4), is

$$\hat{\boldsymbol{\beta}} = (\mathbf{X}^T\mathbf{X})^{-1}\mathbf{X}^T\mathbf{y}, \tag{6.5}$$

where $\mathbf{X}$ is the *design* matrix

$$\mathbf{X} = \begin{pmatrix} 1 & x_{11} & \cdots & x_{1p} \\ \vdots & \vdots & \ddots & \vdots \\ 1 & x_{n1} & \cdots & x_{np} \end{pmatrix}, \text{ and } \mathbf{y} = \begin{pmatrix} y_1 \\ \vdots \\ y_n \end{pmatrix}.$$

The regression model can also be expressed in matrix form

$$\mathbf{y} = \mathbf{X}\boldsymbol{\beta} + \boldsymbol{\epsilon}, \tag{6.6}$$

where $\boldsymbol{\epsilon} = (\epsilon_0, ..., \epsilon_n)$ are unknown when $\mathbf{y}$ is to be predicted.

For the quadratic regression model, the design matrix has the form

$$\mathbf{X} = \begin{pmatrix} 1 & x_{11} & x_{11}^2 & \cdots & x_{1p} & x_{1p}^2 \\ \vdots & \vdots & \ddots & \vdots & & \\ 1 & x_{n1} & x_{n1}^2 & \cdots & x_{np} & x_{np}^2 \end{pmatrix}, \tag{6.7}$$

and the $\boldsymbol{\beta}$ vector has a length of $2p + 1$ [3]. In that case, the least squares solution of Eq. (6.5) provides generally acceptable estimates of the $\boldsymbol{\beta}$ vector, but for accuracy reasons more advance methods of generalized, non-linear least squares solutions are used in the present studies. More specifically, two methods are used that yielded the same results; these are the 'GLS' (Generalized Least Squares) library provided by the 'statsmodels' package of the Python programming language and the 'nls' (Non-linear Least Squares) library provided by the 'stats' package of the R language for statistical programming.

### 6.6.3 Coefficient of determination $\mathrm{R}^2$

We denote by $y_i^*$ the fitted values from the linear regression analysis

$$\mathbf{y}_i^* = \hat{\beta_0} + \sum_{j=1}^{p} x_{ij}\hat{\beta_j}. \tag{6.8}$$

The coefficient of determination is defined as

$$R^2 = Corr^2(y_i^*, y_i) = \frac{Cov^2(y_i^*, y_i)}{Var(y_i^*)Var(y_i)} \tag{6.9}$$

where $Corr(\cdot)$ is the *Pearson product-moment correlation coefficient*, $Var(\cdot)$ is the *variance* and

$$Cov(x, y) = \mathbf{E}[(x_i - \mathbf{E}[x])(y_i - \mathbf{E}[y])] \tag{6.10}$$

is the *covariance*, where $\mathbf{E}[\cdot]$ is the *expected value*. It can be shown [12] that

$$R^2 = \frac{Var(y_i) - Var(\hat{\epsilon_i})}{Var(y_i)}, \tag{6.11}$$

where $\hat{\epsilon_i} = y_i - y_i^*$ are the residuals from the regression. The numerator of Eq. (6.11) is called the *explained* variance and is equal to the difference between the *total* variance $Var(y_i)$ and the

[3] The $\boldsymbol{\beta}$ vector has a length of $p + 1$ in the linear regression formula.

*residual* variance $Var(\hat{\epsilon}_i)$. The coefficient of determination $R^2 \in [0, 1]$ is therefore interpreted as the proportion of variance that is explained by the investigated regression model.

For better understanding the most common definition of $\mathrm{R}^2$ for a standard 1+1 regression analysis, is provided in Eq. (6.12).

$$R^2 = 1 - \frac{SS_{res}}{SS_{tot}} = 1 - \frac{\sum_{i=1}^{n}(y_i - y_i^*)^2}{\sum_{i=1}^{n}(y_i - \mathbf{E}[y])^2} \tag{6.12}$$

The term $SS_{tot}$ represents the sum of the red squares in Fig. 6.12 left, while the term $SS_{res}$ represents the sum of the blue squares in Fig. 6.12 right. The formula in Eq. (6.12) does not necessarily provide the same results as the one in Eq. (6.11) in multi-dimensional regression analysis and is quoted only for better understanding of the significance of $\mathrm{R}^2$.

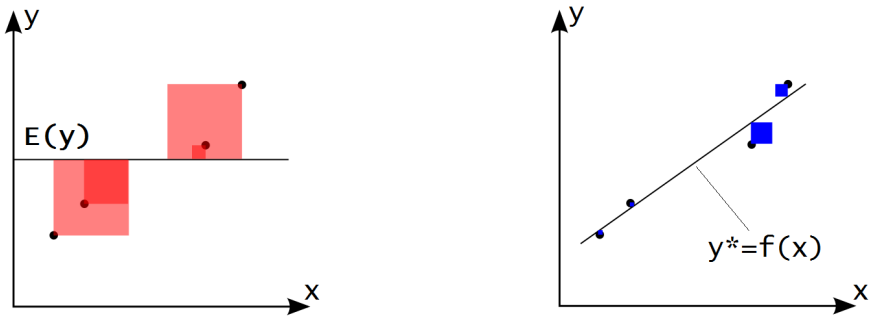


Figure 6.12: Graphical representation of the calculation of $\mathrm{R}^2$ for standard regression analysis. **Left**: The sum of the red squares represents the total variance of the result variable ($SS_{tot}$). **Right**: The sum of the blue squares represents the variance of the residual terms ($SS_{res}$) given the regression model $y^* = f(x)$.

As a result, if a mathematical model is found, that can fit the data with a large coefficient of determination $R^2 \approx 1$, means that the variations of the result variable can be explained almost completely by the identified correlations to the input variables. The smaller the coefficient of determination, the largest the part of the result variation that can not be explained by the regression model, linear or quadratic. In that case, highly non-linear correlations, clustering outliers [4] or a high amount of numerical noise exist [49].

### 6.6.4 Results

In the present study, coefficients of determination are calculated for the numerical model of the impact simulation and for the metamodel, using linear and quadratic regression analysis. For the calculation of $\mathrm{R}^2$ for the original model, the 100 simulation results are being used, while for the metamodel, 1000 Latin Hypercube (LHS) samples were generated and their result values were approximated by the metamodel. The results are summarized in Table 6.6.

[4] The term clustering outliers, refers to discrete observations of a result variable that are far from the range that the rest discrete observations belong. As a result, these values significantly influence the statistical measures because of their high distance from the sample averages. Such 'outliers' may be present due to non-linearities in the Finite Element model, and are not easily identifiable in high dimensional problems.

Table 6.6: Coefficients of determination of the impact simulation model and of the metamodel using multivariate regression analysis

| $R^2$ | Linear regression | Quadratic regression |
|---|---|---|
| Original model | 77.5 % | 87.1 % |
| Metamodel | 82.9 % | 87.9 % |

According to [49], in numerical models for which the coefficient of determination is larger than 80 %, the influence of numerical noise on the result variables is acceptable. As a result, the impact simulation numerical model, does not suffer from significant numerical noise because the variations in the result variable can be explained by the variations in the input variables with a degree of determination of 77.5 % for linear and 87.1 % for quadratic regression analysis.

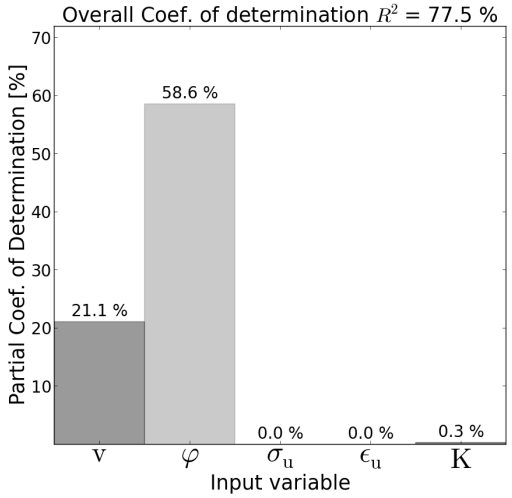


Figure 6.13: Linear regression analysis of the 100 original data.

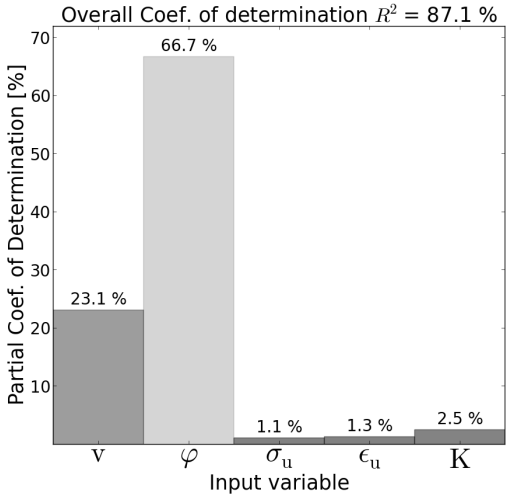


Figure 6.14: Quadratic regression analysis of the 100 original data.

The proportion of the unexplained variance $(1 - R^2)$, may result from three different sources, a) the chosen regression model (linear/quadratic) departs from the actual correlation patterns between the input variables and the result, b) presence of clustering outliers due to high non-linearities in the numerical model of the impact simulation and c) an amount of numerical noise always exists in CAE simulations. In any case, the unexplained variance $(1 - R^2)$, is small and thus none of these issues is significant.

The quality of the metamodel is possible to be assessed with the aid of coefficients of determination. The smaller the difference $\left|R^2{}_{MODEL} - R^2{}_{METAMODEL}\right|$, the higher the degree of accuracy of the metamodel in predicting result values and thus higher quality. It can be observed in Table 6.6, that the metamodel produces result values in a more linear manner than it should. On the other hand, in the quadratic regression case, the fact that a) the $R^2$ values are larger and b) the difference $\left|R^2{}_{MODEL} - R^2{}_{METAMODEL}\right|$ is significantly lower, proves that a) the original input data exhibit quadratic correlations to the result data and b) the quality of the metamodel is acceptable.

In addition to that, partial coefficients of determination are calculated for each input variable against the result variable (see Fig. 6.13-6.16). These coefficients have no significant meaning, because of the inter-correlations between the input variables, but they are comparable to each other and they can indicate which input variables influence the result the most. It is thus a measure of rela-

tive sensitivity of the result variable to each one of the input variables within the chosen variation intervals.

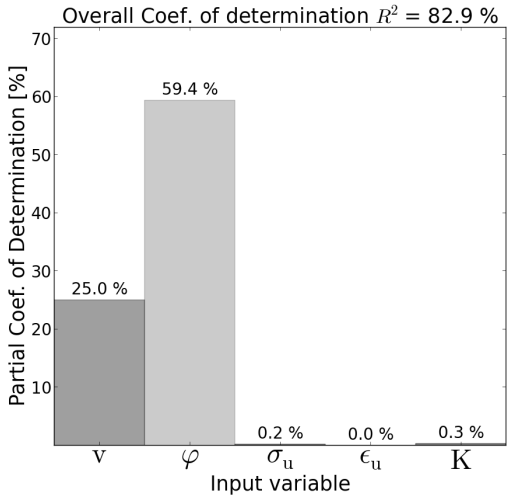


Figure 6.15: Linear regression analysis of the 1000 metamodel data.

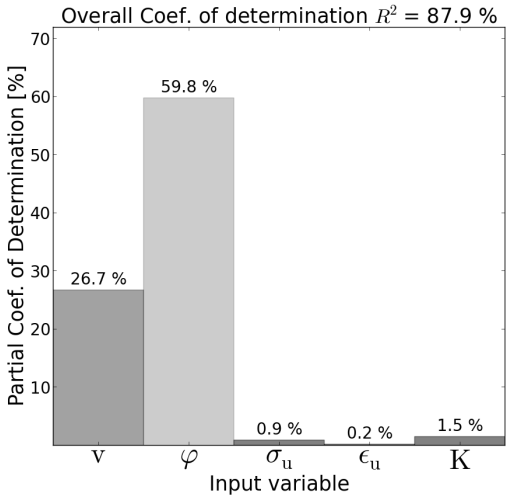


Figure 6.16: Quadratic regression analysis of the 1000 metamodel data.

In all the cases, it is evident that the impact angle and the impact speed are the most influential among the input variables. This is because first, they indicate the boundary conditions of the problem and they are thus very important and second, their variation intervals are significantly larger compared to the other three input variables. The variables ultimate stress and ultimate strain of the weld $\sigma_u$ and $\epsilon_u$, exhibit very low correlation to the result variable and they could been excluded from further uncertainty analyses with the same numerical model.

**General remarks on $\mathrm{R}^2$**

- The calculated $\mathrm{R}^2$ values, depend on the variation intervals of the input variables. If these specified intervals change, the partial and/or overall values of the coefficient of determination may change dramatically.
- The calculation of $\mathrm{R}^2$ is done using variances (see Eq. (6.11)). As a result, in the term $Var(\hat{\epsilon}) = (\hat{\epsilon_i} - \mathbf{E}(\hat{\epsilon}))^2$, the error measures are squared, and thus the influence of 'outlying' (outliers) effects are enhanced.
- A properly defined measure of determination, similar to $\mathrm{R}^2$, may be used to calculate the error of the metamodel during it's developing process.
- It is possible to perform an initial variation analysis with a large number of input variables, within properly specified intervals, and calculate partial coefficients of determination. Subsequently, the main uncertainty analysis can be performed containing the most influential variables only.

# 7 CONCLUSIONS

Computer aided car crash simulations, are widely used in the vehicle design procedure in order to reduce the total development cost. After several years of advancement such simulations have reached a high degree of accuracy and numerical efficiency. In fact, they are so efficient, that with the aid a metamodel, it is possible to be used as the deterministic solution in computationally expensive uncertainty analyses.

In the present thesis, a vertical traffic road sign support structure was numerically evaluated under consideration of passive safety requirements according to [2]. Using uncertainty analysis, it was found that there is no risk for occupant injury in the case that a small vehicle impacts against such a structure. The quality of the solution has been verified using different measures and approaches, such as the time-history of the energy balance, the integration of acceleration compared to the velocities and coefficients of determination derived from the results of the variation analysis.

**Passive safety**

The sign support structure, is a passively safe non-energy absorbing structure. An interesting observation about such structures, that they are intended to fail when involved in crashes against vehicles, is that their safety depends upon their failure. Based on this observation, it can be stated that the permissible and non-permissible design spaces are reversed compared to ordinary structural safety assessments. More specifically, the permissible design space, in view of occupant safety, is defined as the space within which the structure fails according to [2]. In an ordinary structural safety application on the other hand, the permissible design space is usually the space within which the structure does not fail.

This special characteristic of passively safe non-energy absorbing support structures, is important in the choice of the material parameters. In [5], it is mentioned, that the ductility properties of structural steel, is expressed through the ultimate strain value $\epsilon_u$, for which, a value of $15\ \%$ is proposed. This value is lower than experimental values of ultimate strain of structural steel (see Fig. 3.11) and especially for low strength steel such as the S235JR used in the present studies. This underestimation, indicates that the assumed ductility is lower than the real value. As a result, when assessing the stability of a structure, this is not a problem, because if the structure is checked for underestimated ductility, means that it is safer than in reality. In passively safe non-energy absorbing structures though, an underestimation of ductility, is almost always translated to underestimation of the injury indices, which may result to misleading results concerning the occupant safety.

**Numerical model and analysis**

Concerning the numerical model of the structure, presented in section 3.1, it was developed and meshed in detail (see Fig. 3.2) in order to achieve accuracy. A simplified approach using elastic springs was introduced to describe the behaviour of the bolted connection of the supporting plates to the ground (see Fig. 3.5). For the determination of the elastic constant of the springs, a numerical experiment has been employed (see section 3.1.2). The use of such numerical experiments was

proved very useful, because they can provide estimations of unknown model parameters that lack of physical significance.

In addition, the supported sign was introduced in the numerical model (see Fig. 3.7), in order to account for the additional stiffness it assigns to the whole structure. Valid assumptions and considerations have been made for the different connections within the numerical model of the structure (see Table 3.2).

Numerical efficiency, is a key aspect in computer simulations of vehicle impacts. Such simulations, require a small analysis time step in order to calculate the rapid deformations during the crash accurately. This requirement, makes the employment of an explicit solution scheme very suitable. This is because explicit time integration, is performed in very small time steps anyway, and is much more efficient than an implicit time integration process with the same time step.

The small time step of the explicit analysis, is suitable for the calculations concerning the various types of contacts used within the simulation (see Table 4.1). In the treatment of the contact, in each time step, possible penetrations are forced to elimination by applied normal forces. As a result, if the time step is not small enough, these penetrations will be large and the results will lack accuracy. The implementation of an explicit structural analysis algorithm is summarized in section 4.4.

For the modelling of the structure, shell elements were used, and for their numerical representation, the Hughes-Liu shell element was chosen. This shell element type, proved to be very efficient in the single integration point mode. As a result an impact simulation involving the developed numerical model of the structure in conjunction with the explicit solution method, could be performed in reasonable time.

**Results and verification**

The results of the standard test according to [2], are summarized in the test report in section 5.1. In Fig. 5.2-5.5, the motion of the dummy and the fact that it's head does not comes in contact with the airbag, indicate that the impact was not severe for none of the speed classes. The low severity of the impact was proved from the acceleration measurements and the low values of the severity indices and the injury criteria in Fig. 5.6.

The acceleration measurements of the head, are smooth relatively to the accelerations of the centre of mass of the car, where a high frequency vibration interferes in the results. This vibration has an amplitude 100 times larger than the physical acceleration values, and thus it covers completely all the useful information concerning the acceleration of the vehicle. This problem has been confronted using digital filters (see section 5.3) of different cut-off frequencies for different purposes. In addition to this, another important aspect in acceleration measurement, is the sampling period. If the sampling period is not small enough, the acceleration measurements are incorrect (see Fig. 5.4.2) because the influence of the high frequency vibrations is non-symmetric. This effect is referred to as aliasing, and in order to prevent it, a sufficiently small sampling period of $0.005\ \mathrm{ms}$ was used.

The quality of the numerical solution has been verified by the time-history of the energy balance of the system, shown in Fig. 5.8. The energy balance revealed almost zero hourglass energy which indicates high quality of the solution. An increase at the total energy, for the low speed classes, is explained by the use of single surface contact types, as mentioned in [36].

Moreover, an impact-against-rigid-wall experiment, depicted in Fig. 5.13, verified that the HIC calculation algorithm is correct, because the calculated HIC36 value was close to the maximum affordable by the human body value. This means that the occupant was close to get injured but he didn't, a

reasonable outcome of a crash with $50\ \mathrm{km/h}$ including seatbelt and airbag. In addition to this, these results were compared with acceleration recordings of a real $56\ \mathrm{km/h}$ impact test and found to be fairly similar when both filtered with a low pass digital filter of class CFC_180.

**Uncertainty analysis**

The uncertainty analysis, was performed in order to account for some uncertain variables (see Table 6.1) of the problem and extract overall information including different crash scenarios. The assumed uncertain variables, are the boundary conditions impact speed and impact angle, the failure parameters ultimate stress and ultimate strain of the base weld (see section 3.1.2), as well as the elastic stiffness of the springs, used instead of bolted connection of the plates (see section 3.1.2). The first two, and especially the impact angle, found to be the most influential among the uncertain variables. As the critical response variable, the HIC36 was chosen.

Uncertain variables the values of which vary under constant reproduction conditions, are characterized by variability, which is an uncertainty characteristic of aleatoric type. If the available data about an uncertain variable are described by incompleteness and/or impreciseness, then this is uncertainty of epistemic type. After resent advances in engineering uncertainty analysis, presented in [40], [42] and [22], it has been identified, that parameters associated with aleatoric uncertainty are best described using random variables and those associated with epistemic uncertainty using fuzzy variables. In addition to this, generalized models have been developed [22], e.g. fuzzy random variable, that account for aleatoric and epistemic uncertainty type simultaneously.

For the computational realization of the fuzzy analysis a global optimization concept is selected as $\alpha$-level optimization in conjunction with a modified evolution strategy (see section 6.4). For the analysis of problems involving uncertain parameters described by different uncertainty models, the uncertainty analysis tool 'Winfuz', that is capable of performing fuzzy random analysis, was used. The results from fuzzy random analysis are probabilistic measures, e.g. probability of failure, mean value etc., with fuzzy interpretation.

Due to the fact that the calculated HIC36 values were much smaller than the limit value of 1000, a smaller limit value of 5.3 has been adopted in order to present the procedure of the fuzzy random analysis. Based on this limit value, the non-permissible design subspace has been calculated and depicted in a parallel coordinate plot in Fig. 6.2. Moreover, the fuzzy probability of failure, the fuzzy mean HIC36 value and the fuzzy standard deviation of HIC36 have been calculated and presented in Fig. 6.9-6.11. Based on these results, a linear pattern between input parameters and fuzzy mean HIC36 value has been identified (see section 6.5), due to the fact that triangular membership functions of the input parameters, resulted in an also triangular membership function of the mean HIC36 value.

Numerical efficiency for the realization of the uncertainty analysis, has been achieved with the aid of a metamodel. In section 6.2, it is described the usage of a metamodel, that produces result values, based on sets of input parameters and their functional behaviour identified by a number of Finite Element solutions of the problem.

Finally, in section 6.6, the statistical coefficient of determination $\mathrm{R}^2$ has been used to assess the quality of the numerical model and solution, as well as the quality of the metamodel. The calculated coefficients of determination using linear and quadratic regression analysis, reached high values $\approx 87\ \%$ for the original model, indicating that numerical noise does not influence the results dramatically [49]. Moreover, the fact that the coefficient of determination of the metamodel, was very close to the value calculated for the original model, indicates the high quality of the metamodel, in accurately producing result values.

**Future work**

From the study in section 6.6, it has been identified the possibility of using partial coefficients of determination as a relative measure of influence of an uncertain variable (given the variation interval), on the result variable. As a result, an initial variation analysis involving a large number of variables can be performed, identify the most influential ones, and include only those in the main, subsequent uncertainty analysis. This approach, deserves further research, because it provides a computationally efficient way to identify the relative correlation between each input variable to the result variable. It should be noted that the influence of an input variable to the result, highly depends on the variation interval which should be chosen carefully.

In the present study, it has been found that high values of HIC36 appear in simulations with low impact speeds after a time of $250\ \mathrm{ms}$ (see Fig. 5.6 class $35\ \mathrm{km/h}$). In further studies in passive safety of non-energy absorbing structures, simulations with impact speeds lower than $35\ \mathrm{km/h}$ and duration more than $300\ \mathrm{ms}$ should be studied.

Moreover, for the improvement of vehicle impact simulations, a more sophisticated approach to treat the element failure should be employed. As described in section 3.1.6, when an element has failed, according to the applied failure criterion, then it is deleted from the analysis. This simplified approach, introduces some computational error in the calculation. In addition, comparison between results from numerical impact tests with results from real crash tests, can be very helpful in improving the quality of the simulations.

In order to describe more realistically the problem of a car impacting against a sign support structure, more attributes of the physical problem should be taken into account. The investigation of different car models, different foundation types and the possible presence of surrounding objects that may influence the car impact, like trees, small hills etc., can provide a more comprehensive approach of the safety problem.

In addition, the use of higher material ductility (ultimate strain) should be investigated, due to the special characteristic of passively safe non-energy absorbing structures, where the permissible design space is characterized by structural failure, in contrast to ordinary structural safety applications.

# ACKNOWLEDGEMENTS

I would like to thank Dipl.-Ing. Marco Götz for his interest, help and useful recommendations, Prof. Dr.-Ing. Wolfgang Graf, Prof. Dr.-Ing. habil. Michael Kaliske, as well as my close friend Evi for her support.

Moreover, I would like to acknowledge the National Crash Analysis Center (NCAC), U.S.A., which provided the numerical model of the car, and DYNAmore GmbH, Germany, which provided the numerical model of the dummy.

# Appendices

# A APPENDIX

## A.1 PICTURES OF A TYPICAL STRUCTURE

Figure A.1: Pictures of a typical structure **Left**: typical traffic sign support structure. **Right**: details. Upper: rigid, concrete foundation. Middle: base plate bolted on the foundation. Down: connection between truss and sign.

## A.2 EN 12767: PRODUCT FAMILIES

*"The largest size of any proposed product family shall be tested first, at the speed class selected and at low speed.*

*NOTE Usually the largest size will have the greatest resistance to load, in terms of bending moment resistance at ground level.*

*Depending on the results of these tests, further tests shall be carried out as follows:*

a) *If the tested item complies with the NE category, no further tests are required. A product family may be declared for the tested item, and all smaller members of the family for which technical data has been provided, with the same speed class, energy absorption category, and occupant safety level as the tested item. Due to risk of penetration of the windscreen of an impacting car, the untested reduced minimum height shall not be lower than 2,0 m. Lower installations shall be subject to a specific test.*

b) *If the tested item complies with the HE or LE category, further testing shall be carried out on the smallest member of the proposed product family, at the selected speed class only.*

   1) *If the smallest item when tested fulfils the same energy absorption category and occupant safety level, a product family may be declared including the tested items and all intermediate members of the product family for which the technical data has been provided. All the product family shall be declared to have the same speed class, energy absorption level, and occupant safety level.*
   2) *If the smallest item when tested at the same impact speed fulfils the same energy absorption category and a higher occupant safety level, a product family may be declared for all intermediate members of the proposed product family for which the technical data has been provided. All the product family shall be declared to have the same speed class, energy absorption category and occupant safety level as the largest item, except that for the smallest tested item the actual occupant safety level achieved in the test of that item shall be declared.*
   3) *If the smallest item when tested provides a different energy absorption category (HE or LE) and/or a lower occupant safety level to that achieved by the largest item, a product family shall not be declared."*

## A.3 REAL IMPACT TEST: TEST REPORT

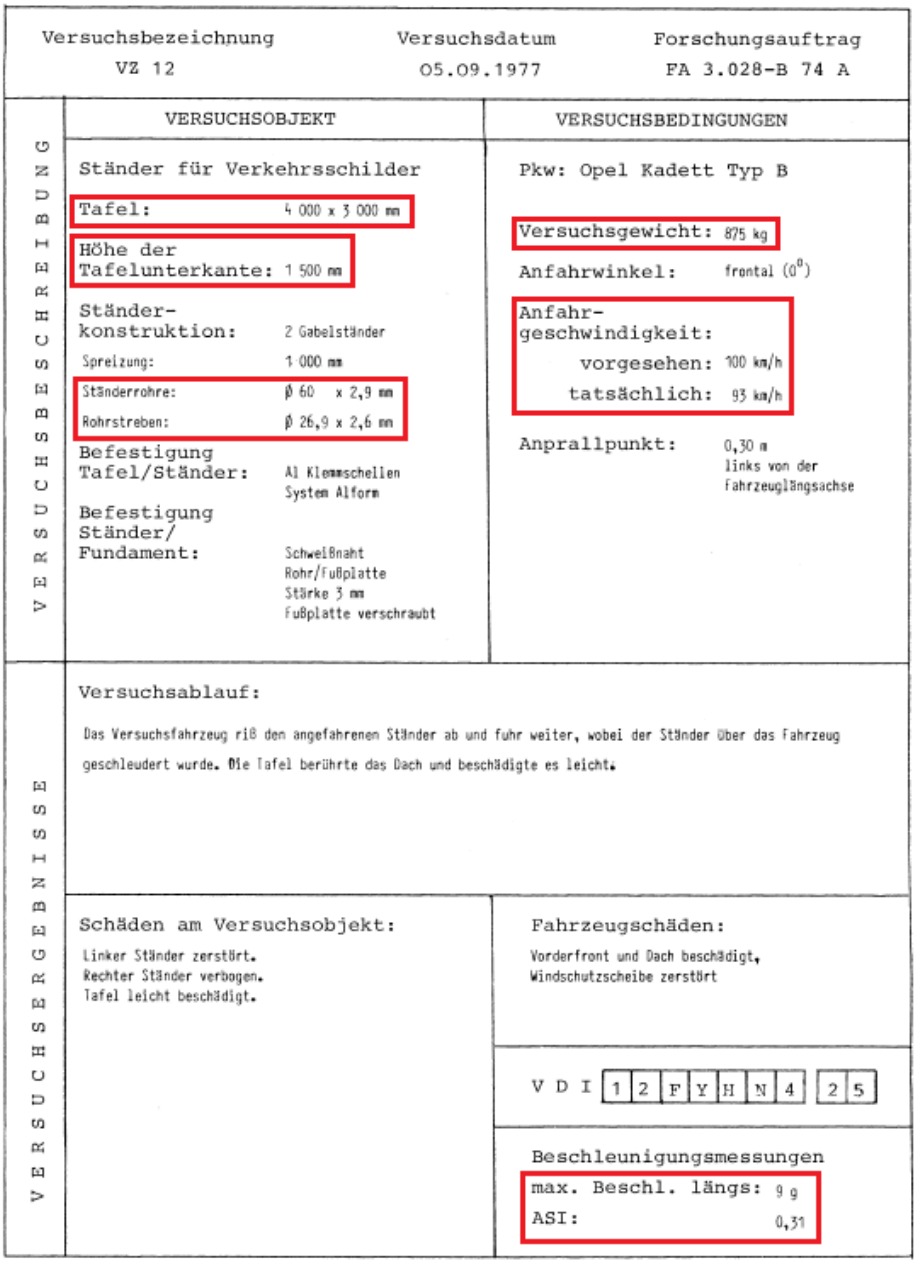

| Versuchsbezeichnung | Versuchsdatum | Forschungsauftrag |
|---|---|---|
| VZ 12 | 05.09.1977 | FA 3.028-B 74 A |

**VERSUCHSBESCHREIBUNG**

| VERSUCHSOBJEKT | | VERSUCHSBEDINGUNGEN | |
|---|---|---|---|
| Ständer für Verkehrsschilder | | Pkw: Opel Kadett Typ B | |
| Tafel: | 4 000 x 3 000 mm | Versuchsgewicht: | 875 kg |
| Höhe der Tafelunterkante: | 1 500 mm | Anfahrwinkel: | frontal (0°) |
| Ständer-konstruktion: | 2 Gabelständer | Anfahr-geschwindigkeit: | |
| Spreizung: | 1 000 mm | vorgesehen: | 100 km/h |
| Ständerrohre: | ϕ 60 x 2,9 mm | tatsächlich: | 93 km/h |
| Rohrstreben: | ϕ 26,9 x 2,6 mm | Anprallpunkt: | 0,30 m links von der Fahrzeuglängsachse |
| Befestigung Tafel/Ständer: | Al Klemmschellen System Alform | | |
| Befestigung Ständer/ Fundament: | Schweißnaht Rohr/Fußplatte Stärke 3 mm Fußplatte verschraubt | | |

**VERSUCHSERGEBNISSE**

Versuchsablauf:

Das Versuchsfahrzeug riß den angefahrenen Ständer ab und fuhr weiter, wobei der Ständer über das Fahrzeug geschleudert wurde. Die Tafel berührte das Dach und beschädigte es leicht.

Schäden am Versuchsobjekt:

Linker Ständer zerstört.
Rechter Ständer verbogen.
Tafel leicht beschädigt.

Fahrzeugschäden:

Vorderfront und Dach beschädigt,
Windschutzscheibe zerstört

VDI 12 FYHN 4 25

Beschleunigungsmessungen

| | |
|---|---|
| max. Beschl. längs: | 9 g |
| ASI: | 0,31 |

Figure A.2: Test report of real impact test.

# B APPENDIX

## B.1 MATHEMATICAL DEFINITIONS

### B.1.1 Random variable

**Definition B.1.** ***random variable*** *Given an experiment specified by the space $S \subseteq \mathbb{R}$, a random variable $\boldsymbol{X}$ is a process of assigning a number $\boldsymbol{X}(\zeta)$ to every outcome $\zeta \in S$ of the experiment. The resulting function must satisfy the following two conditions but is otherwise arbitrary:*

1. *The set $\{\boldsymbol{X} \leq x\}$ is an event for every $x$.*
2. *The probabilities of the events $\{\boldsymbol{X} = \infty\}$ and $\{\boldsymbol{X} = -\infty\}$ equal 0:*
   *.* $P\{\boldsymbol{X} = \infty\} = 0 \qquad P\{\boldsymbol{X} = -\infty\} = 0$

For a random variable, it may be defined, *cumulative distribution function* (CDF)

$$F(x) = P\{\mathbf{X} \leq x\}, \tag{B.1}$$

which is the probability that the random variable $\mathbf{X}$ will be less or equal to the value $x$, and *probability density function* (PDF)

$$f(x) = \frac{dF(x)}{dx}. \tag{B.2}$$

### B.1.2 Fuzzy set

In classical set theory the membership of elements in relation to a set is assessed in binary terms according to a crisp condition [40]. This means that an element either belongs or does not belong to the set, the boundary of the set is crisp, and the set is called *crisp set*, see Fig. B.1.2.

As a further development of classical set theory, fuzzy set theory permits the gradual assessment of the membership of elements in relation to a set, see Fig B.1.2. This is described with the aid of a membership function. A definition of a fuzzy set, is derived from [40].

**Definition B.2.** ***fuzzy set*** *If $\boldsymbol{X}$ represents a fundamental set and $x$ are the elements of this set, to be assessed according to an uncertain postulation and assigned to a subset $A$ of $\boldsymbol{X}$, the set*

$$\tilde{A} = \{(x, \mu_A(x)) | x \in \boldsymbol{X}\} \qquad \mu_A(x) \geq 0 \; \forall x \in \boldsymbol{X} \tag{B.3}$$

*is referred to as fuzzy set on $\boldsymbol{X}$. $\mu_A(x)$ is the membership function (characteristic function) of the fuzzy set $\tilde{A}$. The fuzzy set $\tilde{A}$ is also referred to as uncertain set $\tilde{A}$ and as fuzzy variable or fuzzy value $\tilde{x}$.*

Fuzzy variables may be utilized to describe the imprecision and/or incompleteness of structural parameters directly, as well as to specify the parameters of fuzzy random variables. The membership function, usually is normalized so that, has a peak value of 1.

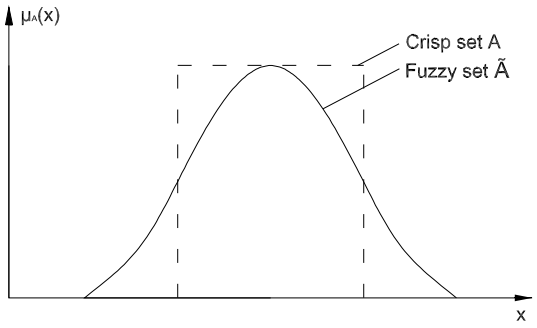


Figure B.1: Comparison of crisp set and fuzzy set.

### B.1.3 Fuzzy random variable

**Definition B.3.** ***fuzzy random variable*** *In accordance with probability theory, the space of the random elementary events $\Omega$ is introduced. Instead of a real realization, a fuzzy realization of the form $\tilde{x}(\omega) = \tilde{x}$ is now assigned to each elementary event $\omega \in \Omega$. Where $\tilde{x}$ is an element of the set $\boldsymbol{F}(\mathbb{R})$ of all fuzzy variables on $\mathbb{R}$. Accordingly from the definition of a fuzzy variable, a fuzzy random variable $\tilde{X}$ is a fuzzy result of the mapping given by*

$$\tilde{X} : \Omega \mapsto \boldsymbol{F}(\mathbb{R}) \tag{B.4}$$

*[42],[48].*

Based on this formal definition, a fuzzy random variable is described by its *fuzzy cumulative distribution function* (fuzzy CDF) $\tilde{F}(x)$. The function $\tilde{F}(x)$ is defined as the set of all real-valued cumulative distribution functions $F(x)$ which are gradually assessed by the membership $\mu_F(F(x))$. $F(x)$ is the CDF of the random variable $X$ and as a result, each realization $x_i$ of $X$ is assigned to a fuzzy (functional) value $\tilde{F}(x_i)$ (see Fig. B.1.3). Thus, $\tilde{F}(x)$ is a *fuzzy function*, definitions of which can be found in [42] and in [48]. It may also be defined accordingly, a *fuzzy probability density function*

$$\tilde{f}(x) = \{(f(x), \mu_f(f(x)))|f \in \mathbf{f}\} \qquad \mu_f(f(x)) \geq 0 \; \forall f \in \mathbf{f}. \tag{B.5}$$

Where **f** represents the set of all probability density functions defined on $X$.

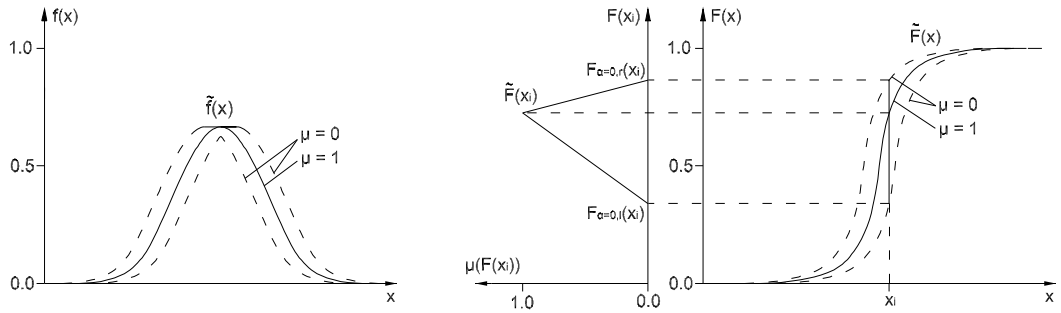


Figure B.2: Fuzzy probability density and fuzzy cumulative distribution function.

In engineering structural problems, a stochastically and non-stochastically uncertain parameter, may by assumed as an elementary event $\omega$ in the space of the random elementary events $\Omega$. As a result, the modelling of such an uncertain parameter as a fuzzy random variable, may be understood by the following simplified approach. Realizations of the given uncertain parameter, are distributed according to a specific probability density function (or cumulative distribution function) the parameters of which, e.g. the mean $\mu$ and the standard deviation $\sigma$ are fuzzy variables, $\tilde{\mu}$ and $\tilde{\sigma}$.

## B.2 FILTERING

### B.2.1 Butterworth 4-pole phaseless digital filter

This filter can be found in [31], [7] and [4].

A difference equation is used for filtering a sequence of data samples. The difference equation is in the time domain has the form shown in Eq. (B.6).

$$Y[t] = a_0 X[t] + a_1 X[t-1] + a_2 X[t-2] + b_1 Y[t-1] + b_2 Y[t-2] \tag{B.6}$$

Where $X[t]$ is the input data stream, $Y[t]$ is the filtered output data stream, $a_0$, $a_1$, $a_2$, $b_1$ and $b_2$ are constants dependent on the CFC as shown below.

Evaluation of coefficients:

$$\begin{aligned}
S &= \text{sampling rate in } \ 1/\mathrm{s} \\
T &= 1/S = \text{sampling period in seconds ( s)} \\
w_d &= 2 \cdot \pi \cdot CFC \cdot 2.0775 \\
w_a &= \frac{\sin\left(w_d \cdot \frac{T}{2}\right)}{\cos\left(w_d \cdot \frac{T}{2}\right)} \\
a_0 &= \frac{w_a^2}{\left(1 + \sqrt{2} \cdot w_a + w_a^2\right)} \\
a_1 &= 2 \cdot a_0 \\
a_2 &= a_0 \\
b_1 &= \frac{-2 \cdot \left(w_a^2 - 1\right)}{\left(1 + \sqrt{2} \cdot w_a + w_a^2\right)} \\
b_2 &= \frac{\left(-1 + \sqrt{2} \cdot w_a - w_a^2\right)}{\left(1 + \sqrt{2} \cdot w_a + w_a^2\right)}
\end{aligned} \tag{B.7}$$

Equation (B.6) is a two-pole filter. To perform a four -pole phaseless filter, data shall pass through the filter twice. Passing data through the filter forward and then backwards will not phase shift the data.

Start-up of the digital filter yields the same response as switching a signal into the input of an analog filter. The digital filter algorithm sees non-zero initial data as a step function, and it responds with a typical under-damped second-order response. If the data set to be filtered contains sufficient pre-event and post-event data, then the initial conditions may be ignored because the filter response to the initial step input will have damped out before the event begins. A minimum of 500 ms of pre-contact data and 500 ms of post-event data shall be recorded for that purpose [4]. In the present thesis, these pre- and post-event data have not been recorded.

### B.2.2 Python function for applying a 4-pole Butterworth digital filter

```
import numpy
import math

def filtering(CFC, a, dt):
# ------------------------------------------------------------------------
# FILTERING FUNCTION
# ------------------------------------------------------------------------
# CFC  = Filter class, e.g. 180, 1000 etc.
# a    = raw acceleration data in g
# dt   = sampling period in ms
# ------------------------------------------------------------------------
# Returns af = filtered accelerations
# ------------------------------------------------------------------------

    # initialization
    SR = dt * 1e-3      # sampling rate in seconds
    NOS = len(a[:,3])

    NOAP = int(0.01/SR)
    NOAP = min(max(NOAP,100), (NOS - 1) )
    ILP = NOS + 2*NOAP - 1

    LFT = NOS + 2*NOAP
    FT = numpy.zeros(4 * LFT).reshape((LFT, 4))

    for i in range(NOAP, (NOAP + NOS)):
        FT[i][0:3] = a[i-NOAP][0:3]

    for i in range(0, NOAP):
        FT[NOAP-i-1][0:3] = 2*a[0][0:3] - a[i+1][0:3]
        FT[NOS+NOAP+i][0:3] = 2*a[NOS-1][0:3] - a[NOS-i-2][0:3]

    # coefficients
    wd = 2 * math.pi * CFC * 2.0775
    wa = math.tan(wd * SR / 2)
    a0 = wa ** 2 / (1 + math.sqrt(2) * wa + wa ** 2)
    a1 = 2 * a0
    a2 = a0
    b1 = -2 * (wa ** 2 - 1) / (1 + math.sqrt(2) * wa + wa ** 2)
    b2 = (-1 + math.sqrt(2) * wa - wa ** 2)/ \
         (1 + math.sqrt(2) * wa + wa ** 2)


    # filter forward
    y1 = numpy.array([0.0, 0.0, 0.0])
    for i in range(0, 10):
        y1[0:3] = y1[0:3] + FT[i][0:3]
```

```
48
49      y1 = y1/10.0
50      x2 = numpy.array([0.0, 0.0, 0.0])
51      x1 = FT[0][0:3]
52      x0 = FT[1][0:3]
53      FT[0][0:3] = y1[0:3]
54      FT[1][0:3] = y1[0:3]
55      for i in range(2, ILP+1):
56          x2 = x1
57          x1 = x0
58          x0 = FT[i][0:3]
59          FT[i][0:3] = a0 * x0 + a1 * x1 + a2 * x2 + \
60                       b1 * FT[i - 1][0:3] + b2 * FT[i - 2][0:3]
61
62      # filter backward
63      y1 = numpy.array([0.0, 0.0, 0.0])
64      for i in range(ILP, ILP-9-1, -1):
65          y1 = y1 + FT[i][0:3]
66
67      y1 = y1/10.0
68      x2 = numpy.array([0.0, 0.0, 0.0])
69      x1 = FT[ILP][0:3]
70      x0 = FT[ILP-1][0:3]
71      FT[ILP][0:3] = y1
72      FT[ILP-1][0:3] = y1
73      for i in range(ILP-2, -1, -1):
74          x2 = x1
75          x1 = x0
76          x0 = FT[i][0:3]
77          FT[i][0:3] = a0 * x0 + a1 * x1 + a2 * x2 + \
78                       b1 * FT[i + 1][0:3] + b2 * FT[i + 2][0:3]
79          FT[i][3] = math.sqrt(FT[i][0] ** 2 + FT[i][1] ** 2 + FT[i][2] ** 2)
80
81      af = numpy.zeros(4 * NOS).reshape((NOS, 4))
82      for i in range(NOAP, (NOAP+NOS)):
83          af[i-NOAP][0:4] = FT[i][0:4]
84
85      return af
```

## B.3 INJURY CRITERIA

### B.3.1 Python function for the HIC calculation

```
1  import numpy
2
3  def Calc_HIC(interval, a, dt, tend):
4  # ------------------------------------------------------------------------
5  # HIC
6  # ------------------------------------------------------------------------
7  # interval in ms, e.g. 36, 15
8  # a    = CFC_1000 filtered accelerations in g
9  # dt   = sampling period in ms
10 # tend = termination time in ms
11 # ------------------------------------------------------------------------
12 # Returns HIC = [HIC value, interval lower bound, interval upper bound]
13 # ------------------------------------------------------------------------
14
```

```
    # Integration of accelerations (in seconds)
    a_intgr = a*dt*0.001

    # Reduction of the array of integrated accelerations
    aver = 0.5/dt
    redused_at = numpy.zeros(1 * tend/0.5).reshape((tend/0.5, 1))
    for i in range(1, 2*tend):
        rox1 = aver*(i-1)
        rox2 = aver*i
        redused_at[i] = sum(a_intgr[rox1:rox2])

    rng = int(tend/0.5)

    HIC = [0, 0, 0, 0]
    u = 0
    hrange = int(interval/0.5)
    for i in range(0, rng - hrange):
        for j in range(2, hrange+1):
            i1 = i
            i2 = i + j

            s = sum(redused_at[i1:i2])

            u = ( (s/(0.0005*(j-1)))  ** 2.5 ) * (0.0005*(j-1))

            if u > HIC[0]:
                HIC = [u, i1, i2]

    return HIC
```

### B.3.2 Python function for the NIC calculation

```
import numpy

def Calc_NIC(anf, ahf, dt, n, g):
# ------------------------------------------------------------------------
# NIC
# ------------------------------------------------------------------------
# anf  = CFC_180 filtered accelerations of the neck in g
# ahf  = CFC_180 filtered accelerations of the head center of mass in g
# dt   = sampling period in ms
# n    = number of samples
# g    = acceleration of gravity in m/s**2
# ------------------------------------------------------------------------
# Returns NIC value and index of NIC value
# ------------------------------------------------------------------------

    dt = dt * 1e-3 #  seconds
    anf = anf/g    #  meters seconds
    ahf = ahf/g

    NIC = numpy.zeros(n).reshape((n, 1))
    vrel = numpy.zeros(n - 1).reshape((n - 1, 1))
    arel = numpy.zeros(n).reshape((n, 1))

    for i in range(1, n - 1):
        arel[i] = anf[i][3] - ahf[i][3]
        vrel[i] = vrel[i-1] + arel[i] * dt
        NIC[i] = 0.2 * arel[i] + vrel[i] ** 2
```

```
28
29      maxNIC = max(NIC)
30      ind_maxNIC = numpy.argmax(NIC)
31
32      return maxNIC, ind_maxNIC
```

## B.4 IMPACT SEVERITY INDICES

### B.4.1 Python function for the ASI calculation

```
1  import numpy
2
3  def Calc_ASI(acf):
4  # ------------------------------------------------------------------------
5  # ASI
6  # ------------------------------------------------------------------------
7  # acf  = CFC_180 filtered accelerations of the car center of mass in g
8  # ------------------------------------------------------------------------
9  # Returns ASI = vector of ASI values for all time steps
10 # ------------------------------------------------------------------------
11
12      n = len(acf[:,0])
13      ASI = numpy.zeros(n).reshape((n, 1))
14      for i in range(0, n):
15          ASI[i] = ((acf[i][0] / 12) ** 2 + (acf[i][1] / 9) ** 2 + \
16                    (acf[i][2] / 10) ** 2) ** 0.5
17
18      return ASI
```

### B.4.2 Python function for the THIV calculation

```
1  import numpy
2  import math
3
4  def Calc_THIV(w, vc, tw, dt, tend):
5  # ------------------------------------------------------------------------
6  # THIV
7  # ------------------------------------------------------------------------
8  # w    = yaw rate (z rotational velocity) in rad/s
9  # vc   = raw velocity data of the car center of mass in m/s
10 # tw   = vector of time values for each step in ms
11 # dt   = sampling period in ms
12 # tend = termination time in ms
13 # ------------------------------------------------------------------------
14 # Returns NIC value and index of NIC value
15 # ------------------------------------------------------------------------
16
17      n = int(tend / dt + 1)
18
19      tsec = tw * 1e-3
20
21      for i in range(0, len(tw)-1):
22          w[i][1] = w[i][0] * ( tsec[i+1] - tsec[i] )
23
24
25      XC = numpy.zeros(2 * n).reshape((n, 2))
```

```
    YC = numpy.zeros(2 * n).reshape((n, 2))

    for i in range(0, len(tw)-1):
        XC[i][1] = vc[i][0] - vc[0][0]
        YC[i][1] = vc[i][1] - vc[0][1]

        XC[i][0] = XC[i][1] * ( tsec[i+1] - tsec[i] )
        YC[i][0] = YC[i][1] * ( tsec[i+1] - tsec[i] )

    x0 = 0.646
    y0 = 0.3305
    Dx = 0.6
    Dy = 0.3

    xb = numpy.zeros(2 * n).reshape((n, 2))
    yb = numpy.zeros(2 * n).reshape((n, 2))

    for i in range(0, len(tw)-1):
        xb[i][0] =  (x0 - XC[i][0]) * math.cos(w[i][0]) \
                   +(y0 - YC[i][0]) * math.sin(w[i][0])
        yb[i][0] = -(x0 - XC[i][0]) * math.sin(w[i][0]) \
                   +(y0 - YC[i][0]) * math.cos(w[i][0])

        xb[i][1] = -XC[i][1] * math.cos(w[i][0]) \
                   -YC[i][1] * math.sin(w[i][0]) + yb[i][0] * w[i][1]
        yb[i][1] =  XC[i][1] * math.sin(w[i][0]) \
                   -YC[i][1] * math.cos(w[i][0]) - xb[i][0] * w[i][1]

    e1 = numpy.zeros(n-1).reshape((n-1, 1))
    e2 = numpy.zeros(n-1).reshape((n-1, 1))
    e3 = numpy.zeros(n-1).reshape((n-1, 1))
    for i in range(0, len(tw)-1):
        e1[i] = abs(xb[i][0] - Dx - x0)
        e2[i] = abs(yb[i][0] - Dy - y0)
        e3[i] = abs(yb[i][0] + Dy - y0)


    ind_e1 = numpy.argmin(e1)
    ind_e2 = numpy.argmin(e2)
    ind_e3 = numpy.argmin(e3)

    b = numpy.argmin([e1[ind_e1], e2[ind_e2], e3[ind_e3]])
    if b == 0:
        tc = ind_e1
    elif b == 1:
        tc = ind_e2
    else:
        tc = ind_e3

    THIV = (xb[tc][1] ** 2 + yb[tc][1] ** 2) ** 0.5

    return THIV,tc
```

# C APPENDIX

## C.1 LS-DYNA KEYWORDS

*AIRBAG_...
It is beyond the scope of the present thesis to deal with the already specified parameters of the airbag simulation.

*BOUNDARY_...

```
*BOUNDARY_SPC_SET
$#    nsid       cid      dofx      dofy      dofz     dofrx     dofry     dofrz$
   2000001         0         1         1         1         0         0         0
```

This keyword is used to define the boundary conditions. More specifically, to restraint specific degrees of freedom of a set of nodes, specified in (2000001). In the present case, the three translational degrees of freedom (dofx, dofy and dofz) in the four corners of the rigid road are fixed.

*CONSTRAINED_...
This series of keywords, contains different options for defining among others, nodal rigid bodies, connections between rigid bodies, welds and generally constrains between nodes, parts, bodies etc.

```
*CONSTRAINED_GENERALIZED_WELD_FILLET_ID
$#     wid    $
   1000001
$#    nsid       cid    filter    window       npr      nprt$
   1000025         0         0     0.000         0         0
$#   tfail      epsf      sigy      beta         l         w         a     alpha$
1.0000E+20&epsilonf &sigmaf        0.000 10.500000 70.000000  3.000000 45.000000
```

This keyword is used to define a fillet weld between the nodes of the nodal pair in the set nsid (1000025). The parameters epsf and sigy refer to the effective plastic strain at failure and the stress at failure respectively. Their values (epsilonf and sigmaf), are user defined parameters, defined using the keyword *PARAMETER.

```
*CONSTRAINED_SPOTWELD_ID
$#     wid     $
   1000001
$#      n1        n2        sn        ss         n         m        tf        ep$
   5000437   4000463     0.000     0.000     0.000     0.000     0.000     0.000
```

This keyword is used to define a spot weld between the two n1 (5000437) and n2 (4000463).

*CONTACT_...
This series of keywords, is used to define contacts (see subsection 4.5). Generally in all the contact types, a master and a slave surface should be specified using node sets, segment sets, parts, part sets and others.

Important parameters:

cid: contact id
ssid: slave surface id
msid: master surface id
sstyp: type of the ssid, 2 = part set id, 3 = part id, 4 = node set id
mstyp: type of the msid, identical to sstyp
fs, fd: static and dynamic coefficient of friction respectively
vdc: viscous damping coefficient in percent of critical. In order to avoid undesirable oscillation in contact, a contact damping perpendicular to the contacting surfaces is applied.

```
*CONTACT_AUTOMATIC_SINGLE_SURFACE_ID
$#     cid      $                                                    title
    1000001Strucrure
$#    ssid      msid     sstyp     mstyp    sboxid    mboxid       spr       mpr$
   1000002         0         2         0         0         0         0         0
$#      fs        fd        dc        vc       vdc    penchk        bt        dt$
  0.200000  0.1500001.0000E+20     0.000 20.000000         0     0.000     0.000
```

This is an one surface contact, i.e. only one surface is defined as slave surface and self penetration is searched. In particular, a set containing all the parts that consist the structure is specified (part set id = 1000002), and thus defining all possible contacts between the different parts, as well as self contacts of one part to itself. Moreover, friction is taken into account because of the non zero values of the two coefficients of friction. The defaults kept for the other parameters.

```
*CONTACT_AUTOMATIC_SURFACE_TO_SURFACE_ID
$#     cid         $                                                   title
   1000003CAR-STRUCTURE
$#    ssid      msid     sstyp     mstyp    sboxid    mboxid       spr       mpr$
         1   1000002         2         2         0         0         0         0
$#      fs        fd        dc        vc       vdc    penchk        bt        dt$
  0.400000  0.400000  1.000000     0.000 20.000000         0     0.000     0.000
```

This is a contact type of general use and according to LS-DYNA support, is the most widely used due to the fact that it defines the most common contact problem, the contact between two surfaces. Here a part set (1) that contains all the parts of the car is the slave surface, and the master surface is the part set that contains all the parts of the structure. Friction has been assumed between these two surfaces. This type of friction is used for the contact between the car and the road, and between the structure and the road. This last contact is useful because if a fractured piece of material fells, there is no surface to stop it and thus energy balance problems may occur.

```
*CONTACT_TIED_NODES_TO_SURFACE_ID
$#     cid           $                                                 title
   1000005Tied Bolts to Road
$#    ssid      msid     sstyp     mstyp    sboxid    mboxid       spr       mpr$
   1000097   2000001         4         3         0         0         0         0
```

This is a tied type of contact, where the contacting nodes of the slave surface to the master surface, are constrained to move together with the master surface. This type of contact was used to tie the bottom nodes of the bolts, on the surface of the rigid road.

```
*CONTACT_TIED_NODES_TO_SURFACE_CONSTRAINED_OFFSET_ID
$#     cid     $                                                      title
   1000102rings1-C1
$#    ssid      msid     sstyp     mstyp    sboxid    mboxid       spr       mpr$
   1000098   3000001         4         3         0         0         0         0
```

This type of contact was used to tie the nodes inner nodes of the rings, on the truss column surface. It was necessary to use this particular keyword because of the offset distance between the rings and the columns.

*CONTROL_...
This series of keywords are used to control or to apply multiple parameter definitions in different parts of the analysis. Generally the default values were kept except in some cases which are mentioned.

```
*CONTROL_ACCURACY
$#     osu       inn    pidosu$
         1         4         0
```

The purpose of this keyword is to define control parameters that can improve the accuracy of the calculation. Parameter osu is a global flag (=0 - off, =1 - on) for $2^{nd}$ order objective stress updates, and thus according to [36], it is important to be on when parts experience large rotations, like car tyres. In that case, the use of $2^{nd}$ order terms in the stress update formulas, has a significant impact in the resulting accuracy. The employemnet of the $2^{nd}$ terms in stress update can be chosen for some parts only, using the parameter pidosu.

```
*CONTROL_ENERGY
$#    hgen      rwen    slnten     rylen$
         2         2         2         2
```

This keyword provides controls for energy dissipation options. For the parameters it holds:
hgen = 2 - compute hourglass energy,
rwen = 2 - rigid wall energy dissipation is computed and included in the energy balance,
slnten = 2 - sliding interface energy dissipation is computed and included in the energy balance,
rylen = 2 - Rayleigh (damping) energy dissipation is computed and included in the energy balance.

```
*CONTROL_TERMINATION
$#  endtim    endcyc     dtmin    endeng    endmas$
 150.00000         0     0.000     0.000     0.000
```

The purpose of this keyword is to define the moment that the simulation ends as endtim, here 150 ms.

```
*CONTROL_TIMESTEP
$#  endtim    endcyc     dtmin    endeng    endmas$
 150.00000
$#  dtinit    tssfac      isdo    tslimt     dt2ms      lctm     erode     ms1st$
     0.000  0.900000         0     0.000 -0.001500       102         0         0
$#  dt2msf   dt2mslc     imscl    unused    unused     rmscl$
     0.000         0         0                       0.000
```

The purpose of this keyword is to set structural time step size control using different options. The parameter dt2ms is important in explicit analysis. The critical time step is computed according to section 4.3 but usually it is inefficiently small. For that reason, LS-DYNA adds a small amount of lumped mass to the nodes of the element that was responsible for that small time step. The result is that the time step increases making the analysis more efficient. This procedure is called dynamic mass scaling and the parameter dt2ms controls it. More specifically, if it is negative, the minimum time step is tssfac*|dt2ms| and any mass scaling is performed until the criterion for the critical time step is met. At the end of the simulation, it is possible to check the amount of extra mass used to control the time step.

*DATABASE_...
This series of keywords is used to define the desirable output quantities such as node histories, cross sectional data, element stresses and strains, energetic equilibrium data etc.

*ELEMENT_...
All the elements of the calculation should be defined using the corresponding keyword from that series. A reduced input is shown for some of the different element types.

```
*ELEMENT_SOLID
$#   eid     pid      n1      n2      n3      n4      n5      n6      n7      n8$
 1008597 1000011 1004488 1004489 1010080 1010079 1000651 1000652 1004480 1004479
 1008598 1000011 1004489 1000656 1004485 1010080 1000652 1000001 1000653 1004480
 1008599 1000011 1004485 1004486 1010083 1010080 1000653 1000654 1004481 1004480
```

This keyword is used to define solid elements. The parameter eid refers to the element id, pid to the part id and n1 to n8 to the ids of the 8 nodes that define the solid element. For practical reasons, the elements of a Finite Element model are usually defined using a preprocessor and being automatically converted in LS-DYNA keyword format.

```
*ELEMENT_SHELL
$#   eid     pid      n1      n2      n3      n4      n5      n6      n7      n8$
 3000001 3000006 3000217 3001407 3005463 3001425       0       0       0       0
 3000002 3000006 3001407 3001408 3005464 3005463       0       0       0       0
 3000003 3000006 3001408 3001409 3005465 3005464       0       0       0       0
```

This keyword is used to define shell elements. The parameter eid refers to the element id, pid to the part id and n1 to n4 to the ids of the 4 nodes that define the shell element.

```
*ELEMENT_DISCRETE
$#   eid     pid      n1      n2     vid               s      pf          offset$
 9000001 9000003 4000055 6000110       0        1.000000       0           0.000
 9000002 9000003 4000118 6000284       0        1.000000       0           0.000
 9000003 9000003 4000181 6000458       0        1.000000       0           0.000
```

This keyword is used to define spring elements. The parameter eid refers to the element id, pid to the part id and n1, n2 to the ids of the 2 nodes that define the spring element. The other values were kept to default.

*HOURGLASS_...

```
*HOURGLASS
$#    hgid       ihq        qm       ibq        q1        q2    qb/vdc        qw$
   1000001         3     0.000         0     0.000     0.000     0.000     0.000
```

The purpose of this keyword is to define hourglass and bulk viscosity properties which are referenced via HGID. The parameter ihq is important because it designates the hourglass control type. It was observed that the viscous form types (ihq = 1,2 and 3) provided good results for solid elements, while the stiffness form types (4 and 5) were better for shell elements.

*INITIAL_...
The purpose of this series of keywords, is to provide a way of initializing velocities and detonation points.

```
*INITIAL_VELOCITY
$#    nsid    nsidex     boxid    irigid      icid$
   3000005         0         0        -1         0
$#      vx        vy        vz       vxr       vyr       vzr$
&initialx      0.000     0.000     0.000     0.000     0.000
```

This keyword was used to define the translational and rotational components of the initial velocity of the node set nsid (3000005). In this case the node set 3000005 contains all the nodes of the car, together with the dummy and the seat. The user defined parameter initialx is used to define the x component of the initial velocity.

*MAT_...
The purpose of this series of keywords, is to define the required physical and mechanical

parameters for the specification of a material model. The keywords for the bilinear model of the steel as well as the elastic material of the spring are shown (see section 3.1.5).

```
*MAT_PIECEWISE_LINEAR_PLASTICITY_TITLE
S235JR
$--------------------------------------------------------------------------------$
$#     mid        ro         e        pr      sigy      etan      fail      tdel$
   1000001 7.8650E-6 210.00000  0.300000  0.235000  0.840000  0.150000     0.000
$#       c         p      lcss      lcsr        vp$
     0.000     0.000         0         0     0.000
$#    eps1      eps2      eps3      eps4      eps5      eps6      eps7      eps8$
     0.000     0.000     0.000     0.000     0.000     0.000     0.000     0.000
$#     es1       es2       es3       es4       es5       es6       es7       es8$
     0.000     0.000     0.000     0.000     0.000     0.000     0.000     0.000
```

This keyword is used to define materials that exhibit plastic behaviour, as a series of lines. In this case two lines were used (bilinear material model). The parameters defined by this keyword are:
mid: material id
ro: density
e: Young's modulus, slope of the first, elastic line
pr: Poisson ratio
sigy: yield stress
etan: tangent modulus, slope of the second plastic, line
fail: plastic strain at failure. When the strain within an element reaches this value, the element is considered as failed and it is deleted from the calculation.

```
*MAT_SPRING_ELASTIC
$#     mid         k$
   9000002&bspring
```

This keyword is used to define the elastic constant of an elastic spring. The user defined parameter bspring, is used to transfer this value to that keyword.

*NODE_...

```
*NODE
$#   nid               x               y               z      tc      rc$
 1000001       469.85001           0.000       30.000000       0       0
 1000002       500.00000           0.000       30.000000       0       0
 1000003       500.00000      -30.150000       30.000000       0       0
```

The purpose of this keyword is to define all the nodes in the numerical model. The parameter nid, refers to the node's id while x,y and z are the Cartesian coordinates of the node in the global coordinate system. The parameters tc and rc, can b used to apply translational and rotational constraints respectively. For practical reasons, the nodes of a Finite Element model are usually defined using a preprocessor and being automatically converted in LS-DYNA keyword format.

*PARAMETER_...

```
*PARAMETER
R initialx 27.77770
R sigmaf   0.36000
R epsilonf 0.15000
R bspring  450.00000
```

The purpose of this keyword is to define user defined parameters that will be used in other parts of the input file. It is a very convenient way to control the values of important variables

of the model, without having to refer to multiple keywords. Here the parameters initialx which is used in keyword *INITIAL_ VELOCITY, the parameters sigmaf and epsilonf which are used in the keyword *CONSTRAINED_ GENERALIZED_ WELD_ FILLET and the parameter bspring which was used in keyword *MAT_ SPRING_ ELASTIC, are defined.

*PART_...

```
*PART
$# title  $
SIGN
$#     pid     secid       mid     eosid      hgid      grav    adpopt      tmid$
   5000001   1000004   1000002         0   1000001         0         0         0
```

The purpose of this keyword is to provide a way to control attributes of a set of elements that consist one part. In each element definition, a part id is included, see keyword *ELEMENT_. Using the *PART keyword, it is possible to assign a section, secid (keyword *SECTION_), a material, mid (keyword *MAT_), a specified hourglass control, hgid (keyword *HOURGLASS_) and other parameters, the values of which kept to default, to the part with id pid.

*SECTION_...
The purpose of that keyword, is to define beam, shell, solid and other types of cross sections. Only the shell and the solid sections are shown.

```
*SECTION_SHELL_TITLE
pipe_large
$#   secid    elform      shrf       nip     propt    qr/irid     icomp     setyp$
   1000001         1  0.833333         2         1         0         0         1
$#      t1        t2        t3        t4      nloc     marea      idof    edgset$
  2.900000  2.900000  2.900000  2.900000  1.000000     0.000     0.000         0
```

The important parameters of the shell section definition keyword are: secid: unique section id. elform: element type, 1 - Hughes-Liu shell element. shrf: Shear factor which scales the transverse shear stress (a suggested value is 5/6). nip: number of through-thickness integration points, two such points were used in order to account for bending. qr/irid: quadrature rule or integration, 0 - Gauss rule. t1 - t4: thickness of the shell at the 4 nodes. nloc: Location of reference surface for three dimensional shell elements, 0: top surface, 1.0: mid-surface, -1.0: bottom surface.

```
*SECTION_SOLID_TITLE
foundation_plates,rods,rings
$#   secid    elform       aet$
   1000003         1         0
```

This keyword, that is used to define solid section, is much more simple than the shell option, as expected. Except the unique section id, the element type is defined with the aid of the parameter elform (1 - constant stress solid element).

*SET_...
The purpose of that series of keywords, is to define sets of nodes, elements, parts, etc.

*END
Finally, this keyword is required to denote the end of the input file.

## C.2 IMPACT AGAINST SINGLE TRUSS

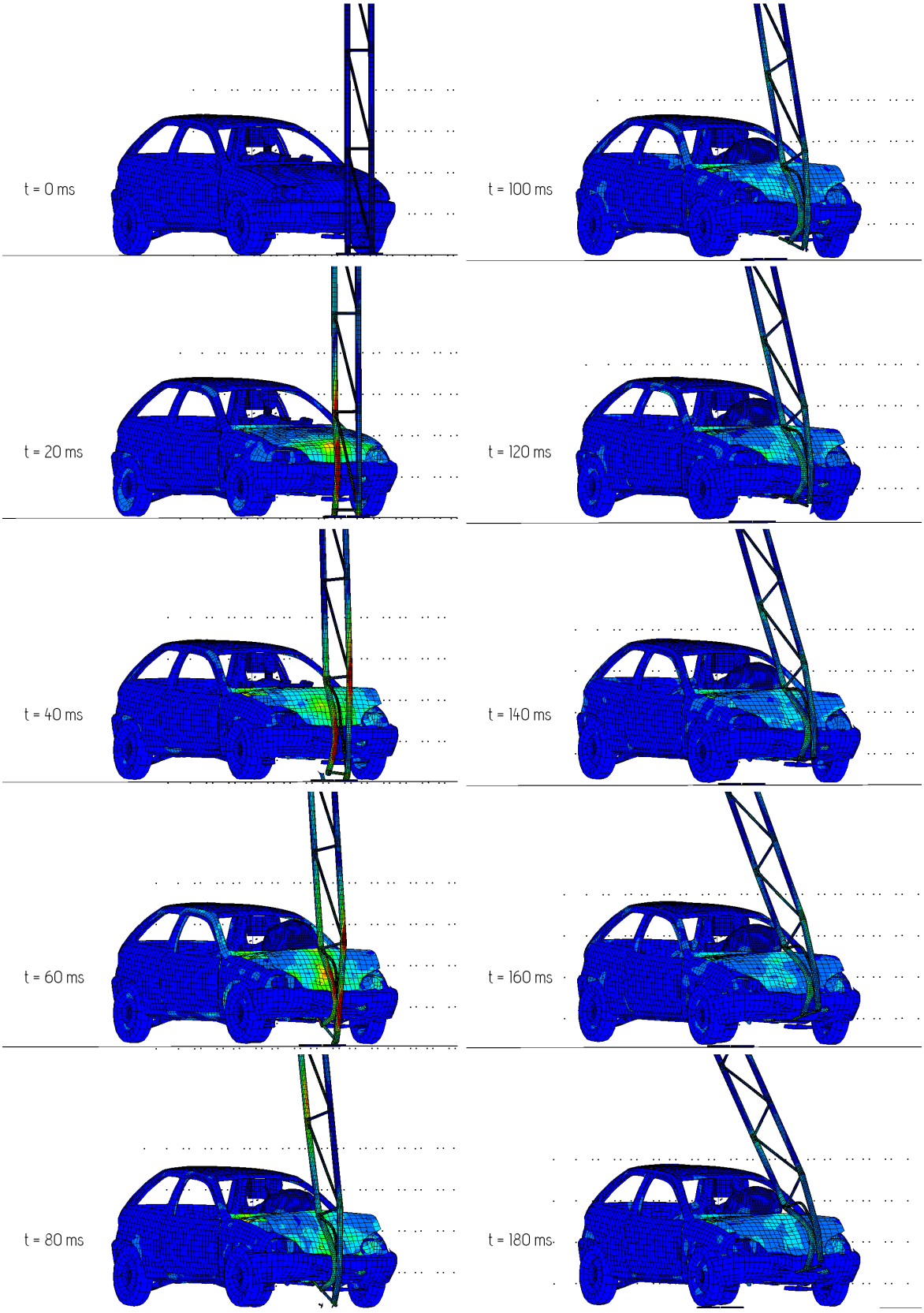


Figure C.1: Von-Misses stress distribution in GPa for time steps 0 - 180 ms in perspective view for single truss impact case.

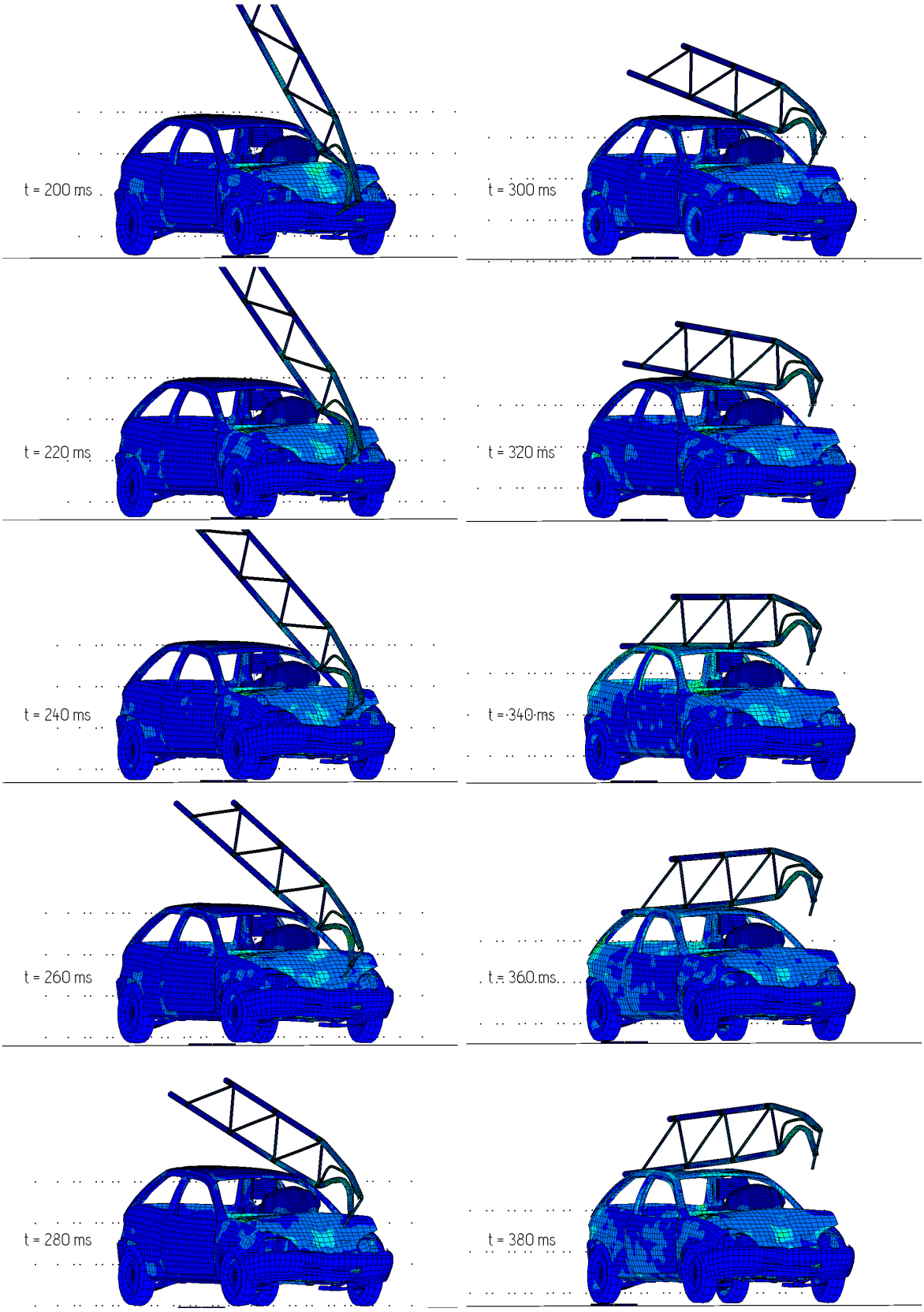


Figure C.2: Von-Misses stress distribution in GPa for time steps 200 - 380 ms in perspective view for single truss impact case.

# LIST OF FIGURES

# LIST OF TABLES

# BIBLIOGRAPHY


[1] Crash analysis criteria discreption. Technical report, Arbeitskreis Messdatenverarbeitung Fahrzeugsicherheit.

[2] EN 12767:2007. *Passive safety of support structures for road equipment - Requirements, classification and test methods*.

[3] EN 12899-1:2007. *Fixed, vertical road traffic signs - Part 1: Fixed signs*.

[4] EN 1317-1:2010. *Road restraint systems - Part 1: Terminology and general criteria for test methods*.

[5] EN 1993-1-1:2005. *Design of steel structures - Part 1-1: General rules and rules for buildings*.

[6] EN 1999-1-1:2007. *Design of aluminium structures - Part 1-1: General rules - General rules and rules for buildings*.

[7] ISO 6487:2002. Road vehicles - measurement techniques in impact tests - instrumentation. Technical report, 2002.

[8] ISO 898-1:2009. *Mechanical properties of fasteners made of carbon steel and alloy steel - Part 1: Bolts, screws and studs with specified property classes - Coarse thread and fine pitch thread*.

[9] Sohrabuddin Ahmad, Bruce M. Irons, and O.C. Zienkiewicz. Analysis of thick and thin shell structures by curved finite elements. *International Journal for Numerical Methods in Engineering*, 2(3):419–451, 1970.

[10] Ted Belytschko, Jerry I. Lin, and Tsay Chen-Shyh. Explicit algorithms for the nonlinear dynamics of shells. *Computer methods in applied mechanics and engineering*, 42(2):225–251, 1984.

[11] Ted Belytschko, Wing Kam Liu, and Brian Moran. *Nonlinear Finite Elements for Continua and Structures*. Wiley, 2000.

[12] Michael Blum and Jean-Baptiste Durand. *Lecture notes in Multidimensional Statistical Analysis*. TIMC-IMAG Laboratory, Techniques for biomedical engineering and complexity management - informatics, mathematics and applications - Grenoble, 2011.

[13] Ola Boström, Yngve Haland, Rikard Fredriksson, Mats Y. Svensson, and Hugo Mellander. A sled test procedure proposal to evaluate the risk of neck injury in low speed rear impacts using a new neck injury criterion (nic). *16 th Conference on the Enhanced Safety of Vehicles*, pages 1579–1585, 1998.

[14] G.E.P. Box and N.R. Draper. *Response Surfaces, Mixtures, and Ridge Analyses*. Wiley Series in Probability and Statistics. Wiley, 2007.

[15] Martin Dietrich Buhmann. *Radial basis functions: theory and implementations*, volume 12. Cambridge university press, 2003.

[16] Clifford C. Chou, Jialiang Le, Ping Chen, and Dj Bauch. Development of CAE simulated crash pulses for airbag sensor algorithm/calibration in frontal impacts. In *17th International Technical Conference on the Enhanced safety of Vehicles, Amsterdam*, 2001.

[17] CARE Community database on Accidents on the Roads in Europe. *http://ec.europa.eu/transport/road_safety/index_en.htm*. European Comission, 2012.

[18] Edwin L. Fasanella and Karen E. Jackson. *Best practices for crash modeling and simulation*. National Aeronautics and Space Administration (NASA), Langley Research Center, 2002.

[19] RISER Roadside Infrastructure for Safer European Roads. *D06: European Best Practice for Roadside Design: Guidelines for Roadside Infrastructure on New and Existing Roads*. Chalmers University of Technology, 2005.

[20] Marco Götz, Wolfgang Graf, Aleksandra Serafinska, and Michael Kaliske. Surrogate models in early design stages. *Proceedings of 11th International Conference on Structural Safety & Reliability, Columbia University New York*, 2013.

[21] Marco Götz, Martin Liebscher, and Wolfgang Graf. Efficient detection of permissible design spaces in an early design stage. *11. LS-DYNA Forum, Ulm 2012*, 2012.

[22] Wolfgang Graf, Marco Götz, and Michael Kaliske. Analysis of dynamical processes under consideration of polymorphic uncertainty. *Proceedings of 11th International Conference on Structural Safety & Reliability, Columbia University New York*, 2013.

[23] J.O. Hallquist, D.J. Benson, and G.L. Goudreau. Implementation of a modified Hughes-Liu shell into a fully vectorized explicit finite element code. Technical report, Lawrence Livermore National Lab., CA (USA), 1985.

[24] John O. Hallquist. *LS-DYNA Theory Manual*, 2006.

[25] Oliver Hechler, Georges Axmann, and Boris Donnay. The right choice of steel-according to the eurocode. Symposium proceedings: Use of steel materials in buildings & construction, Hong Kong, China, 2009.

[26] Hans-Wolfgang Henn. Crash tests and the head injury criterion. *Teaching Mathematics and its Applications*, 17(4), 1998.

[27] Nicholas J. Higham. *Accuracy and Stability of Numerical Algorithms*. Society of Industrial and Applied Mathematics, Philadelphia, 1996.

[28] Gerhard A Holzapfel. *Nonlinear solid mechanics: a continuum approach for engineering*. John Wiley & Sons Ltd., 2000.

[29] Thomas JR Hughes and Wing Kam Liu. Nonlinear finite element analysis of shells: Part i. three-dimensional shells. *Computer Methods in Applied Mechanics and Engineering*, 26(3):331–362, 1981.

[30] Thomas JR Hughes and Wing Kam Liu. Nonlinear finite element analysis of shells: Part ii. two-dimensional shells. *Computer Methods in Applied Mechanics and Engineering*, 27(2):167–181, 1981.

[31] SAE J211-1. *Instrumentation for Impact Test, Part 1, Electronic Instrumentation*. SAE International: The Engineering Society For Advancing Mobility Land Sea AIr and Space, 1995.

[32] Arun Kaintura. *Application of metamodel technologies in engineering tasks*. TU Dresden, Insitute for structural analysis. Master Thesis, 2013.

[33] G. Kokolakis and I. Spiliotis. *Introduction to Probability theory and Statistics*. Simeon Editions, 4th edition, 1999 (in greek language).

[34] Višnja Tkalčević Lakušić. The safety of roadside columns in the event of vehicle impact. *Gradevinar*, 4:305–313, 2012.

[35] W. J. Lewis. *Tension Structures, Form and Behaviour*. Thomas Telfold, 2003.

[36] Livermore Software Technology Corporation (LSTC). *LS-DYNA Keyword User's Manual*, 2013.

[37] Livermore Software Technology Corporation (LSTC). *LS-DYNA User's Guide*, 2013.

[38] Murray Mackay. The increasing importance of the biomechanics of impact trauma. *SADHANA - Academy Proceedings in Engineering Sciences, Indian Academy of Sciences*, 32(4):397–408, 2007.

[39] Brian G. McHenry. Head injury criterion and the atb. *ATB User's Group*, 2004.

[40] Bernd Möller and Michael Beer. *Fuzzy Randomness - Uncertainty in Civil Engineering and Computational Mechanics*. Springer, 2004.

[41] Bernd Möller and Michael Beer. Engineering computation under uncertainty–capabilities of non-traditional models. *Computers & Structures*, 86(10):1024–1041, 2008.

[42] Bernd Möller, Wolfgang Graf, and Michael Beer. Fuzzy structural analysis using $\alpha$ level optimization. *Computational Mechanics*, 26:547–565, 2000.

[43] Bernd Möller, Martin Liebscher, Karl Schweizerhof, Steffen Mattern, and Gunther Blankenhorn. Structural collapse simulation under consideration of uncertainty–improvement of numerical efficiency. *Computers & Structures*, 86(19):1875–1884, 2008.

[44] Athanasios Papoulis. *Probability, Random Variables and Stochastic Processes*. Series in Electrical and Computer Engineering. McGraw-Hill, 4th edition, 2002.

[45] Erprobung passiver Schutzeinrichtungen für Strassen. Die Beeinflussung des Nachfrageverhaltens durch die Voranzeige des Straßenverlaufs mit Hilfe von Straßenrandmarkierungen. *Forschung, Straßenbau und Straßenverkehrstechnik*, Heft 336, 1981.

[46] J. N. Reddy. *An Introduction to Nonlinear Finite Element Analysis*. Oxford University Press, 2004.

[47] J.C. Simo and T.J.R. Hughes. *Computational Inelasticity*. Springer, 2008.

[48] Frank Steinigen, Jan-Uwe Sickert, Wolfgang Graf, and Michael Kaliske. Fuzzy and fuzzy stochastic methods for the numerical analysis of reinforced concrete structures under dynamical loading. *Computational Methods in Stochastic Dynamics*, (K - I):27–40, 2013.

[49] Johannes Will and Uli Stelzmann. Robustness evaluation of crashworthiness using LS-DYNA and optiSLang. *ANSYS Conference & $25^{th}$ CADFEM User's Meeting*, 2007.